National Technical University of Athens
School of Mechanical Engineering
Department of Fluid Mechanics
Parallel CFD & Optimization Unit

Formulation & Programming of a Fluid-Structure Interaction Method & Applications in Inflatable Wings

Diploma Thesis

George E. Papageorgiou

Advisor: Kyriakos C. Giannakoglou, Professor NTUA

Athens, 2019

Acknowledgements

First and foremost, I would like to express my deepest gratitude to my professor, K. Giannakoglou for not only guiding me during the process of completing this diploma thesis, but also for trusting and presenting me with the unique opportunity of working on my thesis in an on-going industrial project.

I would also like to acknowledge Toyota Motor Europe (TME) and Toyota Motor Corporation (TMC) where the idea for this diploma thesis started. I would like to express my deep gratitude to Dr. Kostas Gkagkas for the fruitful discussion we had on a similar project running in parallel at the PCOpt/NTUA and Mr. Eiji Itakoura whose ideas and vision fuelled the whole project.

I would also like to deeply thank Dr. Kostas Tsiakas, who dedicated so many hours of his time, answering to my many questions and helping me wherever an issue appeared. In addition, I would like to express my deep gratitude to Dr. Xenofon Trompoukis and Dr. Varvara Asouti who both guided me and answered to my questions immediately although they are very busy. The whole research team of PCOpt/NTUA is always more than eager to help when needed.

Also, my friends for being always there when I need a break. In closing, I could not miss to thank, all members of the Prom Racing Team of the NTUA for our cooperation over the years. The student engineering competition 'formula student' is a unique educational experience, which I had the opportunity to experience during my studies at the NTUA.

Finally, I would like to thank my parents and my sister for their love and support throughout the years that I studied at my university NTUA. Thank you for enduring all of my complaints and being there for me.

National Technical University of Athens
School of Mechanical Engineering
Department of Fluid Mechanics
Parallel CFD & Optimization Unit

Formulation & Programming of a Fluid-Structure Interaction Method & Applications in Inflatable Wings

Diploma Thesis
George E. Papageorgiou
Advisor: Kyriakos C. Giannakoglou, Professor NTUA

In this thesis, a tool capable of performing aeroelastic analysis of inflatable wings is presented. In order to perform the aeroelastic analysis, the PUMA (Parallel solver, for Unstructured grids, for Multi-blade row computations, including Adjoint) GPU-enabled (Graphics Processing Unit) CFD (Computational Fluid Dynamics) solver developed by the Parallel CFD & Optimization Unit (PCOpt/NTUA) is used for the flow prediction and the aerodynamic load computation. For the structural analysis, the commercial s/w MAPDL (Mechanical ANSYS Parametric Design Language by ANSYS) is used, since it offers the capability to be executed in batch mode from a script and can thus be integrated into an aeroelastic loop.

To perform an aeroelastic analysis with two different solvers, each one using a different grid, Fluid Structure Interaction (FSI) tools are needed in order to interpolate values between them. An interpolation tool based on finite element shape functions is programmed in order to interpolate pressures from the CFD surface grid to the CSM (Computational Solid Mechanics) grid and deformations from the CSM grid to the CFD one. Also, an RBF-based (Radial Basis Function) grid displacement tool is used for adapting and regenerating the volume CFD grid. Various interfacing tools are also programmed to enable the fully automatization of the aeroelastic loop.

After programming the needed FSI tools to fully automatize the aeroelastic loop, several aeroelastic analyses on inflatable wings are performed. Specifically, two different geometries for the inflatable wing are designed and analysed. Also revisions of each case are performed with different materials. Finally, analyses are performed by using the inflatable wing including the tethers, which are used to support the inflatable wing are examined in order to analyse effect on the aeroelastic problem. Useful results for the aeroelastic behaviour of inflatable wings are thus extracted.

Εθνικό Μετσόβιο Πολυτεχνείο
Σχολή Μηχανολόγων Μηχανικών
Τομέας Ρευστών
Μονάδα Παράλληλης Υπολογιστικής Ρευστοδυναμικής
& Βελτιστοποίησης

Διατύπωση & Προγραμματισμός Μεθόδου Αλληλεπίδρασης Ρευστού-Στερεού & Εφαρμογές σε Φουσκωτές Πτέρυγες.

Διπλωματική Εργασία

Παπαγεωργίου Ε. Γεώργιος
Επιβλέπων: Κυριάκος Χ. Γιαννάκογλου, Καθηγητής ΕΜΠ

Στην εργασία αυτήν παρουσιάζεται ένα εργαλείο ικανό να πραγματοποιήσει αεροελαστική ανάλυση σε φουσκωτές πτέρυγες. Αρχικά για την πραγματοποίηση αεροδυναμικής ανάλυσης χρησιμοποιείται το λογισμικό PUMA (**P**arallel solver, for **U**nstructured grids, for **M**ulti-blade row computations, including **A**djoint) το οποίο έχει αναπτυχθεί από τη Μονάδας Παράλληλης Υπολογιστικής Ρευστοδυναμικής & Βελτιστοποιήσης του ΕΜΠ (ΜΠΥΡΒ/ΕΜΠ) και εκτελείται σε κάρτες γραφικών (GPU) για την πρόλεξη της ροής και τον υπολογισμό των αεροδυναμικών φορτίων. Για την δομική ανάλυση, χρησιμοποιείται το εμπορικό πακέτο MAPDL (**M**echanical **A**NSYS **P**arametric **D**esign **L**anguage), το οποίο αποτελεί τμήμα του εμπορικού λογισμικού ANSYS. Για το συγκεκριμένο λογισμικό συντάχθηκε η αλληλουχία των εντολών σε μορφή γλώσσας προγραμματισμού για την επίλυση των εξισώσεων της μηχανικής του προβλήματος και ενσωματώθηκε στην αυτόματη αεροελαστική ανάλυση. Προγραμματίστηκαν ακόμα διάφορα εργαλεία για την πλήρη αυτοματοποίηση της αεροελαστικής μεθόδου.

Ωστόσο οι δύο διαφορετικοί επιλύτες χρησιμοποιούν διαφορετικά πλέγματα για να λύσουν τις εξισώσεις, επομένως μια μέθοδος αλληλεπίδρασης ρευστού-στερεού απαιτεί διάφορα εργαλεία προκειμένου να παρεμβάλει μεγέθη ανάμεσα στα δύο αυτά πλέγματα. Γι αυτόν τον λόγο προγραμματίστηκε μια μέθοδος παρεμβολής η οποία βασίζεται στις συναρτήσεις μορφής των πεπερασμένων στοιχείων για την παρεμβολή πιέσεων από το αεροδυναμικό πλέγμα στο πλέγμα του στερεού και παραμορφώσεων από πλέγμα του στερεού στο αντίστοιχο αεροδυναμικό. Ακόμα, για την παραμόρφωση του ογκικού αεροδυναμικού πλέγματος χρησιμοποιείται λογισμικό βασιζόμενο στη θεωρία των συναρτήσεων ακτινικής βάσης (**R**adial **B**asis **F**unction).

Μετά τον προγραμματισμό των διαφόρων εργαλείων πραγματοποιήθηκαν αρκετές αεροελαστικές μελέτες σε φουσκωτές πτέρυγες. Συγκεκριμένα, σχεδιάστηκαν και μελετήθηκαν δύο διαφορετικές γεωμετρίες φουσκωτών πτερύγων. Επιπλέον, κάθε γεωμετρία αναλύθηκε χρησιμοποιώντας διαφορετικά υλικά. Τέλος, πραγματοποιήθηκαν αναλύσεις, οι οποίες περιελάμβαναν τα σχοινιά πρόσδεσης προκειμένου να εκτιμηθεί η επίδραση τους στο αεροελαστικό πρόβλημα. Συνεπώς, μπορούν να εξαχθούν χρήσιμα συμπεράσματα για την αεροελαστική συμπεριφορά των φουσκωτών πτερύγων.

Acronyms

NTUA	National Technical University of Athens
PCOpt	Parallel CFD & Optimization unit
CFD	Computational Fluid Dynamics
PUMA	Parallel solver, for Unstructured grids, for Multi-blade row computations, including Adjoint
LTT	Lab of Thermal Turbomachines
CSM	Computational Solid Mechanics
RANS	Reynolds Averaged Navier Stokes
MAPDL	Mechanical ANSYS Parametric Design Language
FSI	Fluid Structure Interaction
RBF	Radial Basis Function
GPU	Graphics Processing Unit
CPU	Central Processing Unit
IGES	Initial Graphics Exchange Specification

Contents

Chapter 1

Introduction

1.1 Aeroelasticity

Aeroelasticity is the branch of physics and engineering and encompasses interactions of structures (stiffness), mass properties (inertia) and aerodynamics, with occasional further considerations for thermal and propulsion effects, Fig. 1.1. It is common in aerospace field in which vehicles require a minimal-weight structure that is capable of withstanding large aerodynamic load changes. These requirements, when used by an optimization method, usually lead to a flexible vehicle structure. In such a case though, a degradation in the aeroelastic stability of the vehicle may appear.

The basic feature of aeroelasticity is that fluid flowing around a structure exerts aerodynamic forces on it causing the deformation of it. This change in the structure results in the redistribution of air loads, which affects the aerodynamic performance of the surface compared to a rigid aerodynamic surface and so on so forth. The simultaneous analysis of aerodynamic loads, structural loads and the disturbance in air flow caused by the structure deformation gives rise to the aeroelastic state equilibrium, [1].

The study of aeroelasticity may broadly be classified into two categories with respect to the time dependence of inertial and aerodynamic forces. If during the analysis of aerodynamics problems loads vary relative slow, a static method could be applied. An example of a static phenomenon for wings is divergence, [2]. Divergence occurs when a lifting surface, under aerodynamic load, deflects in a way which increases the applied load and, thus, twisting effect. As the structure deflects further, the twisting is amplified, bringing the structure to the point of divergence. The remaining problems are dynamic and occur as a result of inertial forces, aerodynamic forces and structure stiffness. An example of a dynamic phenomenon is flutter, Fig. 1.2.

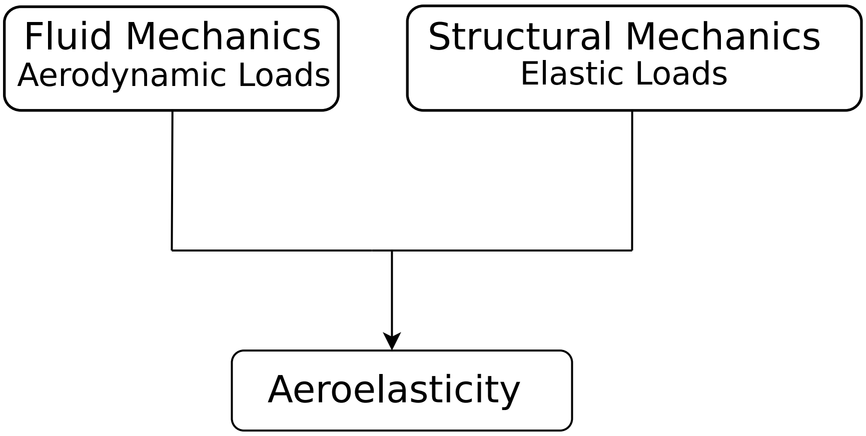

Figure 1.1: *Aeroelasticity Basic Fields Interaction.*

Flutter is the dynamic instability of a structure subjected to external forces. As the dynamic pressure on a structure increases, there is a point at which the structural damping (material damping) cannot damp the motions which are further amplified due to the applied aerodynamic energy. This could become catastrophic for the structure and should be prevented early from the design phase, [3]. It is obvious from the above that, aeroelastic phenomena are playing a major role in all applications, which include an elastic structure exposed to a fluid flow.

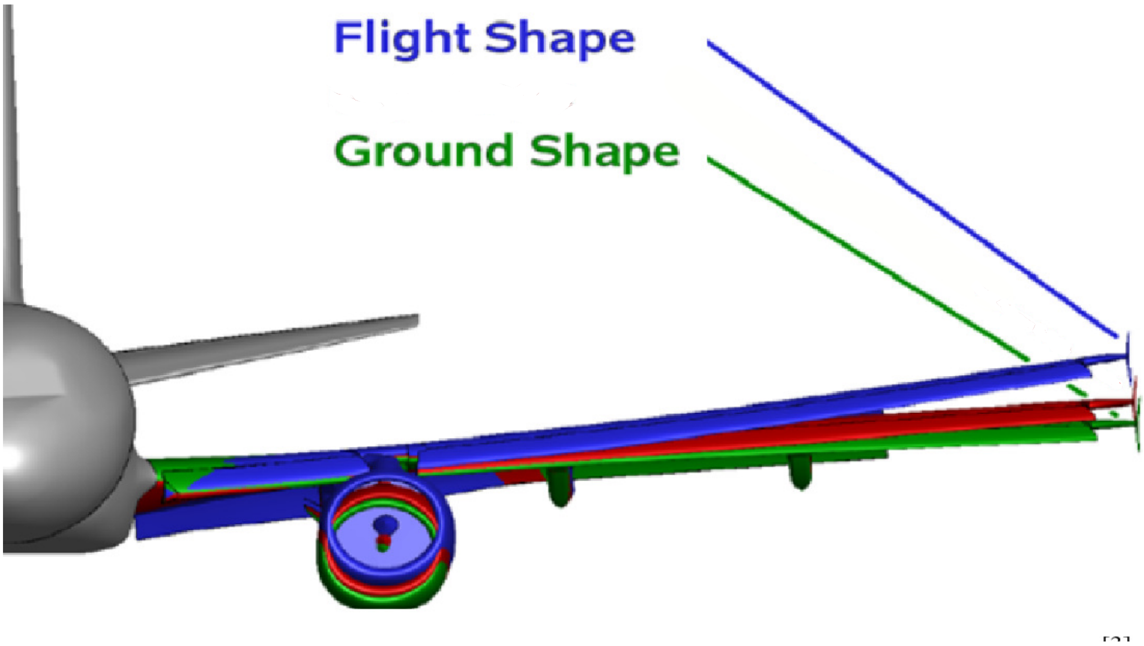

Figure 1.2: *Bending of wing during flight, [4].*

1.2 Inflatable Structures

An inflatable structure is one that is filled by a pressurized gas, typically air, in order to obtain its shape and size. Inflatable structures are usually constructed by two layers of membrane connected together with longitudinal or transverse members called spars. These spars separate the structure into different air-tight compartments, which are filled with the selected gas. Inflation creates the needed structural rigidity and enables the construction of larger structures. Since, the pressurized gas undertakes the basic structural role, providing strength and shape, the membrane needed is very thin and its primary role is to contain the gas, occupying only a small portion of the whole volume. As a result, the total weight and cost are significant low and by emptying the gas the total size can be dramatically reduced, facilitating storing and transportation, [5].

However, inflatable structures have a basic drawback, since in case of puncturing the flexible membrane, loss of the pressurized gas and collapse of the whole structure, may occur. This can be dealt with the creation of separate air-tight compartments instead of a singe one and, also, with the use of new materials, which are flexible enough to accommodate the gas needed though hard enough to withstand hits by blunt objects. Recently, the development of new composite materials designed specifically with the above characteristics, created a new interest in inflatable structures and their potential use in many new fields such as in aerospace, transportation, etc.

1.2.1 Uses of Inflatable Structures

Although material science progress helped inflatable structures to find uses in new areas, their basic idea is not new and dates back to the ancient times. At first, people used animal skins filled with air in order to cross rivers, [6], however due to the lack of materials needed for the membrane, extensive use of inflatable structures began in the 19th century. Nowadays, they are used in many aspects of our daily life.

An inflatable structure which is used every day in million applications is the pneumatic tire. Tires are basically designed to act as dampers for bumpy and rough roads, protecting the vehicle and passengers and contributing to an easier and safer transportation. Usually, they are made from a rubber material reinforced with steel cords and containing pressurized air. They are used extensively in cars, airplanes, trucks, etc. in any kind of transportation, in which a vehicle should come to contact with the ground. The idea of tires and its invention was made in England in the early 1800s, [7]. Since then, tire technology has improved dramatically, expanding its usage even in space missions.

Another field in which inflatable structures are extremely common is maritime, with the inflatable boats. As already mentioned, the first inflatable object was used for crossing rivers and after the invention of techniques capable of making rubbery materials more durable and flexible, the first type of inflatable boat was created. Nowadays, those boats are very common and have several uses. Specifically, since they are portable, lightweight and, when propelled by motors, adequate fast, they have diverse roles and are used in rescue missions or recreation. Also, in most ships, the emergency lifeboats are small inflatable boats capable of accommodating passengers and staying afloat for several days, [6].

Recently, with the use of new materials, inflatable structures are used as buildings especially for holding sports and recreation events. The structure can be either wholly, partially, or roof-only air supported, Fig. 1.3, [5]. Also, these inflated buildings could be used for emergency situations, since they can easily be transported and assembled in minutes; they could also be deployed after natural disasters to accommodate hospitals and all the necessary facilities.

Figure 1.3: *Inflatable Roof of a Stadium in Tokyo,[8].*

In addition, inflatable structures are used for protecting people during disasters, since they can be accommodated very efficiently and inflated even by mouth. Airbags, for example, are used for protecting passengers during crashes by inflating rapidly when large acceleration occurs and deflating quickly after that, providing soft cushioning. Another structure offering protection is the life jacket which inflate easily and helps the wearer to stay afloat.

Lastly, in the aerospace field, inflatable structures have an extensive use which dates back to late 1700s. An inflatable structure was used to achieve the first manned flight in 1783 and; in specific, this was a balloon inflated with hydrogen, [9]. Since then, they are used for many years for transportation, scientific reasons and, nowadays, for recreation. In recent years, for example, weather balloons are launched around the world every day for diagnosing current weather conditions as well as for updating computer models for weather forecasting. Another inflatable structure used in aviation for several years is the airship. Airships are made by a membrane like envelope, which is used to contain pressurized gas, such as helium, and create the needed lift for the structure to stay at an altitude. They were primary used for the transportation of goods and people for several years until replaced by airplanes. However, even today, new projects are running in order to make them useful for modern applications.

During the past years, research regarding inflatable structures has been intensified since they have a potential use in interplanetary missions, Fig. 1.4. The basic objective for this kind of missions is the total weight and volume of the structures to be as low as possible. Since inflatable structures by design fulfil this objective, NASA and other aerospace organizations experiment with different designs, materials and techniques. The basic idea is to keep the structure in a deflated state, in a volume significant smaller than the final deployed volume, in order to save storage space and when necessary, the inflation can be accomplished in a few seconds. Inflatable structures had already used in the exploration of Venus, Fig. 1.4, in which two large balloons were inflated with helium and then float in the atmosphere providing data. Future plans for exploring other planets typically include inflatable structures (in which astronauts could be protected from the harsh environment) or research vehicles with inflated components for data gathering.

Figure 1.4: *Replica of the balloon used in Venus exploration,[10]*

1.2.2 Inflatable Wings

Nowadays, the structure which has the most potential for several uses is an inflatable wing. The concept of such wings was developed decades ago [11], however lastly new design studies contribute in designing new models with much more capabilities than the early models. The basic concept is to keep the wing stowed when not in use and deploy it at will. The wing span may vary from as small as 15cm to 10m. However, the most promising size is that of the wings needed by a small UAV (Unmanned Aerial Vehicle) that can be carried and deployed from a man, [1]. In that case, the wings must be deflated in order for the UAV to be possible to be transported and stored. An UAV which can store its wings inside its fuselage has many potential uses even in space exploration, since it could be stowed and deployed at another planet's atmosphere, reducing weight and space needed during the travel, Fig. 1.5

Nonetheless, inflatable wings have two major drawbacks, which limit their uses. First, is the lack of control surfaces (ailerons) which renders the navigation of a UAV almost impossible. This problem can be dealt with by changing the wing geometry in real time. Second, is the high wing deflections and deformations under high loads, which results in losing airfoil shape and the aerodynamic characteristics. However, with the development of new materials this problem could also be solved to a certain degree.

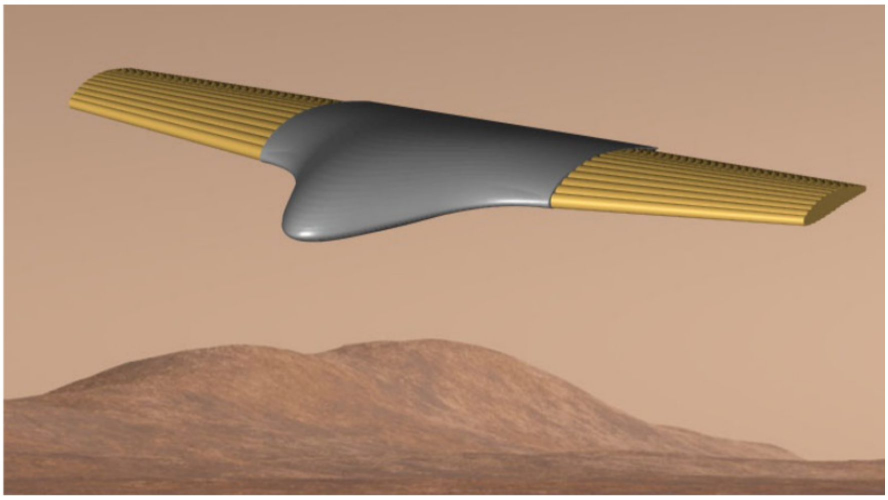

Figure 1.5: *Conceptual UAV with inflatable wings for MARS exploration, [12].*

1.2.3 History of Inflatable Wings

The first reference to an inflatable wing is found in the patent by Taylor McDaniel for the first rubber glider in April 1930. McDaniel's flight machine, Fig. 1.6 was a glider made by inflatable tubes secured in the fuselage. The control of the aircraft was possible through flexing and wrapping the trailing edge of the inflatable structure. The advantage of this inflatable glider against the wooden gliders of its time was its resilience during a crash, since its lightweight and flexible construction supposed to endure a crash landing. In order to validate the durability, McDaniel made its test pilot to nose dive the aircraft and crash it deliberately to the ground and indeed neither the structure nor the pilot suffered from any damage. Although the first test flights were successful and the glider performed according to plan, there is no documentation that the prototype was evolved further and put into production.

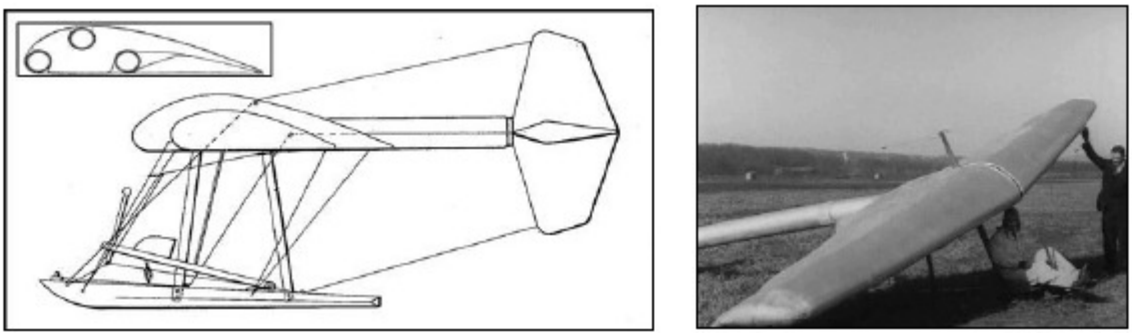

Figure 1.6: *Flying Machine (1930) by Taylor McDaniel.[11].*

For many years, different patents and experiments were made but no prototype was constructed until 1950 and the first successful inflatable winged flight is that of the Goodyear's Inflatoplane, Fig. 1.7. This project was carried out from the aviation department of Goodyear after the USA army requested a solution for pilots trapped behind enemy lines. The idea was that the inflatoplane would be dropped to the sight of the crash in a container in its deflated state, in which even one man could carry it. Then, the pilot would inflate it and use it to return to safety. Its cruise speed was 60 mph, with a range of 390 miles and an endurance of 6.5 hours, while carrying a maximum weight of 240 lbs.

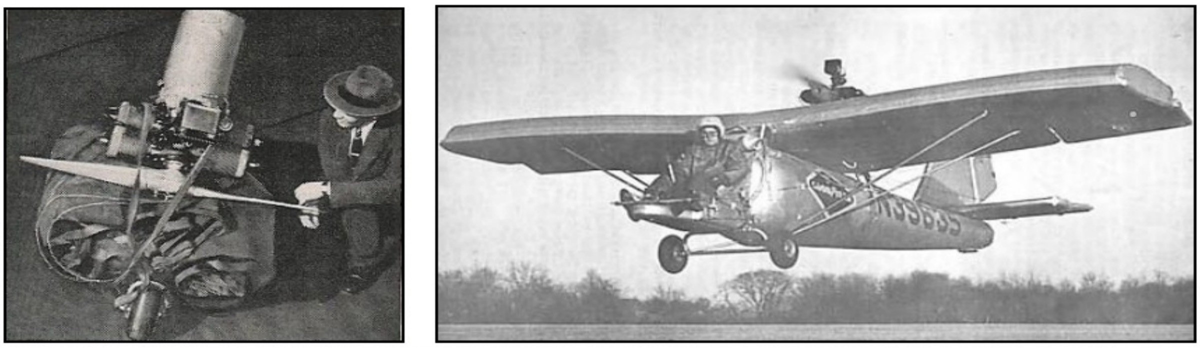

Figure 1.7: *Goodyear's Inflatoplane. Left: The inflatoplane in the deflated state. Right: The inflatoplane during test flight.[11].*

The inflatoplane was tested in Langley full-scale wind tunnel (NASA), Fig. 1.8, in order to determine the aerodynamic and structural deflection characteristics over a range of velocities and load factors. The airplane was longitudinally stable and had adequate pitch and roll control and normal stall characteristics at the lower speeds giving maximum load factors between 1 and 1.5. However, as speed increased, aeroelastic effects associated with the wing twist caused an increase in the lift-curve slope and loss of stability near the stall. For speeds over 70mph and an altitude producing a load factor just above 2, a column-type buckling occurred on the inboard wing panel with one section folding up and hitting the engine mounted above the wing. A total of twelve planes were constructed until 1972, when the USA cancelled the project since no practical use could be found, [13].

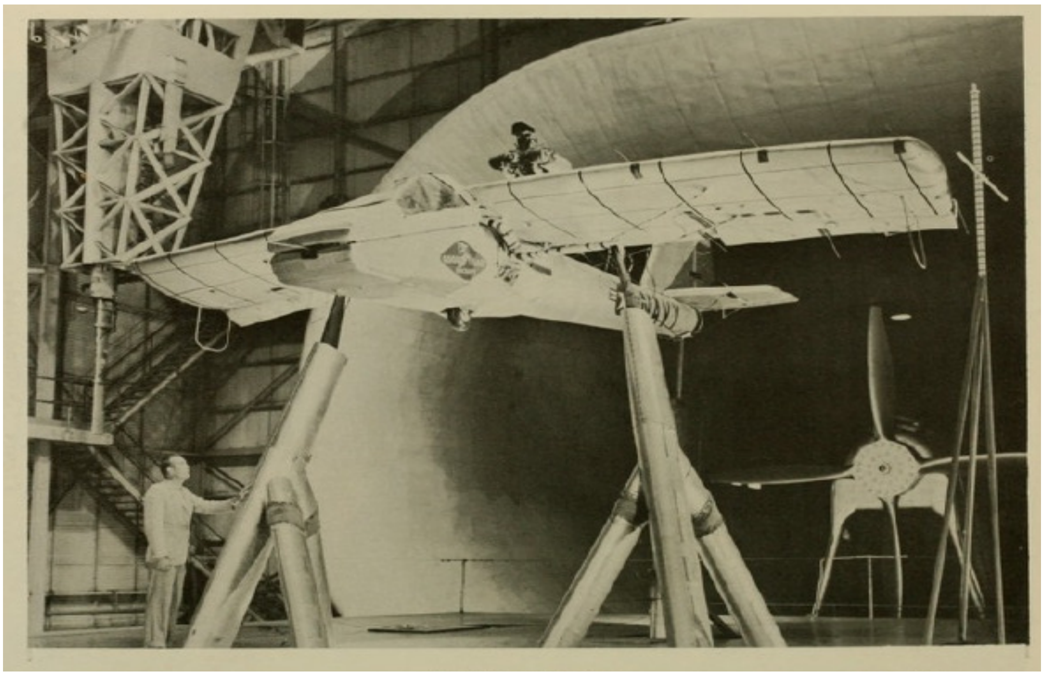

Figure 1.8: *Goodyear's Inflatoplane in the Langley Wind tunnel, [11].*

In 1970, the first UAV with inflatable wings was demonstrated by the ILC Dover, Inc. Apteron was a 5-ft span flying wing UAV designed to be stored in a small volume for ease of portability and launched from any remote location. The entire aircraft, weighed 7 lbs, was powered by a 0.5 hp engine, and was remotely controlled via elevons mounted at the trailing edge. Although this was considered a success during flight demonstrations, Apteron was never put into production.

In 2001, researchers at the NASA Dryden Flight Research Centre created and flown a small-scale (15-25lbs), instrumented, research aircraft configured with inflatable wing in order to investigate its flight characteristics. The inflatable wings used in this program were designed and fabricated by Vertigo, Inco (Lake Elsinore, California) for a U.S. Navy program. They contained five inflatable, cylindrical spars that run spanwise from tip to tip. The spars were made of spirally braided Vectran threads (a Celanese AG product) laid over a urethane gas barrier. A fabric webbing spar cap was aligned on the top and bottom of each of the spars. The wing span is 64 in. tip to tip, and the chord is 7.25 in. The airfoil was relatively thick, symmetric section of a NACA-0012. The wing did not contain any control surfaces and control was carried out by the empennage. A manifold at the centre of the wing hold the wing spars in position and provides a rigid connection between the high-pressure gas source and the wing spars. The basic concept was that the UAV would be launched from a carrier aircraft at a low altitude and, at first, would fly without any wing structure until the pilot initiate the wing inflation procedure and the wings inflate to the designed pressure. After that, the pilot would flight the aircraft and land it successfully, Fig. 1.9.

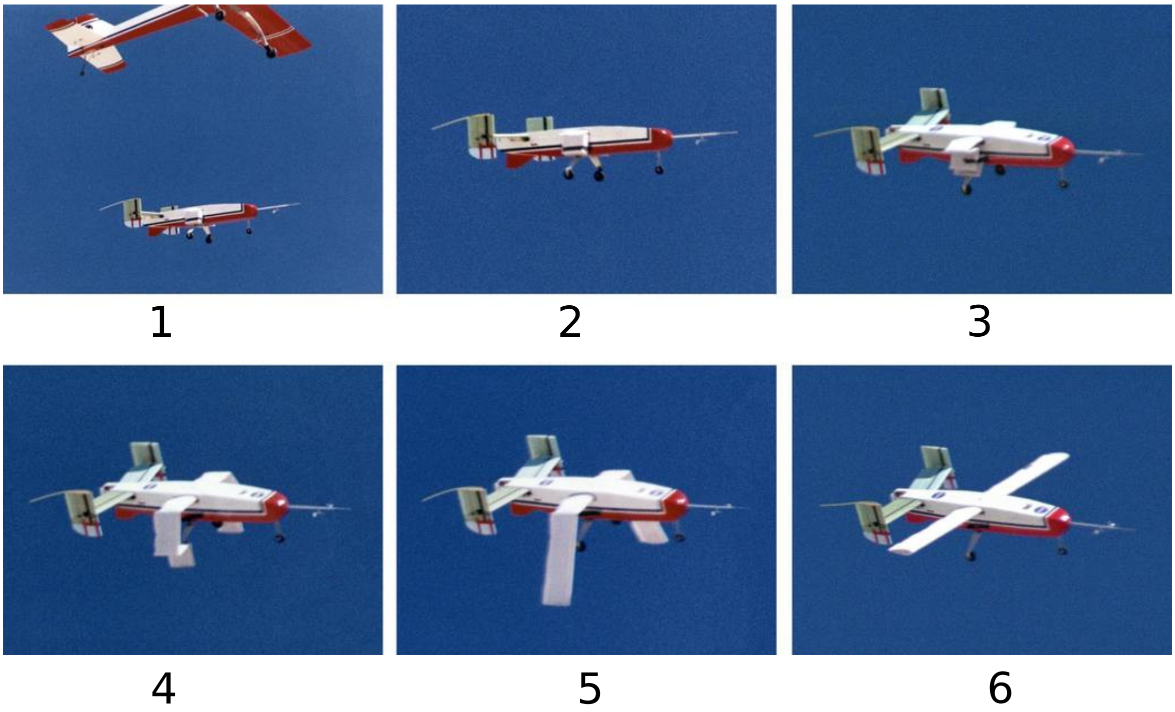

Figure 1.9: *Deployment of NASA I-2000 inflatable wing, Figure 1 shows the release of the carrier. Figure 2 flight without wings. Figures 3-5 the inflating sequence. Figure 6 the fully inflated wing, [14].*

Three flight operations were conducted to demonstrate the in-flight inflation capability of the I-2000 and document the wing and vehicle dynamic response during inflation and transition to lifting flight and the following conclusions were made, [14]:

1)Integration of the inflatable wing test article into a research aircraft configuration is possible at small scale. Powered flight, using only the control surfaces on the tail of the aircraft, was demonstrated.

2)The asymmetric twist distribution of the inflatable wing required significant differential elevon deflection to achieve trimmed flight. A small trim tab on one wing was sufficient to achieve trimmed flight.

3)The feasibility of airdrop and in-flight inflation of the wing, with transition to controlled lifting flight, was demonstrated. Wing inflation and transition to lifting flight was rapid; vehicle dynamic response was benign and limited primarily to roll and heave motions. No indications of instability or divergence were evident.

4)Mechanics of materials analytical methods were effective in modelling the multiple-spar wing configuration for a range of inflation pressures.

Also some notable tries in the history of inflatable wings was made by a Swiss company named Prospective Concepts AG, which developed two manned inflatable aircraft. First, in 1998, it revealed the Stingray, which had a revolutionary wing that derived its rigidity from compressed air. The second concept was the Pneuwing, which was made by the combination of coated high-strength materials and air pressure which gave the wing its strength. Inside the wing, there was no rigid structure to support it. Furthermore, the aircraft was controlled by the ailerons, which were operated in the traditional way by means of wires, the landing flaps changed their curvature by varying the air pressure, which was a plus for the aerodynamics. However, neither of these projects was evolved and no further work was done.

In the recent years, only one company, ILC Dover, is still developing inflatable wings which in cooperation with the University of Kentucky undertook the Big Blue project for creating a inflatable wing appropriate for an UAV, which would be used for space exploration. This project had the objective to investigate the use of new materials for the inflatable wings which, in the early state are flexible and can be stowed efficiently, then they would inflate, in order to take their airfoil shape and in the final phase, a special curable resin would help them to become rigid. (Big Blue experiments 1 and 2). For that reason, the inflatable wings were made from Vectran and a special UV-curable (ultra-violet) resin would be applied after the inflation, [1]. Different aspects of the Big Blue project are shown in Fig. 1.10.

Figure 1.10: *Big Blue Project, BIG BLUE II aircraft and attached inflation system at the recovery site (left). BIG BLUE 3 pre-inflated (middle) and post-inflated (right) at maximum altitude.*

However, after identifying several problems with the resin, the next two experiments (Big Blue 3 and 4) were carried out with inflatable wings which were made from Vectran and gained their structural rigidity from the pressurized air contained. The objective of those two experiments was to determine different internal pressures and NACA profiles. Lastly, the Big Blue 5 experiment was carried out in order to verify the feasibility of inflatable wings for flight in high altitude with very low density air. All experiments but Big Blue 5 were successful, helping to understand how an inflatable wing can be modelled and to monitor different behaviours occurring during the flight of such a structure, [1].

Except of the use of inflatable wings in UAVs and, possible, in an aircraft, there is a new field in which this could be used, that of the renewable energy. This is the case in this diploma thesis. Specifically, recent years research is being carried out in order to find ways to produce energy using methods, which do not produce any kind of waste. There are several new ideas, which incorporate inflatable structures and could contribute to the production of energy. The basic concept is that, at high altitude, the air velocity is higher and more persistent, as a result a wind turbine operating at this altitude would be much more efficient than one operating at the ground, Fig. 1.11. However, those concepts include challenges such as safely suspending and maintaining wind turbines in high altitudes, capable of dealing with different conditions. In projects like that the challenge is to be able to predict, from the design phase, the behaviour of such structure and especially the wing, since aerodynamic loads change radically and, as several researches had shown, inflatable structures are susceptible to aeroelastic problems.

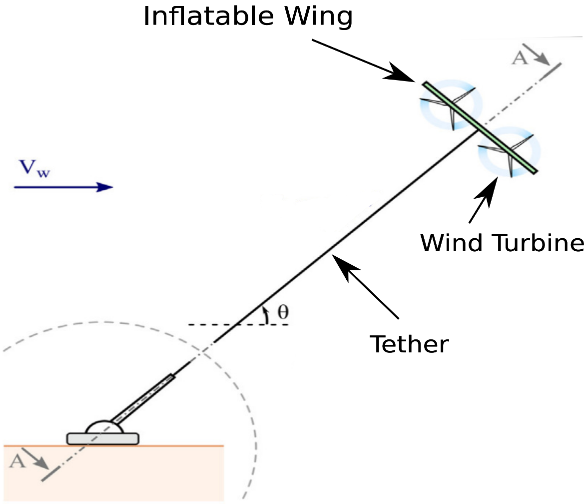

Figure 1.11: *Airborne Wind Turbine, The wind turbine is attached to the inflatable wing and the whole structure is held by the tether which acts also as the cable transferring the produced electricity, [15].*

1.3 Thesis Outline

The chapters of this diploma thesis are the following:

- **Chapter 2** Presentation of flow equations, focusing on the RANS equation used in the GPU-enabled PUMA s/w for the aerodynamic loads computation.
- **Chapter 3** Presentation of basic structural equations, used by the commercial structural solver, for the deformation computation.
- **Chapter 4** Presentation of the basic categorization of fluid-structure methods. Also in this chapter the tools used for the interpolation of values between the different solvers are presented.
- **Chapter 5** Presentation of the workflow used in this thesis for the aeroelastic cycles.
- **Chapter 6** Aeroelastic applications on different inflatable wings shapes and geometries.
- **Chapter 7** Overview and Conclusions.

Chapter 2

Aerodynamic Analysis

The flow model used to compute the aerodynamic loads is presented first. The flow model consists of the steady-state Reynolds–Averaged Navier–Stokes (RANS) equations for compressible flow and the Spalart–Allmaras turbulence model (to effect closure in turbulent flows),[16]. The CFD solver together with its adjoint counterpart is called PUMA (**P**arallel solver, for **U**nstructured grids, for **M**ulti-blade row computations, including **A**djoint). Code development started about two decades ago in the framework of a number of PhD theses in the PCOpt/NTUA and, during the last decade, it has been transferred to NVIDIA-GPUs and enriched with new features and capabilities. All runs executed during this thesis were executed using exclusively with the GPU-enabled variant of PUMA, [17],[18].

2.1 The RANS Equations for Compressible Flow

The 3D RANS equations for compressible fluid flows, in vector form,[16]

$$\frac{\partial U_n}{\partial t} + \frac{\partial f_{nk}^{inv}}{\partial x_k} - \frac{\partial f_{nk}^{vis}}{\partial x_k} = 0 \qquad (2.1)$$

In Eq. 2.1 , U_n stands for the conservative flow variables array namely $U_n = [\rho\ \rho u_1\ \rho u_2\ \rho u_3\ \rho u_3\ \rho E]$, with ρ being the fluid density, $u_m (m = 1, 2, 3)$ being the velocity components and E the energy per unit mass. The inviscid fluxes f_{nk}^{inv} and the viscous fluxes f_{nk}^{vis} (the Einstein summation convention for repeated indices is applied) are defined as:

$$f_{nk}^{inv} = \begin{bmatrix} \rho u_k \\ \rho u_1 u_k + p\delta_{1k} \\ \rho u_2 u_k + p\delta_{2k} \\ \rho u_3 u_k + p\delta_{3k} \\ u_k(E_t + p) \end{bmatrix}, \; f_{nk}^{vis} = \begin{bmatrix} 0 \\ \tau_{1k} \\ \tau_{2k} \\ \tau_{3k} \\ u_l \tau_{l,k} + q_k \end{bmatrix} \tag{2.2}$$

where the δ_{nk} is the Kronecker symbol, $E_t = \frac{p}{\gamma - 1} - \frac{1}{2}\rho u^2$ the total energy per unit volume, q_k the thermal flux components and τ_{ik} are viscous and turbulent stresses. In the rest of this thesis the velocity vector is represented **u**. Eq. 2.2 are supplemented by the following definitions[16]

- (i, j) component of the viscous stress tensor (τ_{ij}) for Newtonian fluids:

$$\tau_{ij} = \frac{\mu + \mu_t}{Re} \left(\frac{\partial u_i}{\partial x_j} + \frac{\partial u_j}{\partial x_j} - \frac{2}{3}\delta_{ij} \frac{\partial u_k}{\partial x_k} \right) \tag{2.3}$$

- Reynolds number (Re)

$$Re = \frac{\rho u l}{\mu} \tag{2.4}$$

  where ρ is the density of the fluid, l the characteristics length, in our case the chord width of the airfoil and μ the molecular viscosity of the fluid.

- k component of the heat flux (q_k):

$$q_k = \frac{C_p}{Re} \left(\frac{\mu}{Pr} + \frac{\mu_t}{Pr_t} \right) \frac{\partial T}{\partial x_l} \tag{2.5}$$

  where C_p is the specific heat under constant pressure.

- Static temperature (T). Since the fluid is assumed to be a perfect gas, T is related to pressure and density through the equation of state:

$$p = \rho R_g T, \tag{2.6}$$

  where R_g is the specific gas constant.

- Prandtl number (Pr):

$$Pr = \frac{C_p \mu}{k} \tag{2.7}$$

  where k the thermal conductivity.

- Turbulent Prandtl number (Pr_t)

- Specific heat ratio (γ):

$$\gamma = \frac{C_p}{C_v} \tag{2.8}$$

where C_v is the specific heat for constant volume.

- Total or stagnation enthalpy (h_t):

$$h_t = E + \frac{p}{\rho} \tag{2.9}$$

For perfect gas, the total enthalpy is linked to pressure (p), density (ρ) and velocity (u_m) through:

$$h_t = \frac{\gamma p}{\rho(\gamma - 1)} + \frac{1}{2} u_m^2 \tag{2.10}$$

- Total or stagnation temperature (T_t):

$$T_t = T + \frac{u_m u_m}{2C_p} \tag{2.11}$$

- Total or stagnation pressure for perfect gases (p_t):

$$p_t = p \left(1 + \frac{\gamma - 1}{2} M^2 \right)^{\frac{\gamma}{\gamma - 1}} \tag{2.12}$$

The turbulence viscosity μ_t is computed employing the one-equation Spalart-Allmaras turbulence model. According to this model, an additional PDE for the turbulence field $\tilde{\nu}$, namely [19]

$$\begin{aligned} \frac{\partial\left(\rho\tilde{\nu}\right)}{\partial t} + \frac{\partial(\rho\tilde{\nu}u_k)}{\partial x_k} = \frac{\rho}{Re_0 \sigma} \left\{ \frac{\partial}{\partial x_k} \left[(\tilde{\nu} + \nu) \frac{\partial \tilde{\nu}}{\partial x_k} \right] + c_{b_2} \frac{\partial \tilde{\nu}}{\partial x_k} \frac{\partial \tilde{\nu}}{\partial x_k} \right\} \\ + \rho c_{b_1} (1 - f_{t_2}) \tilde{S} \tilde{\nu} - \frac{\rho}{Re_0} \left(c_{w_1} f_w - \frac{c_{b_1}}{\varkappa^2} f_{t_2} \right) \left(\frac{\tilde{\nu}}{\Delta} \right)^2 \end{aligned} \tag{2.13}$$

where Δ stands for the distance of each point within the flow domain from the closest wall boundary. Solving 2.13, μ_t is computed from $\tilde{\nu}$ by $\mu_t = \rho\tilde{\nu} f_{v_1}$. Equation

2.13 is supplemented by the following relations and constants [19]:

$$
\begin{aligned}
&\chi = \frac{\tilde{\nu}}{\nu},\ f_{u_1} = \frac{\chi^3}{\chi^3 + {c_{v_1}}^3},\ f_{u_2} = 1 - \frac{\chi}{1 + \chi f_{u_1}},\ S = \sqrt{\varepsilon_{klm}\varepsilon_{kqr}\frac{\partial u_m}{\partial x_l}\frac{\partial u_r}{\partial x_q}},\\
&\tilde{S} = S + \frac{\tilde{\nu} f_{u_2}}{Re_0 \varkappa^2 \Delta},\ f_w = g\left(\frac{1 + c_{w_3}^6}{g^6 + c_{w_3}^6}\right)^{\frac{1}{3}},\ g = r + c_{w_2}\left(r^6 - r\right),\\
&r = min\left(10, \frac{\tilde{\nu}}{Re_0 \tilde{S} \varkappa^2 \Delta^2}\right),\ \tilde{\mu} = \rho\tilde{\nu},\ f_{t_2} = c_{t_3} e^{c_{t_4}\chi^2},\\
&c_{v_1} = 7.1,\ c_{b_1} = 0.1355,\ c_{b_2} = 0.622,\ c_{w_1} = \frac{c_{b_1}}{\varkappa^2} + \frac{1 + c_{b_2}}{\sigma},\\
&c_{w_2} = 0.3,\ c_{w_3} = 2.0,\ \sigma = \frac{2}{3},\ \varkappa = 0.41,\ c_{t_3} = 1.2,\ c_{t_4} = 0.5
\end{aligned}
\tag{2.14}
$$

The equations are solved on unstructured grids (in 3D, such a grid may contain tetrahedra, pyramids, prisms and hexahedra) using the finite-volume method, while the linear system arises from the discretization is solved by the point-implicit (involving internal sub-iterations) Jacobi solver.

Chapter 3

Structural Analysis

In addition to the flow model, the structural model used is presented in this section. The basic principles of the finite element method used by the software, for solving structural problems are introduced and then more details about our problem are given. As a structural solver, the commercial software ANSYS and, specifically, its MAPDL (Mechanical ANSYS Parametric Design Language) counterpart, was used, [20].

3.1 Basic Structural Relationships

Firstly, the stresses, strains and the relationship between them are presented, since they are essential for the finite element method in order to compute structural deformations in any structural problem. In a global coordinate system (x, y, z), it is known that stresses referring to all axes, Fig. 3.1 are defined by the Vector 3.1:[20]

$$\sigma = \begin{bmatrix} \sigma_x \\ \sigma_y \\ \sigma_z \\ \tau_{xy} \\ \tau_{yz} \\ \tau_{zx} \end{bmatrix} \tag{3.1}$$

In this thesis, the materials used are considered to be elastic. The elastic strain

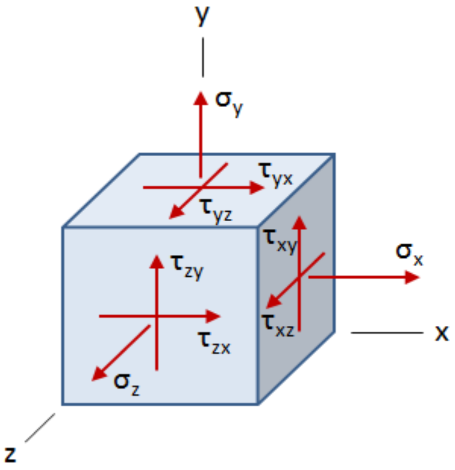

Figure 3.1: *General state of stress, [21].*

vector ε^{el} in the global coordinate system is equal to :

$$\varepsilon^{el} = \varepsilon - \varepsilon^{th} \tag{3.2}$$

with ε representing the total strain vector defined as:

$$\varepsilon = \begin{bmatrix} \varepsilon_x \\ \varepsilon_y \\ \varepsilon_z \\ \gamma_{xy} \\ \gamma_{yz} \\ \gamma_{zx} \end{bmatrix} \tag{3.3}$$

and ε_{th} represents the thermal strain vector which is defined as:

$$\varepsilon^{th} = \Delta T \begin{bmatrix} \alpha_x \\ \alpha_y \\ \alpha_z \\ 0 \\ 0 \\ 0 \end{bmatrix} \tag{3.4}$$

In Eq. 3.4, $\alpha = [\alpha_x \quad \alpha_y \quad \alpha_z]$ is the secant coefficients of thermal expansion in the global coordinate system and $\Delta T = T - T_{ref}$, with T_{ref} the temperature in which no strain occurs. In our analysis the reference temperature is assumed equal to the current so the thermal strain vector is set to zero. As a result the elastic strain would be assumed equal to the total strain. After defining stresses and strains the generalized Hooke's law for elastic material gives the relationship between them:

$$\begin{aligned}\sigma_\chi =&\frac{E_\chi}{h}\left(1-\nu_{yz}^2\frac{E_z}{E_y}\right)\varepsilon_\chi+\frac{E_y}{h}\left(\nu_{xy}+\nu_{xz}\nu_{yz}\frac{E_z}{E_y}\right)\varepsilon_y+\\ &\frac{E_z}{h}\left(\nu_{xz}+\nu_{yz}\nu_{xy}\right)\varepsilon_z\end{aligned}\tag{3.5}$$

$$\begin{aligned}\sigma_y =&\frac{E_y}{h}\left(\nu_{xy}+\nu_{xz}\nu_{yz}\frac{E_z}{E_y}\right)\varepsilon_\chi+\frac{E_y}{h}\left(1-\nu_{xz}^2\frac{E_z}{E_y}\right)\varepsilon_y+\\ &\frac{E_z}{h}\left(\nu_{yz}+\nu_{xz}\nu_{xy}\frac{E_y}{E_x}\right)\varepsilon_z\end{aligned}\tag{3.6}$$

$$\begin{aligned}\sigma_z =&\frac{E_z}{h}\left(\nu_{xz}+\nu_{yz}\nu_{xy}\frac{E_z}{E_y}\right)\varepsilon_\chi+\frac{E_y}{h}\left(\nu_{yz}+\nu_{xz}\nu_{xy}\frac{E_y}{E_x}\right)\varepsilon_y+\\ &\frac{E_z}{h}\left(1-\nu_{xy}^2\frac{E_y}{E_x}\right)\varepsilon_z\end{aligned}\tag{3.7}$$

$$\tau_{xy} = G_{xy}\gamma_{xy}\tag{3.8}$$

$$\tau_{yz} = G_{yz}\gamma_{yz}\tag{3.9}$$

$$\tau_{xz} = G_{xz}\gamma_{xy}\tag{3.10}$$

where,

$$h = 1-\nu_{xy}^2\frac{E_y}{E_x}-\nu_{yz}^2\frac{E_z}{E_y}-\nu_{xz}^2\frac{E_z}{E_x}-2\nu_{xy}\nu_{yz}\nu_{xz}\frac{E_z}{E_x}$$

Hooke's law is supplemented by the following definitions:

- E_i is the elastic modulus or Young modulus along axis i, which is usually defined by experiment for the used material.

- ν_{ij} is the Poisson ratio defined as $\nu_{ij} = -\frac{\varepsilon_j}{\varepsilon_i}$.

- G_{ij} is the shear modulus in direction j on the plane whose normal is in direction i, which in isotropic materials is given by the following relationship $G = \frac{E(1-\nu)}{2(1+\nu)}$ and in other cases is defined by an experiment.

Eqs. from 3.5 through 3.10 could be written in a matrix form as:

$$\sigma = [E]\varepsilon\tag{3.11}$$

with $[E]$ called the elastic stiffness matrix and defined as:

$$[E] = \begin{bmatrix} \frac{1-\nu_x y\nu_{zy}}{E_y E_z \Delta} & \frac{\nu_{xy}+\nu_{zx}\nu_{yz}}{E_y E_z \Delta} & \frac{\nu_{zx}+\nu_{yx}\nu_{zy}}{E_y E_z \Delta} & 0 & 0 & 0 \\ \frac{\nu_{xy}+\nu_{xz}\nu_{zy}}{E_z E_x \Delta} & \frac{1-\nu_{zx}\nu_{zy}}{E_z E_x \Delta} & \frac{\nu_{zy}+\nu_{zx}\nu_{xy}}{E_z E_x \Delta} & 0 & 0 & 0 \\ \frac{\nu_{xz}+\nu_{xy}\nu_{yz}}{E_x E_y \Delta} & \frac{\nu_{yz}+\nu_{xz}\nu_{yx}}{E_x E_y \Delta} & \frac{1-\nu_{xy}\nu_{yx}}{E_x E_y \Delta} & 0 & 0 & 0 \\ 0 & 0 & 0 & 2G_{yz} & 0 & 0 \\ 0 & 0 & 0 & & 2G_{yz} & 0 \\ 0 & 0 & 0 & 0 & 0 & 2G_{yz} \end{bmatrix} \tag{3.12}$$

where Δ is given by:

$$\Delta = \frac{1 - \nu_{xy}\nu_{yx} - \nu_{yz}\nu_{zy} - \nu_{zx}\nu_{xz} - 2\nu_{xy}\nu_{yz}\nu_{zx}}{E_x E_y E_z}$$

After defining the stresses, strains and the relationship between them for any elastic material and coordinate system, the simplified relationships for an isotropic elastic material is defined since, in our study, this kind of material is used. An isotropic material has the same properties in every direction.

- In this case, the normal strains are expressed as:

  $$\varepsilon_x = \frac{\partial u}{\partial x},\ \varepsilon_y = \frac{\partial v}{\partial y},\ \varepsilon_z = \frac{\partial w}{\partial z} \tag{3.13}$$

  where u,v,w are the displacements in the x, y, z direction accordingly.

- The shear strains are expressed as:

  $$\gamma_{xy} = \frac{\partial u}{\partial y} + \frac{\partial v}{\partial x},\ \gamma_{yz} = \frac{\partial v}{\partial z} + \frac{\partial w}{\partial y},\ \gamma_{zx} = \frac{\partial w}{\partial x} + \frac{\partial u}{\partial z}, \tag{3.14}$$

Also, Eqs. 3.5 through 3.10 are simplified as:

$$\begin{aligned} \varepsilon_x &= \frac{1}{E}\left[\sigma_x - \nu(\sigma_y + \sigma_z)\right], \\ \varepsilon_y &= \frac{1}{E}\left[\sigma_y - \nu(\sigma_x + \sigma_z)\right], \\ \varepsilon_z &= \frac{1}{E}\left[\sigma_z - \nu(\sigma_y + \sigma_x)\right], \\ \gamma_{xy} &= \frac{\tau_{xy}}{G},\ \gamma_{yz} = \frac{\tau_{yz}}{G},\ \gamma_{zx} = \frac{\tau_{zx}}{G} \end{aligned} \tag{3.15}$$

Eq. 3.15 is supplemented by the following definitions:

- E is the Young modulus which, in this case, is constant and equal for all directions.
- ν is the Poisson ratio defined as $\nu = \nu_{xy} = -\frac{\varepsilon_y}{\varepsilon_x}$ and is the same in all directions.
- G is the shear modulus which, in isotropic materials, is given by the following relationship $G = \frac{E(1-\nu)}{2(1+\nu)}$.

As a result, the Hooke's law in matrix form can be written as:

$$\sigma = \begin{bmatrix} \sigma_x \\ \sigma_y \\ \sigma_z \\ \tau_{xy} \\ \tau_{yz} \\ \tau_{zx} \end{bmatrix} = \begin{bmatrix} \overline{\nu} & \overline{\mu} & \overline{\mu} & 0 & 0 & 0 \\ \overline{\mu} & \overline{\nu} & \overline{\mu} & 0 & 0 & 0 \\ \overline{\mu} & \overline{\mu} & \overline{\nu} & 0 & 0 & 0 \\ 0 & 0 & 0 & G & 0 & 0 \\ 0 & 0 & 0 & 0 & G & 0 \\ 0 & 0 & 0 & 0 & 0 & G \end{bmatrix} \begin{bmatrix} \varepsilon_x \\ \varepsilon_y \\ \varepsilon_z \\ \gamma_{xy} \\ \gamma_{yz} \\ \gamma_{zx} \end{bmatrix} \tag{3.16}$$

where

$$\overline{\nu} = \frac{E(1-\nu)}{(1+\nu)(1-2\nu)} \qquad \text{and} \qquad \overline{\mu} = \frac{E\nu}{2(1+\nu)} \tag{3.17}$$

So again, the relationship between stresses and strains has the form $\sigma = [E]\varepsilon$ but it is now more simplified than before. These relationships are used in the finite element method in order to solve a variety of structural problems.

3.2 Principle of Virtual Work

3.2.1 Problem Statement

The finite element method, [20], is based on the principle of virtual work. This principle is used for computing stresses and deformations in structures since it enables simpler equations than the classic Newton method. The basic idea is that a virtual (very small) displacement δu results in a virtual (very small) work δW caused by the applied external forces:

$$\delta W = \delta U \tag{3.18}$$

where:

- U is the strain energy (internal work).

- W is the external work caused from the external loads applied to the structure.

- δ is the virtual operator.

Considering a 3D elastic body (the geometry of which is given) subjected to surface forces $p = [p_x \quad p_y \quad p_z]$ and body forces $F = [F_x \quad F_y \quad F_z]$. In addition, supports are specified on some surface area. For given applied loads, displacements, boundary conditions and material stress-strain law, the purpose is to compute the displacement field for the body. Firstly, the elastic energy in equilibrium is defined as:

$$U_{eq} = \frac{1}{2} \iiint_V \sigma^T \varepsilon dV = \frac{1}{2} \iiint_V \varepsilon^T [E] \varepsilon dV \tag{3.19}$$

Let us consider a small displacement for the whole body volume and for the surface area where surface forces are applied, the resulting strains are given by Eq 3.20:

$$U_{dis} = \frac{1}{2} \int_V \sigma^T \left(\varepsilon + \delta\varepsilon\right) dV = \frac{1}{2} \int_V \left(\varepsilon + \delta\varepsilon\right)^T [E] \left(\varepsilon + \delta\varepsilon\right) dV \tag{3.20}$$

Since $\delta U = U_{dis} - U_{eq}$, replacing with Eqs. 3.19 and 3.20 and neglecting the term $(\delta\varepsilon)^2$ concludes:

$$\delta U = \iiint_V \delta\varepsilon^T [E] \varepsilon dV \tag{3.21}$$

After defining the virtual internal work the external work caused by applied surface and body loads should be defined. At first the surface loads contribution to the total virtual work could be written as:

$$F_{surf} = \oint_S \delta u^T p dS \tag{3.22}$$

where p is the vector of surface loads. Also, the body force contribution could be written as:

$$F_{body} = \iiint_V \delta u^T F dV \tag{3.23}$$

where F is the vector of body loads. Combining Eqs. 3.18, 3.4 and 3.23 concludes at:

$$\iiint_V \delta\varepsilon^T [E] \varepsilon dV = \oint_S \delta u^T p dS + \iiint_V \delta u^T F dV \tag{3.24}$$

3.2.2 Finite Element Equations

In order to present the use of the principle work in the finite element method a random 3D element will be used. The displacement of each node is defined as the following vector:

$$u_{node} = [u_1 \quad v_1 \quad w_1 \quad u_2 \quad v_2 \quad w_2 \quad \cdots] \tag{3.25}$$

Displacements at some point inside the finite element can be determined with the use of nodal displacements u_{node} and shape functions N_i. Shape functions are basically polynomial expressions that define the contribution of each node to the displacement inside the finite element, [22] and can be written in a matrix form as, 3.26:

$$[N] = \begin{bmatrix} N_1 & 0 & 0 & N_2 & \cdots \\ 0 & N_1 & 0 & 0 & \cdots \\ 0 & 0 & N_1 & 0 & \cdots \end{bmatrix} \tag{3.26}$$

The strain vector can also be determined through displacements at nodal points:

$$\varepsilon = [B]u_{node} \tag{3.27}$$

with

$$[B] = [L][N] \tag{3.28}$$

which is called the displacement differentiation matrix and is defined by Eq. 3.26 and $[L]$ which is the matrix differentiation operator defined as:

$$[L] = \begin{bmatrix} \frac{\partial}{\partial x} & 0 & 0 \\ 0 & \frac{\partial}{\partial y} & 0 \\ 0 & 0 & \frac{\partial}{\partial z} \\ \frac{\partial}{\partial y} & \frac{\partial}{\partial x} & 0 \\ 0 & \frac{\partial}{\partial z} & \frac{\partial}{\partial y} \\ \frac{\partial}{\partial z} & 0 & \frac{\partial}{\partial x} \end{bmatrix} \tag{3.29}$$

So, the $[B]$ is defined as:

$$[B_i] = \begin{bmatrix} \frac{\partial N_i}{\partial x} & 0 & 0 \\ 0 & \frac{\partial N_i}{\partial y} & 0 \\ 0 & 0 & \frac{\partial N_i}{\partial z} \\ \frac{\partial N_i}{\partial y} & \frac{\partial N_i}{\partial x} & 0 \\ 0 & \frac{\partial N_i}{\partial z} & \frac{\partial N_i}{\partial y} \\ \frac{\partial N_i}{\partial z} & 0 & \frac{\partial N_i}{\partial x} \end{bmatrix} \tag{3.30}$$

Also, by the definition of the shape functions, the displacement vector in some point inside the element can be written as:

$$u = [N]u_{node} \tag{3.31}$$

Substituting the above at the Eq. 3.24 with respect to the nodal displacements concludes at:

$$\left(\int_V [B]^T[E][B]dV\right) u_{node} = \int_S [N]^T pdS + \int_V [N]^T FdV \tag{3.32}$$

or

$$[K]\, u_{node} = \int_S [N]^T pdS + \int_V [N]^T FdV \tag{3.33}$$

with

$$[K] = \int_V [B]^T[E][B]dV \tag{3.34}$$

3.3 Bar Element Model

In this thesis, the tethers supporting the inflatable wing are modelled as bar elements and their basic relationships are presented below. Equations presented below apply for a two node bar. Firstly, a function should be defined, which describes the profile of the bar displacement. For a two-node element, the displacement, expressed in the local coordinate system could be interpolated by a polynomial expression, Eq. 3.35: [22]

$$u(s) = a_0 + a_1 s \tag{3.35}$$

By solving Eq. 3.35 along the element concludes in:

$$\begin{bmatrix} u_I \\ u_J \end{bmatrix} = \begin{bmatrix} 1 & -1 \\ 1 & 1 \end{bmatrix} \begin{bmatrix} a_0 \\ a_1 \end{bmatrix} \implies$$

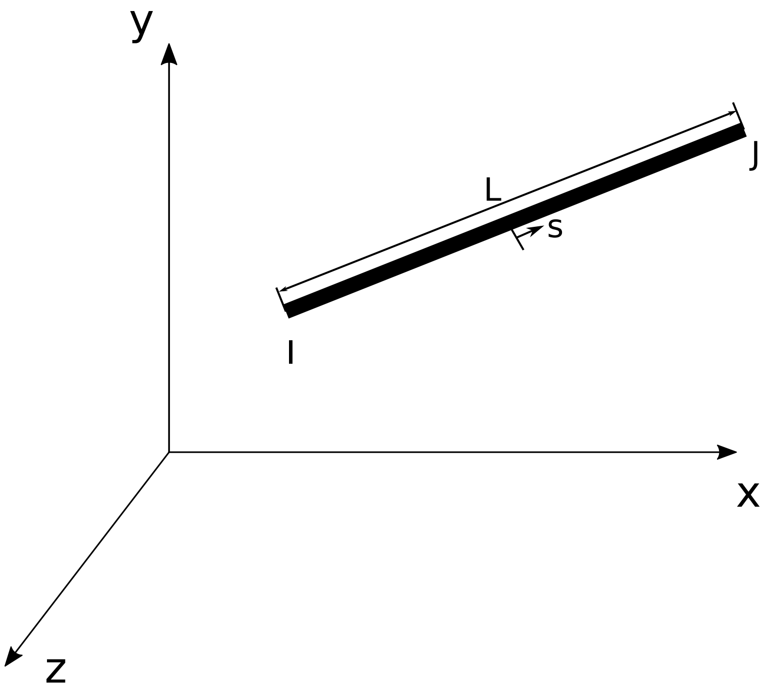

Figure 3.2: *A 2-node 3D bar element.*

$$\begin{bmatrix} a_0 \\ a_1 \end{bmatrix} = \frac{1}{2} \begin{bmatrix} 1 & 1 \\ -1 & 1 \end{bmatrix} \begin{bmatrix} u_I \\ u_J \end{bmatrix} \tag{3.36}$$

Introducing Eq. 3.36 into 3.35 concludes at:

$$\begin{aligned} u(s) &= u_I \underbrace{\frac{(1-s)}{2}}_{N_1} + u_J \underbrace{\frac{(1+s)}{2}}_{N_2} \\ u(s) &= u_I N_1(s) + u_J N_2(s) \\ u(s) &= \sum_{i=1}^{2} N_i(s) u_i \end{aligned} \tag{3.37}$$

$N_i(s)$ are referred to as shape functions and describe the displacement along the bar. In this case, the strain can be easily defined as:

$$\varepsilon = \frac{\partial u(s)}{\partial s} = \frac{u_J - u_I}{2}$$

Matrix $[B]$ is defined in Eq. 3.28 and in this case is expressed as $[B] = [-1 \quad 1]$. The stiffness matrix can be defined by using the principle of virtual work, 3.34:

$$[K] = \frac{1}{L}\int_0^1 [B]^T E[B]ds = \frac{A}{L}\int_0^1 [-1 \quad 1]^T E[-1 \quad 1]ds = \frac{AE}{L}\begin{bmatrix} 1 & -1 \\ -1 & 1 \end{bmatrix} \tag{3.38}$$

where A is the cross section of the bar. After finding the stiffness matrix of the bar in the local coordinate system it can easily be transformed in the global coordinate system, with the help of a transformation matrix. After, obtaining the stiffness matrix of the element in the global coordinate system, the assembly of the elements can be performed and the solution can be achieved.

3.4 4 -Node Finite Element

In this thesis, the inflatable wing configuration is modelled by 4-node finite elements and in this section their basic relationships are presented. After using the principle of virtual work to solve a simple bar element, the shape functions and stiffness matrix of a 4-node element will be defined. The shape function for a 4-node element is written with two others variables (s,t) instead of (x,y), which result from non-dimensionalization. In the new coordinate system the position of the four corners of the element are shown in Fig. 3.3.

So, following the same technique as in the beam element, the first displacement is interpolated with a polynomial expression with four variables:[20]

$$u(s,t) = a_0 + a_1 s + a_2 t + a_3 st \tag{3.39}$$

For the four corners of the element:

$$\begin{bmatrix} u_I \\ u_J \\ u_K \\ u_L \end{bmatrix} = \begin{bmatrix} 1 & -1 & -1 & 1 \\ 1 & 1 & -1 & -1 \\ 1 & 1 & 1 & 1 \\ 1 & -1 & 1 & -1 \end{bmatrix} \begin{bmatrix} a_0 \\ a_1 \\ a_2 \\ a_3 \end{bmatrix} \Longrightarrow$$

$$\begin{bmatrix} a_0 \\ a_1 \\ a_2 \\ a_3 \end{bmatrix} = \frac{1}{4}\begin{bmatrix} 1 & 1 & 1 & 1 \\ -1 & 1 & 1 & -1 \\ -1 & -1 & 1 & 1 \\ 1 & -1 & 1 & -1 \end{bmatrix} \begin{bmatrix} u_I \\ u_J \\ u_K \\ u_L \end{bmatrix} \tag{3.40}$$

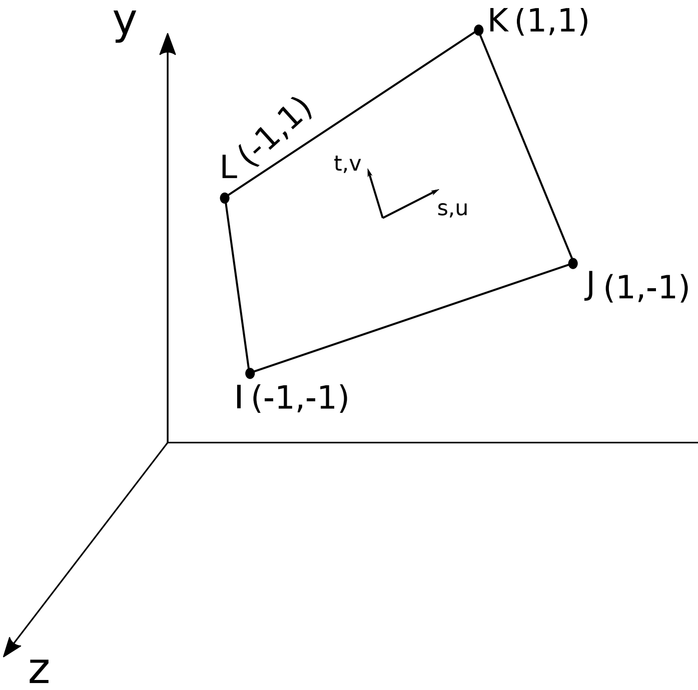

Figure 3.3: *4-Node Finite Element.*

Introducing Eq. 3.40 into 3.39 concludes at:

$$u(s,t) = u_I \underbrace{\frac{(1-s)(1-t)}{4}}_{N_1} + u_J \underbrace{\frac{(1+s)(1-t)}{4}}_{N_2} + u_K \underbrace{\frac{(1+s)(1+t)}{4}}_{N_3} + u_L \underbrace{\frac{(1-s)(1+t)}{4}}_{N_4}$$

$$u(s,t) = u_I N_1(s,t) + u_J N_2(s,t) + u_K N_3(s,t) + u_L N_4(s,t)$$

$$u(s,t) = \sum_{i=1}^{4} N_i(s,t) u_i \tag{3.41}$$

The same applies for all the rotations and translations of the element $[u, \quad v, \quad w, \quad \theta_x, \quad \theta_y, \quad \theta_z]$. The stiffness matrix can be defined by using the principle of virtual work, 3.34:

$$[K] = \iint_A [B]^T [E][B] dxdy \tag{3.42}$$

Matrix $[B]$ is defined in Eq. 3.28 as $[B] = [L][N]$. Matrix $[L]$, Eq. 3.29, in a two dimensional element is simplified:

$$[L] = \begin{bmatrix} \frac{\partial}{\partial x} & 0 & 0 \\ 0 & \frac{\partial}{\partial y} & 0 \\ \frac{\partial}{\partial y} & \frac{\partial}{\partial x} & 0 \end{bmatrix} \tag{3.43}$$

Matrix $[N]$, Eq. 3.26, for a 4-node element is simplified:

$$[N] = \begin{bmatrix} N_1 & 0 & 0 & N_2 & 0 & 0 & N_3 & 0 & 0 & N_4 & 0 & 0 \\ 0 & N_1 & 0 & 0 & N_2 & 0 & 0 & N_3 & 0 & 0 & N_4 & 0 \\ 0 & 0 & N_1 & 0 & 0 & N_2 & 0 & 0 & N_3 & 0 & 0 & N_4 \end{bmatrix} \tag{3.44}$$

Also, [E] is the elastic matrix defined by Eq. 3.12. Since shape functions are defined with respect to the (s,t), a transformation from (x,y) to (s,t) must be performed.

$$\begin{bmatrix} \dfrac{\partial N}{\partial s} \\ \dfrac{\partial N}{\partial t} \end{bmatrix} = \underbrace{\begin{bmatrix} \dfrac{\partial x}{\partial s} & \dfrac{\partial y}{\partial s} \\ \dfrac{\partial x}{\partial t} & \dfrac{\partial y}{\partial t} \end{bmatrix}}_{[J]} \begin{bmatrix} \dfrac{\partial N}{\partial x} \\ \dfrac{\partial N}{\partial y} \end{bmatrix} \tag{3.45}$$

Differentiating the Eq. 3.4 we have:

$$\left.\begin{aligned} \frac{\partial x}{\partial s} &= \sum_{i=1}^{4} \frac{N_i(s,t)}{\partial s} x_i, \quad \frac{\partial y}{\partial s} = \sum_{i=1}^{4} \frac{N_i(s,t)}{\partial s} y_i \\ \frac{\partial x}{\partial t} &= \sum_{i=1}^{4} \frac{N_i(s,t)}{\partial t} x_i, \quad \frac{\partial y}{\partial t} = \sum_{i=1}^{4} \frac{N_i(s,t)}{\partial t} y_i \end{aligned}\right\} \tag{3.46}$$

$$\begin{bmatrix} \dfrac{\partial N}{\partial x} \\ \dfrac{\partial N}{\partial y} \end{bmatrix} = [J]^{-1} \begin{bmatrix} \dfrac{\partial N}{\partial s} \\ \dfrac{\partial N}{\partial t} \end{bmatrix} \tag{3.47}$$

with $[J]^{-1}$ the inverse matrix. By using the above relationships we conclude that stiffness matrix, $[B]$ is given by the Eq. 3.48:

$$[K] = \iint_A [B]^T [E][B] dxdy = \int_{-1}^{1} \int_{-1}^{1} \underbrace{[B]^T [E][B]}_{f(s,t)} detJdsdt \tag{3.48}$$

Same as before, after defining the stiffness matrix, the boundary conditions and the external forces could be applied. Finally, the assembly of all elements can be performed and the problem can be solved.

Chapter 4

Fluid-Structure Interaction

Fluid Structure Interaction (FSI) involves the coupling of fluid dynamics and structural mechanics disciplines, in systems which involve the structure of a body and the surrounding fluid. Fluid flow around any structure exerts aerodynamic forces which cause the deformation of it. The new deformed structure has impact on the fluid flow due to geometry changes and, as a result, the aerodynamic forces change again. The whole system is solved iteratively, till the equilibrium, in order to define the behaviour of the structure due to the aerodynamic loads. FSI is a crucial consideration in the design of many engineering systems, e.g. aircraft, spacecraft, engines, etc.

4.1 FSI Approaches

FSI methods are divided into two large categories based on the solution procedure employed. One option is to solve the fluid and the structural equations simultaneously, with a single solver. This approach is called **monolithic** and requires a code developed especially for this particular combination of physical problems. This method is very robust and does not require an external coupling algorithm; however existing codes, without extensive changes, cannot be used. The second approach is called **partitioned** and does not require a fully integrated solver. In this approach, the equations governing the fluid flow and solid are solved independently within an iteration loop. The solution can be performed by using existing solvers (in-house or commersial ones) without any modification as ”black box” tools, after adding an external coupling tool; this is very good for use in an industrial environment where, very often, commercial tools can be used for some or all of the disciplines. As a result, in this approach, the only development needed is a stable and accurate coupling algorithm. Overall, the partitioned method is still preferable over a monolithic scheme because of its flexible/modular and appealing mathematical features. In this diploma thesis, the partitioned approach is followed, since a CFD GPU-enabled solver (the in-house CFD solver of PCOpt/NTUA) is available reducing the time needed for the fluid equations solution and this is coupled with a commercial s/w (by ANSYS) for the structural analysis.

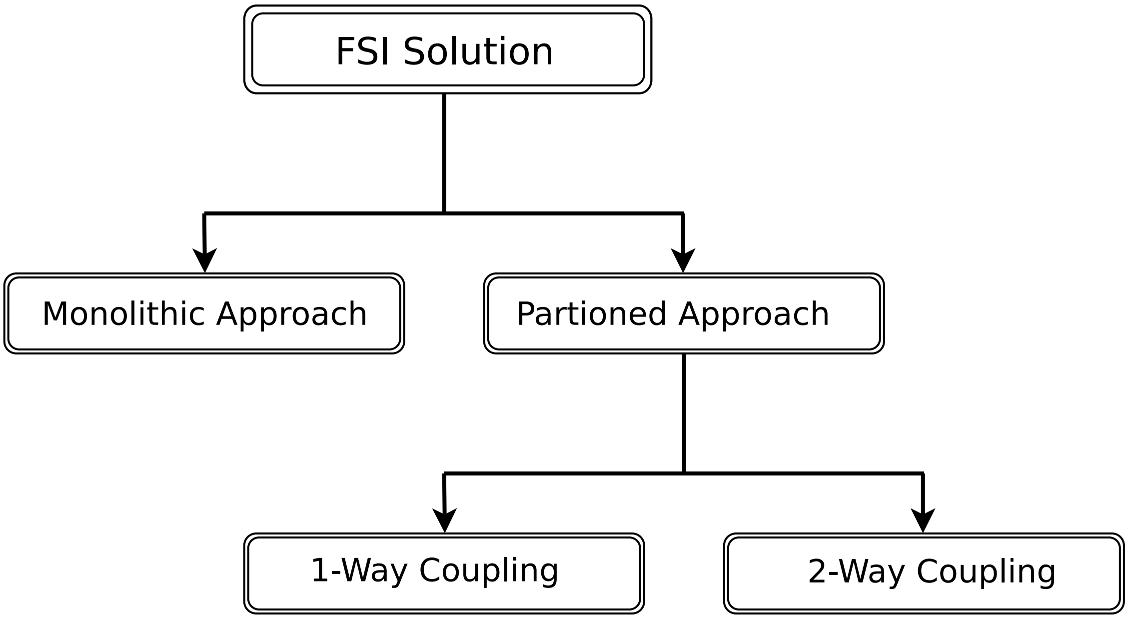

Figure 4.1: *Solving Approaches in FSI.*

4.1.1 Matching and Non-Matching Mesh Coupling

Apart from the classification according to the method used for solving the two basic principles dominating an FSI problem, the treatment of grids introduce another classification of FSI methods. From this point of view, the two possible classes of methods are the matching grid and the non-matching ones. When the computational domains of the fluid and structure problems have matching discrete interfaces, the problem of coupling is straightforward since grid nodes coincide. However, in most realistic applications, the fluid and structure grids are non-matching along the interface either because grids have been generated by different grid generation s/w or because the two problems have different resolution requirements. It is common that the fluid grids, particularly if dealing with turbulent flows, are much finer than the structure grids; this difference creates issues in relation to the conservation of energy and momentum at their interface, [23].

4.1.2 One-Way and Two-Way Coupling

The partitioned method, since the two solvers are independent, could be classified in two subclasses of methods, namely one-way or two-way coupling. In the **one-way coupling**, the communicated quantities along the FSI interface are only sent from the one domain to the other, not the other way around. For example, the fluid pressure (or the viscous stresses if a viscous flow model is considered) distribution on the structure surface is transferred from the CFD solver to the CSM solver, but the structure displacement is not transferred back. In the **two-way coupling**, the FSI interfacing data are transferred both ways. For example, the fluid pressure distribution, computed by the CFD run on the surface, is computed and transferred from the CFD solver to the CSM model. Using the pressure from the fluid as an external load, the resulting displacement of the structure is transferred back to CFD solver (displacing, thus, the boundary and, as a consequence, the boundary and internal grid) and the whole communication is performed iteratively until equilibrium is reached, [23].

4.2 Interfacing Methods

In general FSI problems, the interfacing methods between grids is certainly in important component of the computational procedure. This part of the calculation deals with the transformation of the aerodynamic loads into structural loads and of the structure displacement into the CFD grid displacement. Since the fluid and structural module can be modelled at different levels of complexity, the fidelity of the interfacing technique depends on how the fluid and structure are modelled. When solving the fluid flow with the RANS equations and the structure with CSM approaches, while the fluid grid is normally very refined close to the body in order to cover viscous effects, the structure grid is normally coarser, Fig. 4.2.

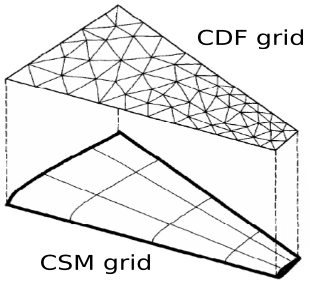

Figure 4.2: *The different grids on the surface, [24], for instance, on the surface of a wing.*

4.2.1 Aerodynamic Loads Interpolation from the CFD to the CSM Grid

After computing the aerodynamic loads on the CFD grid, they should be transferred to the CSM grid. However, in the most general case the two different grids do not match, and an algorithm should be used for this transfer. In this thesis, an algorithm based on the shape functions which are described in Chapter 3, is used for interpolating aerodynamic loads from CFD grid to the CSM grid nodes; of course, the developed algorithm could be used the other way round, should this be the case. A node-to-element approach is used, since each target node loops over all the elements of the source grid and tries to locate the element that resides in. Most nodes find a unique element and, in such a case, the interpolation is straightforward. However, occasionally, due to the curved (in 3D) shape of the surface there are ambiguities and the node seems to belong to two or more elements. The element that minimizes the distance is then selected. The method is presented for interpolating pressures from the CFD elements to the CSM nodes, however the same steps can be followed for the interpolation of deformations from the CSM grid to the CFD nodes. In the flowchart that follows, it doesn't matter the type of elements of the target (CSM) surface grid (practically, only "target nodes" matter). The source (CFD) surface grid is formed by triangles and/or quadrilaterals. In case of quadrilaterals, though, these are split into triangles, see below. In order to find in which element each node resides in the following steps are utilized:

1. As already said, all quadrillaterals of the source CFD surface grid are split into triangles.
2. For each target CSM node, loop over all the CFD triangles is performed and the following calculations are performed:

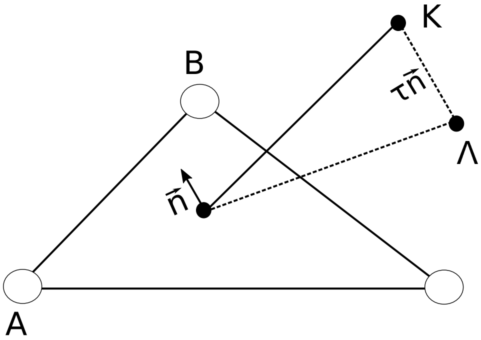

Figure 4.3: *CFD element triangle (ABΓ) and CSM node K, for which should be decided if K resides in.*

$$\vec{r}_M = \frac{\vec{r}_A + \vec{r}_B + \vec{r}_\Gamma}{3}, \tag{4.1}$$

(this is the position vector of the barycenter of triangle $AB\Gamma$)

$$\vec{n} = \frac{\overrightarrow{AB} \times \overrightarrow{A\Gamma}}{|\overrightarrow{AB} \times \overrightarrow{A\Gamma}|} \tag{4.2}$$

(this is the unit normal vector to the triangle). In order to define if the normal vector is inwards or outwards, a check for the

$$\tau = \overrightarrow{MK} \cdot \vec{n} \tag{4.3}$$

(this is the projection of the vector linking points to M and K onto the normal vector to the triangle). In order to define if the normal vector is pointing inwards or outwards, a check for the sign of τ is performed. If the sign is positive, then the node is projected onto the triangle, else the projected node belongs to the opposite side of our geometry.

$$\vec{r}_{\Lambda} = \vec{r}_M + \overrightarrow{MK} - \tau\vec{n} \tag{4.4}$$

(this is the position vector of point Λ which is the projection of K onto the surface). If K resides in $AB\Gamma$ then the following equation

$$|\overrightarrow{\Lambda A} \times \overrightarrow{\Lambda B}| + |\overrightarrow{\Lambda B} \times \overrightarrow{\Lambda\Gamma}| + |\overrightarrow{\Lambda\Gamma} \times \overrightarrow{\Lambda A}| = |\overrightarrow{AB} \times \overrightarrow{A\Gamma}| \tag{4.5}$$

related to the sum of the areas of the three triangles formed by the triangle vertices and the projection point Λ must be satisfied. After finding in which source triangles the target node K resides in, (in a complex shaped surface there might be more than one triangles for each point), the one which minimizes the absolute τ value is kept. After having found the grid triangle in which the point belongs to, it is straightforward to identify the "parent" quadrilateral of this triangle.

3. The parametric coordinates (s,t) of the projected CSM point onto the CFD surface grid are computed through the following formulas:

$$\begin{aligned} x_K &= \sum_{i=1}^{3or4} N_i(s,t)x_{f_i} \\ y_K &= \sum_{i=1}^{3or4} N_i(s,t)y_{f_i} \\ z_K &= \sum_{i=1}^{3or4} N_i(s,t)z_{f_i} \end{aligned} \tag{4.6}$$

where x_f, y_f, z_f are the coordinates of the triangles/quadrilaterals' vertices. Eq. 4.6 is solved iteratively with the Newton-Raphson method. However, the above system has three given equations and two unknown variables, the parametric coordinates (s,t). As a result only two equations could be used for the solution. In order to determine which two, the computed unit normal vector is used. Specifically, the absolute values of the three coordinates of the normal vector n_x, n_y, n_z are computed and the maximum one is found. Each n_x, n_y, n_z corresponds to one equation. The equation that corresponds to the component with the absolute maximum value is eliminated.

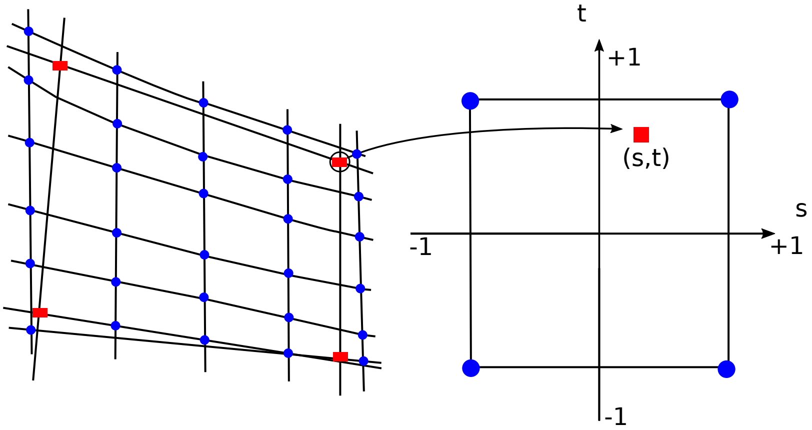

Figure 4.4: *Left: Difference between the two grids, CFD nodes (blue) represented as a structured grid in this figure, (though this is not necessary at all), CSM nodes (red). Right: The node to element approach used to interpolate the aerodynamic load to the CSM grid, [25].*

4. Interpolate the aerodynamic load by using the computed (s,t) for each CSM node.

$$p_K = \sum_{i=1}^{3or4} N_i(s_K, t_K) p_{f_i} \tag{4.7}$$

4.2.2 Validation Cases For the Shape Function Based Interpolation Algorithm

After presenting the basic algorithm developed for interpolating fields between non-matching grids a series of demonstration/validation cases are presented in this section. The first case is a simple surface given with a closed form expression by the following equations:

$$x = ucos\phi \\ y = usin\phi \\ z = \phi \tag{4.8}$$

where $0 < u < 1$ and $\frac{\pi}{4} < \phi < \frac{\pi}{2}$. On the above surface, two grids with different number of nodes are created. The one contains 10201 and the other 2601 nodes. Both grids are unstructured, containing only triangles. The fine grid represents the CFD grid and the coarse one the CSM one. A scalar quantity (a field) is assigned to the nodes of the fine grid, representing the pressure field computed from the CFD solver in the aeroelastic problem. An analytic integration is performed, in order to have a baseline to compare with. Then the coordinates of the two grid points along with the assigned values of the fine grid are used by the interpolation algorithm. The assigned values to the coarse grid points are extracted, integrated and a comparison with the results from the analytic integration is performed. Also, the ANSYS interpolation algorithm and an in-house RBF interpolation tool are used for comparison, Table 4.1. The shape function based algorithm produces similar results to the RBF tool and ANSYS. Also, in Fig. 4.6, the scalar field on the initial grid and on the interpolated one can be seen.

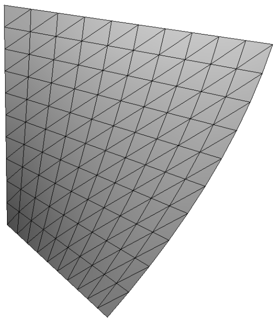

Figure 4.5: *3D Surface used for the interpolation.*

Integration Point	Value	Percentage Difference
Source grid	-0.32297	-
ANSYS interpolated values	-0.33385	3.2364%
RBF interpolated values	-0.33359	3.3134%
Shape function based algorithm	-0.33358	3.3134%

Table 4.1: *Integrated value of the scalar value on the source or target surface grids; for the latter,the integration is performed and after the interpolation.*

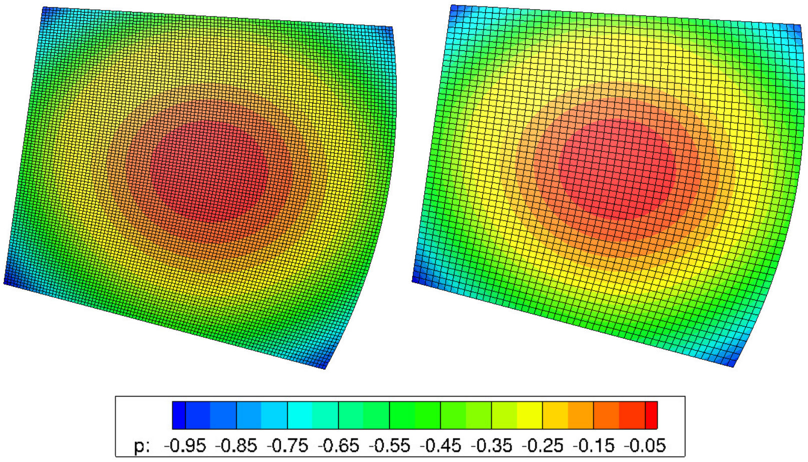

Figure 4.6: *3D Surface "pressure" (the scalar field to be interpolated will briefly denoted by "pressure", into quotation marks) field used for the interpolation. Left: Source (fine) grid and "pressure" field. Right: Target (coarse) grid and the interpolated "pressure" field.*

The second test case refers to the aeroelastic problem analysed in this thesis. The two non-matching grids used are the surface CFD grid containing 11277 nodes and the CSM surface grid containing 6443 nodes, Fig. 4.7. The scalar field to be interpolated is the pressure field computed by the CFD solver. Iso-areas for the initial (source) pressure field and the interpolated one contour are essentially the same, Fig. 4.8. So far, the shape function algorithm was used for interpolating values from a fine grid to a coarse grid. Next step is to use the same algorithm for the opposite course, from a coarse to a fine grid. The non-matching grids used are the same as before, however in this case, deformations computed on the CSM grid should be interpolated onto the CFD surface grid. In this test case, bending along y-axis is performed in the CSM model. The CFD surface grid is deformed accordingly, Fig. 4.9.

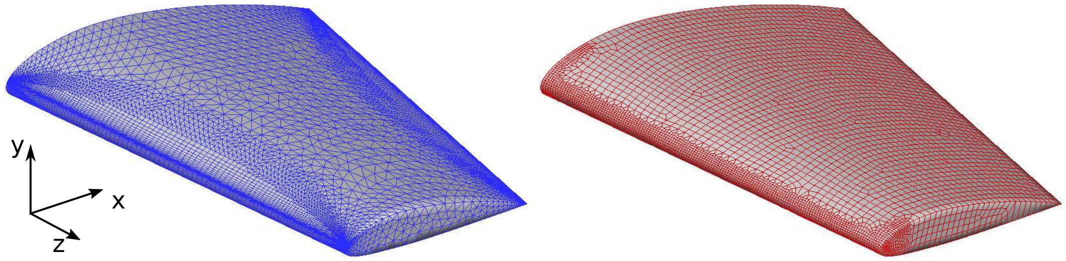

Figure 4.7: *Surface grids for the two solvers. Left: The source CFD surface grid (blue). Right: The target CSM grid (red).*

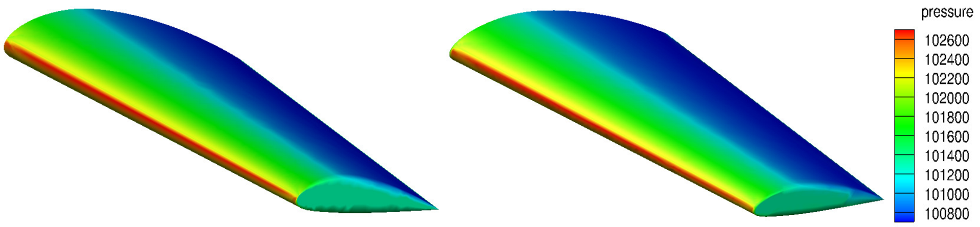

Figure 4.8: *Pressure fields on the two grids. Left: The initial pressure field computed from the CFD solver on the CFD surface grid. Right: The interpolated pressure field on the CSM grid.*

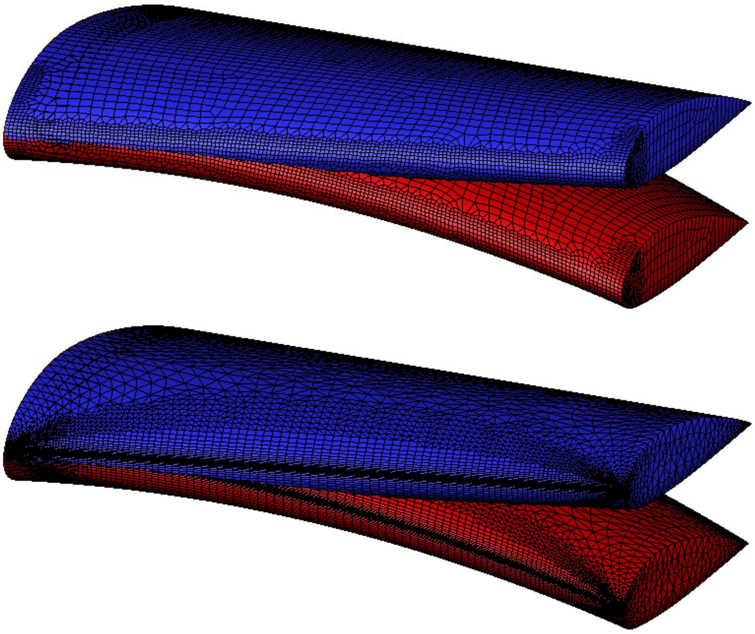

Figure 4.9: *Deformation interpolation from CSM to CFD grid. Top: Initial (blue) CSM grid and deformed CSM grid (red) as computed by ANSYS. Bottom: Initial (blue) CDF grid and the interpolated one (red).*

The final test case refers to the CRM wing (NASA Common Research Model [26]). The source grid is the wing surface grid extracted from an available CFD volume grid (having about 3 million nodes), containing 45177 nodes. As target a surface grid extracted from another much finer available CFD volume grid (having about 28 million nodes) is used; the grid surface has 180465 nodes. Both surface grids are structured and composed only of quadrilateral elements. The value to be interpolated is the deformation along x, z axes resulting in a rotation of the whole wing along the y axis, Fig. 4.10.

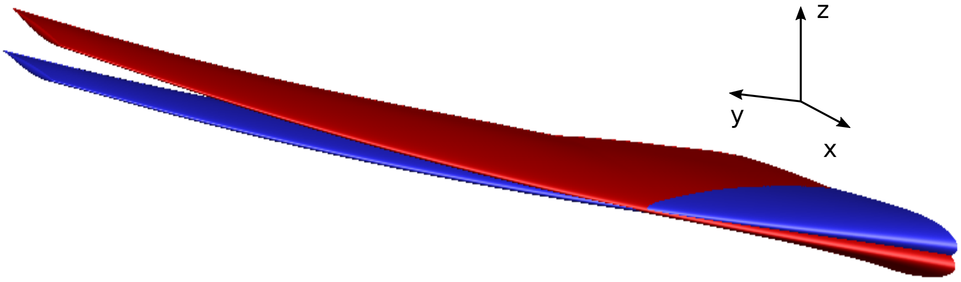

Figure 4.10: *Deformation interpolation from a coarse to a fine grid. Initial (blue) wing and the interpolated deformed wing (red).*

4.2.3 Deforming the Volume CFD Grid

In order to perform an automated FSI-analysis, except from the fluid and structure solver, a procedure to adapt and regenerate the volume CFD grid for each aeroelastic cycle is needed. In this thesis, an in-house RBF-based (Radial Basis Function) grid displacement tool was used, [27]. The basic theory of the RBF networks is summarized below.

An RBF network is a weighted linear combination of RBF kernels, which can interpolate discrete data in the n-dimensional space. In FSI, the quantity to be interpolated are the known 3D displacements at the S surface CFD grid, which are interpolated by the shape function algorithm. A 3D RBF kernel $\phi_S(x) = \phi(r\|x - x_s\|)$ is a real value function depending on the distance r of a point $x \ \epsilon \ \Re^3$, which belongs to the CFD-grid from the RBF interpolation source $x_s \ \epsilon \ \Re^3$. ($\|.\|$ stands for the Euclidean distance). To interpolate three displacement fields (in the 3D space), the RBF interpolation will separately be applied to each one of them.

The RBF deformation function $d : \Re^3 \rightarrow \Re^3$ is a linear combination of the kernels ϕ_s, centred at the N source nodes and weighted by $w_s \ \epsilon \ \Re^3$:

$$d(x) = \sum_{S=1}^{N} w_s \phi_s(x) \tag{4.9}$$

where, x is the target position vector, in FSI case the CFD volume grid, with $x_M,\ M \epsilon\, [1, ..., M]$ and $x_s,\ S \epsilon\, [1, ..., N]$ the source nodes, in FSI case the deformed surface CFD grid.

The weights w_s are computed so as to exactly reproduce the imposed displacements δ_s at the source nodes. This requires the solution of a NxN linear system:

$$\begin{bmatrix} \phi_1(x_1) & \dots & \phi_N(x_1) \\ \vdots & \ddots & \vdots \\ \phi_1(x_N) & \dots & \phi_N(x_N) \end{bmatrix} \begin{pmatrix} w_1^T \\ \vdots \\ w_N^T \end{pmatrix} = \begin{pmatrix} \delta_1^T \\ \vdots \\ \delta_N^T \end{pmatrix} \tag{4.10}$$

After solving equation 4.10 the displacements for all the target nodes are computed according equation 4.9. It is obvious that the computation of the weights is the most expensive task, since the size of the source grid affects the computational cost. The in-house RBF tool contains several techniques for reducing the computational cost which are developed in the framework of an ongoing PhD thesis in PCOpt/NTUA,[27].

Chapter 5

Workflow Used for the Aeroelastic Problem

In this chapter, the workflow followed in this study will be covered. The PUMA CFD code running on GPUs described in Chapter 2 is used to predict the flow field around the geometry. The MAPDL commercial CSM code described in Chapter 3 is used to compute the resulting displacements of our structure. The new interpolation tool based on shape functions and the in-house RBF tool described in Chapter 4 are used for the interpolation of the computed structural displacements and aerodynamic loads between the two different grids and the grid morphing of the CFD volume grid respectively.

5.1 Steps Within the Zeroth Cycle

The first step for the aeroelastic problem is the creation of the basic geometry. Two geometries are used for this thesis a NACA4318 airfoil-shaped wing and a NACA0012 one, both of them are designed in a commercial CAD s/w and exported as an Initial Graphics Exchange Specification (IGES) format, Appendix A. Next step for the aeroelastic problem is the creation of the CFD grid, which is performed using the commercial s/w Pointwise and exported in a format compatible with the PUMA code, Appendix B. Then, the CFD solver input file, containing the farfield boundary condition is written. An assumption made in this diploma thesis is that, despite having an inflatable wing the baseline geometry is assumed to be undeformed, then in the 'zeroth' cycle the inflation procedure is modelled, by applying a uniform pressure of 101325 Pa, on the skin of the wing. The CSM workflow for the 'zeroth' cycle is described below. A sample of the batch commands used for the CSM model can be found in Appendix C.

- The IGES file of the geometry is imported into the pre-processor of the CSM s/w.
- The elements for the CSM grid, the material properties and the thickness of the structure are defined.
- A unstructured grid with 4-node elements is created using the integrated meshing tool offered by ANSYS.
- Symmetry plane and supports are defined.
- An internal pressure applied to all the elements is simulating the inflation pressure exerted by the pressurized gas.
- The uniform pressure of 101325 Pa is applied to the CSM grid nodes.
- The solution of the structural problem is performed.
- The deformation of each CSM node is written in the global coordinate system as (dx, dy, dz). This then will be used for the CFD grid deformation by the RBF-morpher tool.
- The stresses computed and the deformed state of the geometry is saved for the first aeroelastic cycle, Appendix D

Finally, the file containing the computed deformations is used by the RBF-morphing tool in order to deform the CFD grid accordingly.

5.2 Steps Within All Subsequent Cycles

Some from the above steps are used only for the 'zeroth' aeroelastic cycle. Specifically, after deforming the initial CFD grid, according to the CSM computed deformations, the procedure used is described below and can be seen at Fig. 5.1

- The deformed CFD grid from the previous cycle is used as data to the PUMA solver in order to compute the flow field around the geometry. After, the specified number of the CFD solver iterations is reached, a file containing the coordinates of the surface CFD grid and the computed pressure is written.
- The CSM solver setup is different compared to the 'zeroth' cycle:
    - The deformed geometry, saved in a grid format, from the last cycle is used as the initial one for the next cycle. As a result, there is no need

  to remesh/rebuild the CSM model and define elements, materials and thickness.

  - The computed stresses from the previous cycle are applied to the new model, as an initial state to the geometry.
  - Since, the same model is used from the previous cycle there is no need for defining again supports and symmetry plane. Also, the internal pressure resembling the pressurized gas is kept constant throughout the cycles.
  - The pressure distribution computed by the CFD solver on the deformed CFD grid nodes is interpolated onto the CSM grid nodes.
  - The solution of the structural problem is performed.
  - The computed deformation of each CSM node is written in a file and this is used for the CFD grid deformation by the RBF-morpher tool.
  - The stresses computed and the deformed state of the geometry is saved for the next aeroelastic cycle.

- Then the maximum deformation computed by the CSM solver and the lift force computed by the CFD solver are checked in order to ascertain if aeroelastic convergence is reached. In case that the current solution is deemed unconverged the RBF-morphing tool is used in order to deform the CFD grid and the same procedure is performed again until convergence is achieved.

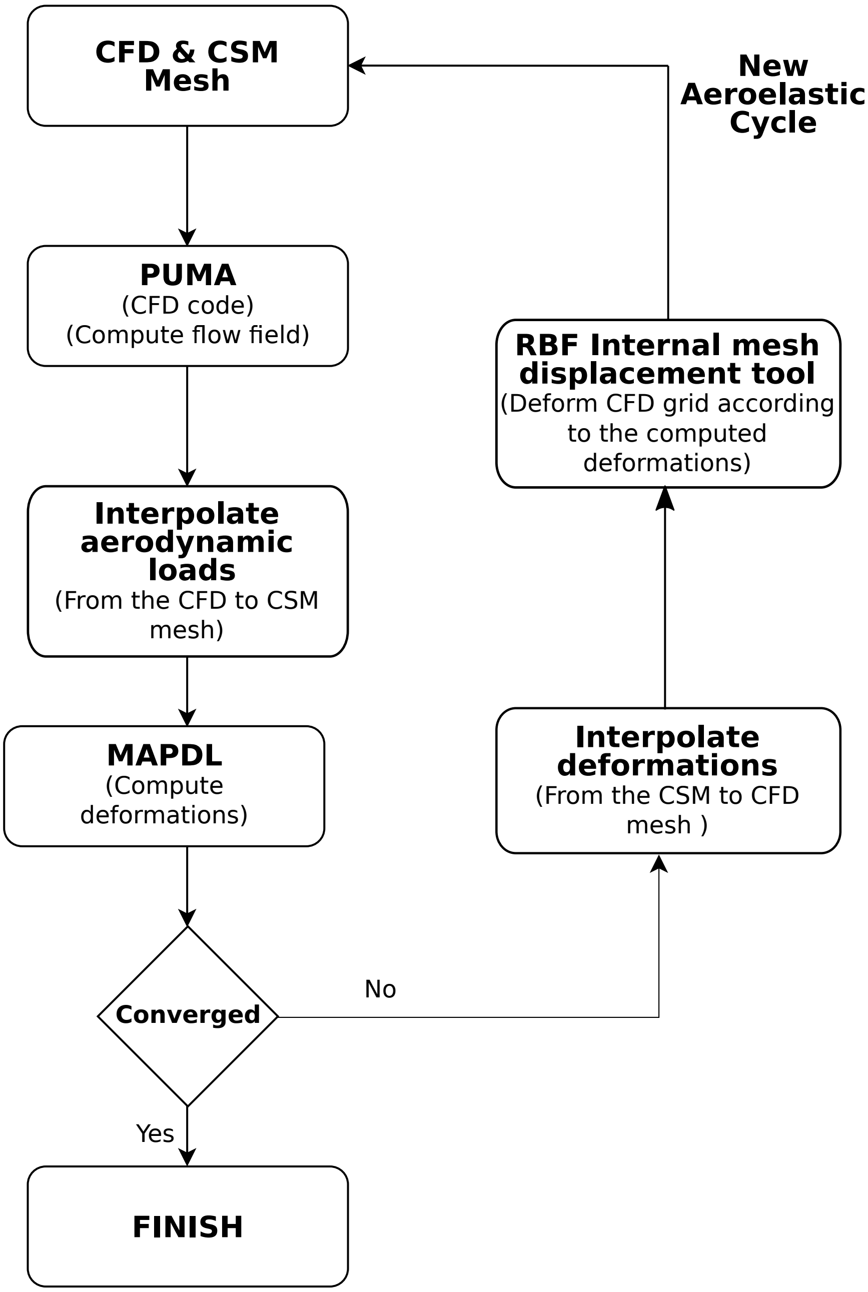

Figure 5.1: *Aeroelastic analysis workflow.*

Chapter 6

Aerostructural Analysis of Inflatable Wings

6.1 Cases Overview and Common Characteristics

All the examined cases are tabulated in Table 6.1. A caterpillar-shaped wing can be seen in Fig. 6.18 and in this thesis the term is used for the wing created from the approximation of an airfoil with circular profiles. Flow conditions used for all cases are presented in Table 6.2. The basic two material properties, used for all cases, Tables 6.3 and 6.4. At first, a composite material modelled as an orthotropic one is used, Table 6.3. The second material used is modelled as an isotropic one, Table 6.4. The second one in comparison to the composite is more flexible and is used to analyse the behaviour of the inflatable wing in such case.

Fluid Eqs.	*Material Used*
Case 1: NACA4318 wing without tethers	
Euler	Composite/Stiff
RANS	Composite/Stiff
RANS	Elastic/Flexible
Case 2: Caterpillar-shaped NACA4318 wing without tethers	
RANS	Composite/Stiff
RANS	Elastic/Flexible
Case 3: NACA4318 wing with tethers	
RANS	Composite/Stiff
Case 4: NACA0012 wing without tethers	
Euler	Composite/Stiff
RANS	Composite/Stiff
RANS	Elastic/Flexible
Case 5: NACA0012 wing with tethers	
RANS	Composite/Stiff

Table 6.1: *Overview of the cases studied in this chapter.*

FarField Condition	**Value**
Air Density	1.2 kg/m^3
Static Pressure	101325 Pa
Velocity Magnitude	60 m/s
Flow Direction	X-axis
Infinite Pitch Angle	10 degrees
Yaw Angle	0 degrees
Temperature	294 K
Air Dynamic Viscosity(RANS only)	$1.716 \times 10^{-5} kg/ms$
Turbulence Model(RANS only)	Spalart-Allmaras

Table 6.2: *All cases: Data used the CFD solver.*

Orthotropic Composite Material Properties	
Density	$1000.7 kg/m^3$
Young' Modulus XY	$9.3769 \times 10^9 kg/ms^2$
Young' Modulus YZ	$8.411 \times 10^9 kg/ms^2$
Young' Modulus XZ	$8.411 \times 10^9 kg/ms^2$
Poisson's Ratio	0.36
Shear Modulus XY	$1.972 \times 10^8 Pa$
Shear Modulus YZ	$1.489 \times 10^8 Pa$
Shear Modulus XZ	$1.489 \times 10^8 Pa$

Table 6.3: *All cases: Composite material properties.*

Isotropic Elastic Material Properties	
Density	$1400.6 kg/m^3$
Young' Modulus	$2 \times 10^8 kg/ms^2$
Poisson's Ratio	0.33

Table 6.4: *All cases: Elastic material properties*

6.2 Case 1: Studies on the Inflatable NACA4318 Wing

6.2.1 Aeroelastic Computations based on the Euler Equations

The first case is concerned with the aeroelastic problem of a NACA4318 shaped wing. The initial geometry is designed using the standard NACA4318 profile to create a tapered wing. The model consists of an internal configuration which accommodates the pressurized gas. It was chosen to separate the wing into 7 air-tight compartments with 6 transverse ribs, Fig. 6.1. The CFD grid is generated using Pointwise and since an inviscid flow model is used, the distance of the first nodes off the wall is chosen to be 0.001 m. The farfield boundary is a sphere with a radius equal to 50 metres, when the half wing span is 1m. A hybrid grid with $\sim 3 \times 10^5$ nodes, consisting of tetrahedra, pyramids, prisms and hexahedra is generated around half of the wing. The CFD grid is shown in Fig. 6.2. The aeroelastic computation will be based on the in-house PUMA code for the CFD analysis, Chapter 2, the MAPDL for the structural analysis, Chapter 3 whereas for interfacing the above deformations are interpolated to the CFD grid using the RBF-house tool, Section 4.2.3, whereas pressures are interpolated to the CSM grid from the CFD grid using

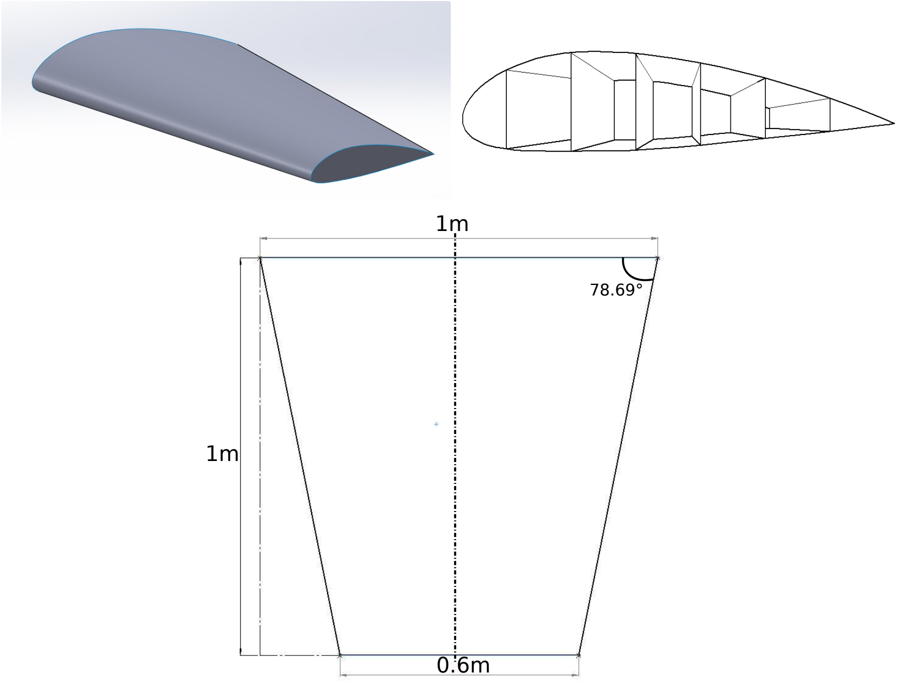

Figure 6.1: *Case 1. NACA4318 airfoil shaped wing. Top-Left: Half of the 3D wing model. Top-Right: Perspective view of the internal ribs. Bottom: Half-wing planform.*

ANSYS integrated tool, Section 4.2.1. The necessary supporting tethers, Fig. 1.11,

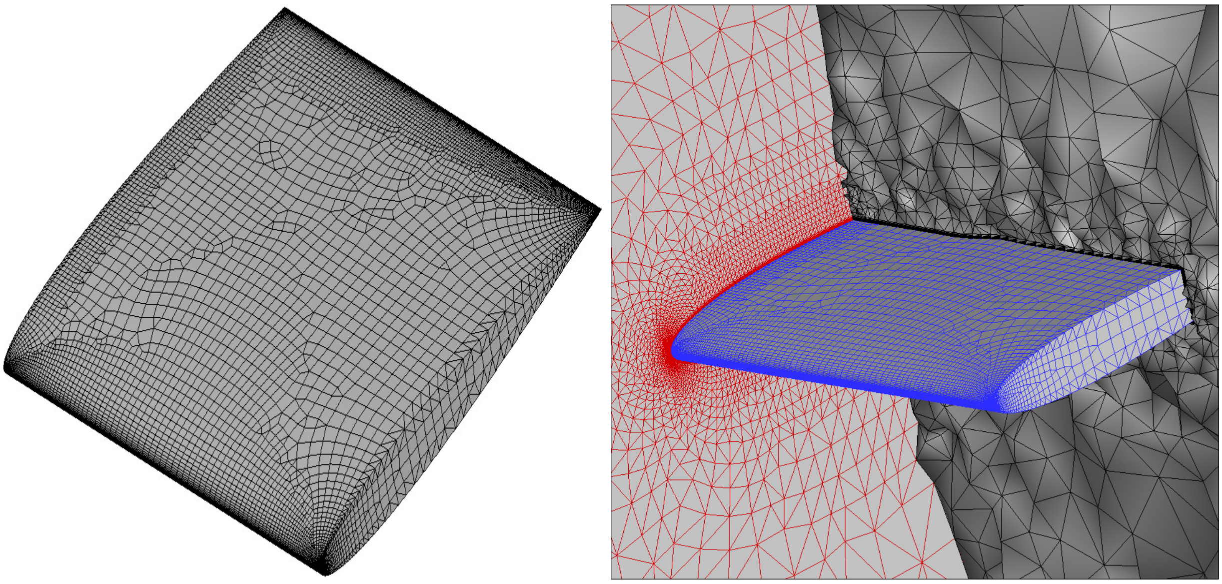

Figure 6.2: *Case 1. CFD grid used for the numerical solution of the Euler equations. Left: Hybrid surface grid, with triangles and tetrahedra, on the wing surface. Right: Hybrid volume grid around half of the wing. The wing surface is shown in blue and the symmetry boundary in red.*

for cases 1,2 and 4 have not been included as separate bodies; instead they have been replaced by a pair of supports pre wing tip, Fig. 6.3. The front tether is substituted by a support constraining translations along the x, y axes and the rear tether by a support constraining translation along the y axis only. The CSM solver basic data are given in Table 6.5. Monitoring the lift coefficient evolution during aeroelastic cycles and the maximum deformation deviation from the previous cycle, Fig 6.4, shows that the aeroelastic problem is practically well converged after 8 aeroelastic cycles. In the last aeroelastic cycle the deviation of the maximum deformation from the previous cycle is equal to $2.13 \times 10^{-5} m$. Fig. 6.4 presents the evolution of the maximum deformation on the wing surface in terms of aeroelastic cycles

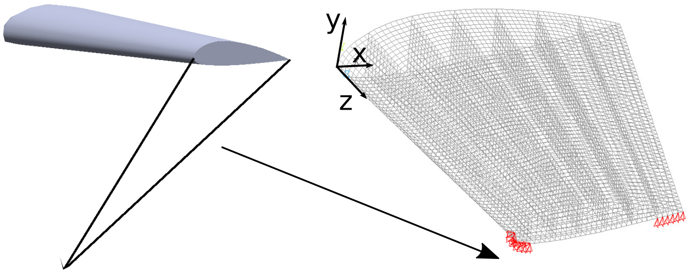

Figure 6.3: *Case 1. 3D model of the wing with tethers. Instead of using tethers, supports (see in the text) are used at the wing tip.*

Material	Composite Material
Elements	Shell 181
Thickness	1 mm
Internal Pressure	120000 Pa

Table 6.5: *Case 1. CSM solver basic data for NACA4318 shaped wing.*

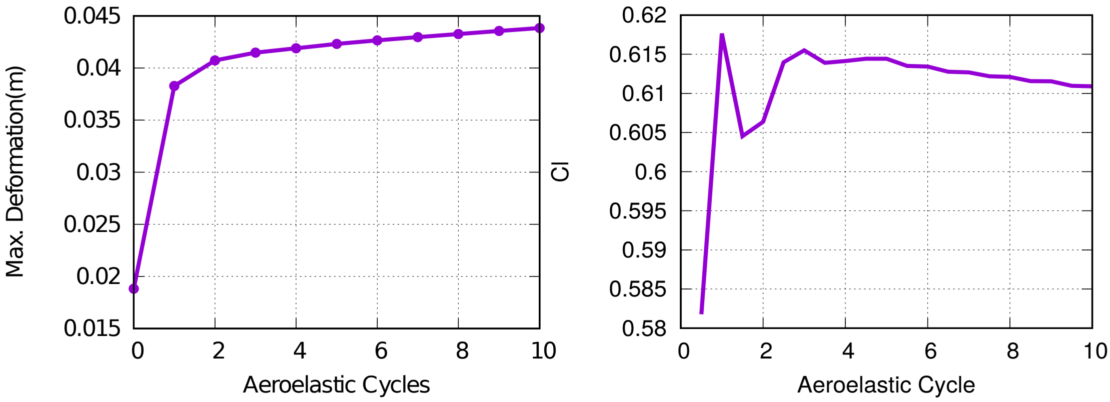

Figure 6.4: *Case 1. Evolution of aeroelastic simulation, inviscid flow. Left: Cumulative maximum deformation in each aeroelastic cycle. Right: Lift coefficient evolution during the aeroelastic cycles.*

and shows that, within 10 cycles at most, the aeroelastic loop is considered to be adequately converged for engineering purposes. In the same plot, a superposition of the evolution of the lift coefficient during the aeroelastic cycles, as an extra proof of the overall algorithm convergence, is also shown.

In Fig. 6.5, the convergence of all the flow equations in the last aeroelastic cycle is presented; this is a good demonstration that the fact that a convergence criterion is not activated and, instead, the flow equations are solved for 2000 iterations per aeroelastic cycle, is absolutely sufficient and leads to adequately converged results. Each flow solution (for the fixed amount of 2000 iterations) takes ∼ 10 min on a single NVIDIA Tesla K40 GPU, the structural solution takes ∼ 2 min. on Intel I-5 CPU and the CFD grid deformation ∼ 3 min. on the same CPU. Recall that the CFD grid deformation, which adapts the CFD grid to the displaced wing (as a result of a structural analysis within an aeroelastic cycle) is based on the in-house RBF tool (Section 4.2.3). As a result the whole aeroelastic problem using Euler equations for 10 aeroelastic cycles costs around 2.5 hours on an heterogeneous computational platform. At the zeroth aeroelastic cycle, the wing is inflated and it takes a more rounded shape. In the next aeroelastic cycles, the wing is deformed upwards due to the aerodynamic (pressure) losses, Fig. 6.6. The Mach number field, plotted on the symmetry plane, for the initial and the deformed wing is compared in Fig. 6.7.

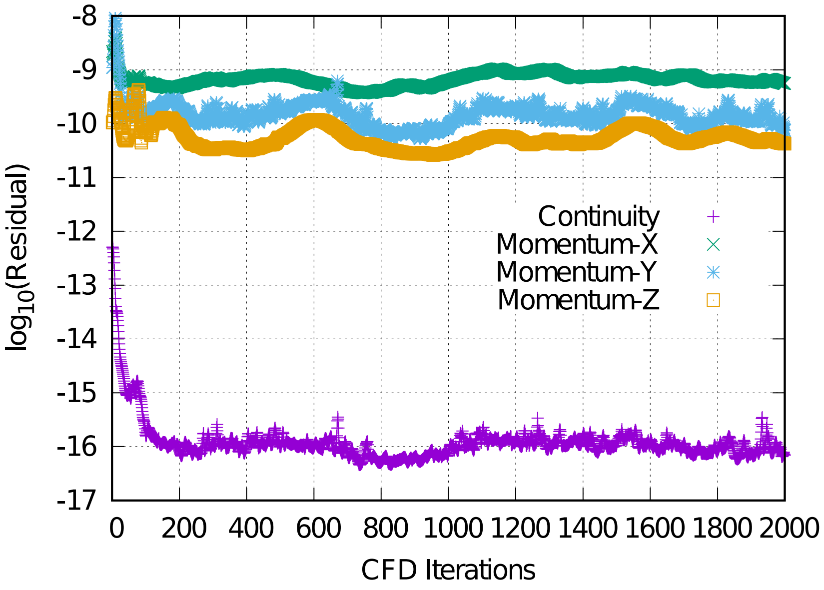

Figure 6.5: *Case 1. CFD convergence for the last aeroelastic cycle NACA4318, inviscid flow. Each CFD tun terminates after 2000 iterations, in each cycle, without any other convergence criterion.*

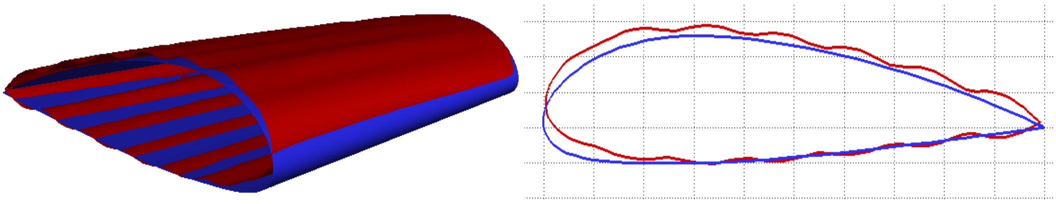

Figure 6.6: *Case 1. Total deformation of the wing at the end of aeroelastic cycles, inviscid flow. Left: Initial (blue) and the finally deformed (red) wings in 3D space. Right: View of the airfoil on the symmetry plane of the initial (blue) and deformed (red) wing.*

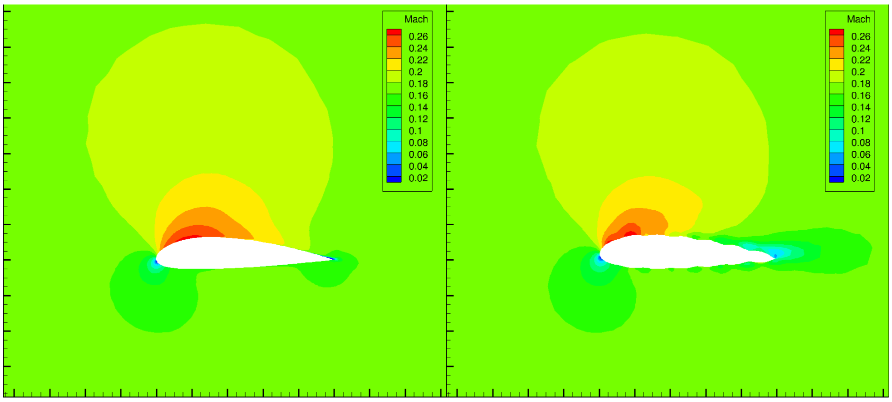

Figure 6.7: *Case 1. Mach number iso-areas around the wing on the symmetry plane, inviscid flow. Left: Initial state. Right: Deformed wing, upon convergence of the aeroelastic simulation.*

6.2.2 Aeroelastic Computations based on the RANS Equations

After solving the aeroelastic problem by making the assumption of inviscid flow, the next step is to use the Navier-Stokes equations instead, because, after the inflation, the surface skin of the wing is bumpy and separation could occur. Working with the RANS equations, the only changes made are related to the CFD grid and CFD solver setup. A hybrid grid of tetrahedra, pyramids, prisms and hexahedra consisting of $\sim 1 \times 10^6$ nodes is generated around half of the wing. The average distance of the first series of nodes off the wall is chosen to allow for resolution of the turbulent boundary layer down to the wall ($y+ < 1$). The CFD grid is shown in Fig. 6.8.

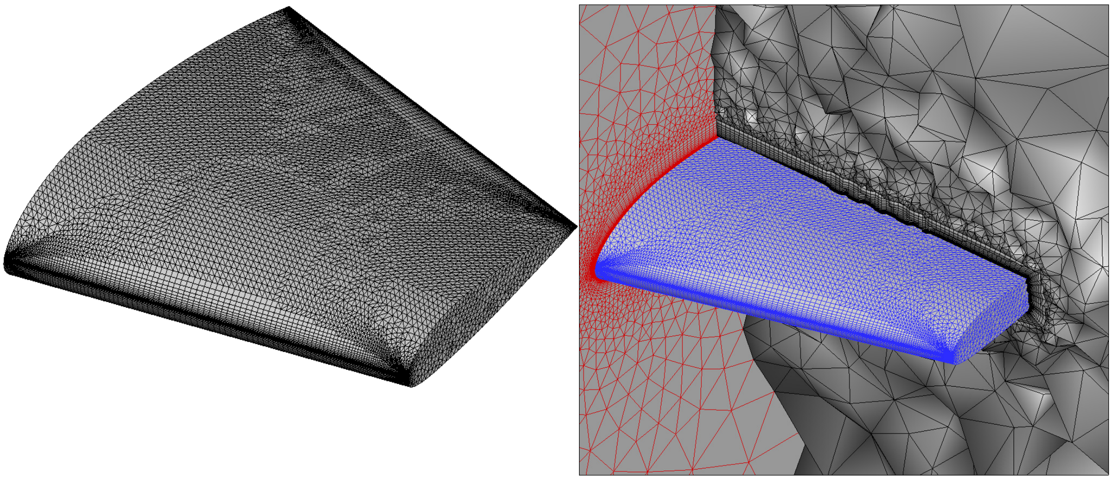

Figure 6.8: *Case 1. CFD grid for a viscous/turbulent flow simulation. Left: Hybrid surface grid on the wing surface. Stretched quadrilateral elements are used close to the LE and tip regions, to properly capture the surface curvature at these areas. Right: Hybrid volume grid around the wing. The wing surface is shown in blue and the symmetry boundary in red. Stretched hexahedra and prisms are used close to the wing surface to obtain proper boundary layer resolution.*

As before the aeroelastic problem is practically well converged after 8 cycles, yielding maximum deformation deviation is equal to the value of $2.12 \times 10^{-5} m.$, Fig. 6.9. The lift coefficient has not converge in depth, however the aeroelastic cycles are stopped, since the problem has reached a satisfactory level of convergence, Fig. 6.9.

In Fig. 6.10, the convergence of the CFD equations for the last 2000 iterations of the last aeroelastic cycle is shown. Each flow solution takes $\sim$ 25 min. on a single NVIDIA Tesla K40 GPU, the structural solution takes $\sim$ 2 min. on an Intel I-5 CPU and the CFD grid deformation $\sim$ 3 min. on the same CPU. Overall, the whole aeroelastic problem using Navier-Stokes equations for 10 aeroelastic cycles

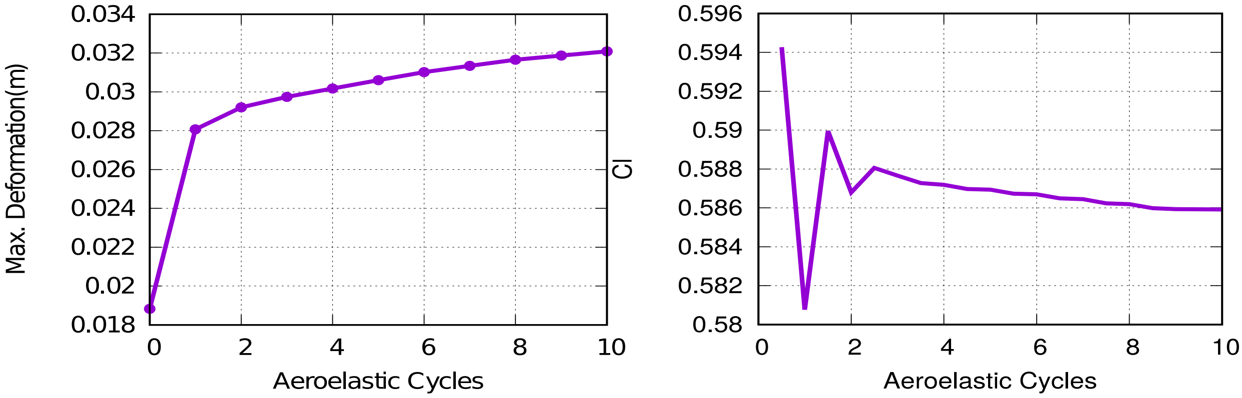

Figure 6.9: *Case 1. Evolution of the aeroelastic simulation NACA4318, viscous flow. Left: Cumulative maximum deformation calculated in each aeroelastic cycle. Right: Lift coefficient evolution during 10 aeroelastic cycles.*

costs around 5 hours, having twice as much as the cost of a similar simulation using the inviscid flow model.

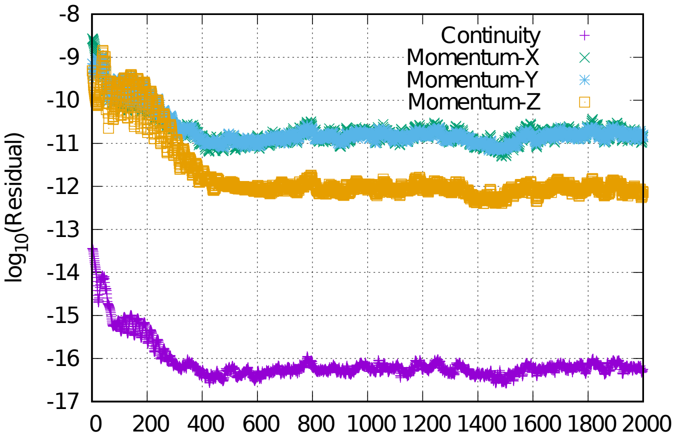

Figure 6.10: *Case 1. CFD equations convergence for the last aeroelastic cycle, viscous flow.*

By comparing the convergence of the CSM model between the aeroelastic problems solved with the Euler and Navier-Stokes equations, Fig. 6.11, it is seen that, in the first cycle, the Euler equations produce a higher aerodynamic load resulting in a higher deformation compared to the Navier-Stokes equations, the solution of which is affected by the bumpy shape of the inflated wing and results in a reduced aerodynamic load. This reduction takes place due to the fact with the turbulent flow model, the CFD solution captures the separation, which occurs at the trailing edge of the wing, Fig. 6.12.

After running the inflated wing with a pitch angle of 10° the same aeroelastic solution was performed for three different pitch angles 2° 5° and 8° and the computed values of the lift and drag coefficient are used to draw the polars, Fig. 6.13. Also, the

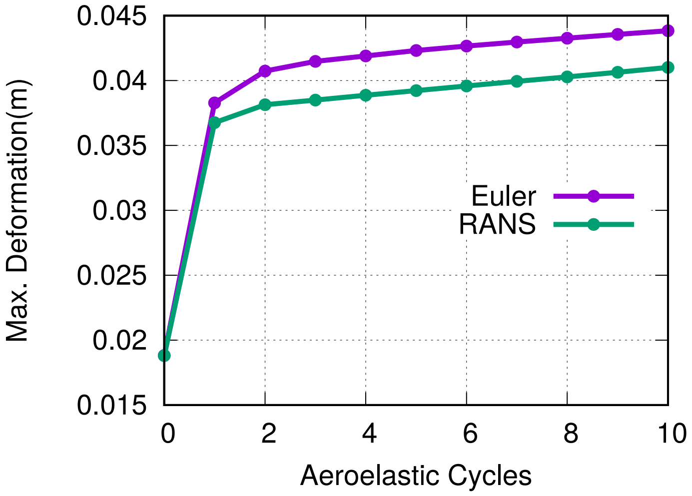

Figure 6.11: *Case 1. Cumulative maximum deformation of the wing. Comparison between the solutions of the Euler and the Navier-Stokes equations.*

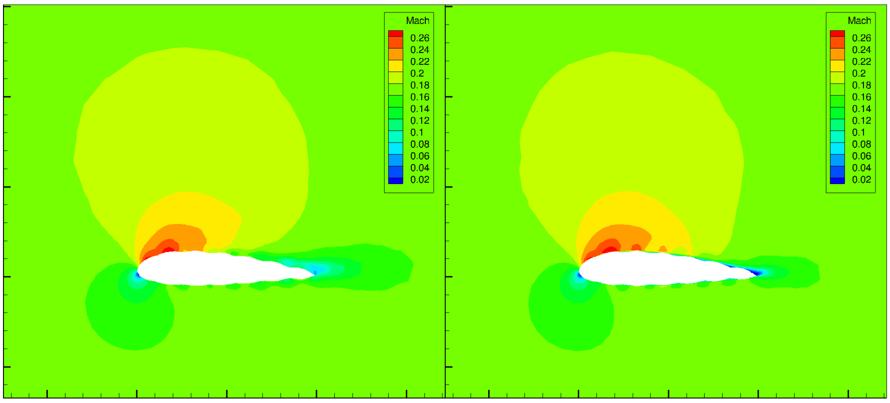

Figure 6.12: *Case 1. Mach number iso-areas over the symmetry plane at the last aeroelastic cycle. Left: Field computed by solving the Euler equations. Right: Field computed by solving the RANS equations.*

undeformed NACA4318 wing polar is produced by running a CFD analysis with the same range of pitch angles for comparison.

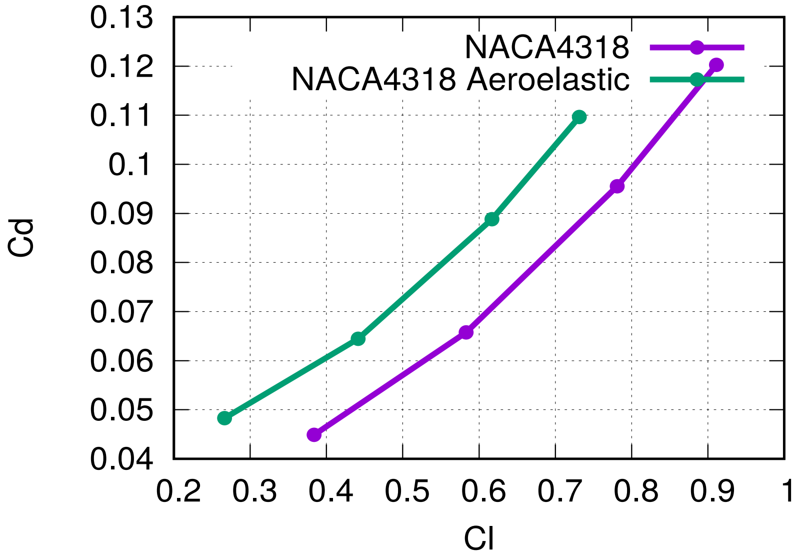

Figure 6.13: *Case 1. The computed polar (c_L vs. c_D) using the RANS equations' model. Undeformed NACA4318 wing (purple) and deformed NACA4318 wing from the aeroelastic problem. The shape of the curve produced by the used angle of attacks is similar to a regular polar diagram of a NACA 4318 wing, despite the change in the shape of the wing due to the structural deformations.*

6.2.3 Case 1. Revisited using a Flexible Material

The scale of the deformations produced by using a composite material for the aeroelastic problem was small and as a result the next step was to change the material in a more flexible material in order to evaluate the behaviour of the wing in such a case. The only change that has to be made is in the CSM model, by changing the material properties, the thickness and the internal pressure, Table 6.6. After changing the material properties, the aeroelastic problem is solved again.

Material	Orthotropic Material, see table 6.4
Elements	Shell 181
Thickness	3 mm
Internal Pressure	110000 Pa

Table 6.6: *Case 1. CSM solver for flexible material.*

In this case the computed maximum deformation is higher. The new problem is converged, Fig. 6.14, to the value of $5.79 \times 10^{-6} m$. for the deviation of the maximum deformation computed by the CSM solver and the lift coefficient evolution is practically converged.

It is interesting to pay attention to the difference in the first aeroelastic cycle between the two cases, Fig. 6.15. In both cases, the same CFD setup options and CFD grids are used, however, differences in the thickness, material and internal

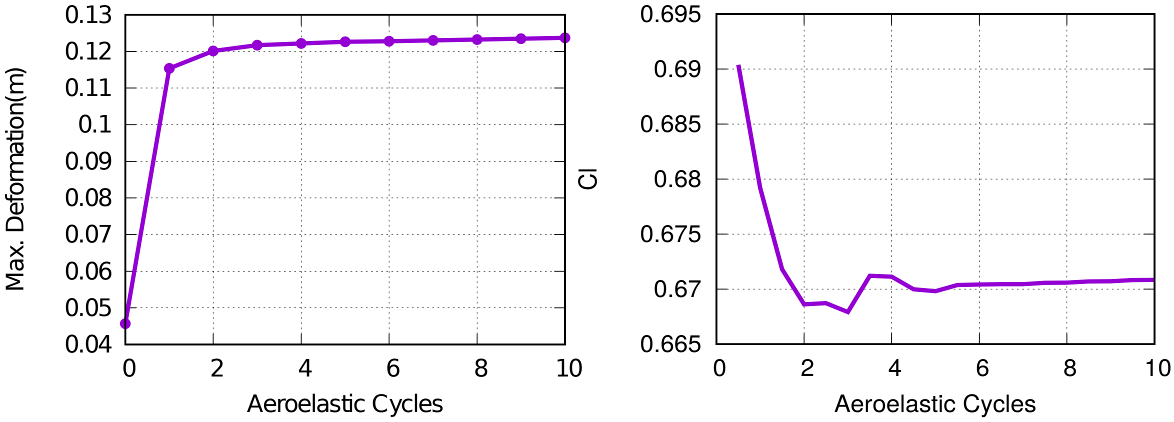

Figure 6.14: *Case 1. Evolution of the aeroelastic simulation, viscous flow model. Left: Cumulatively maximum deformation through the aeroelastic cycles. Right: Lift coefficient evolution through the aeroelastic cycles.*

pressure result, in the flexible material case, to a less bumpy surface wing and a higher aerodynamic load, Fig. 6.17 As a result, in the first aeroelastic cycle, the deformation has increased abruptly, in comparison to the composite material case, Fig. 6.16.

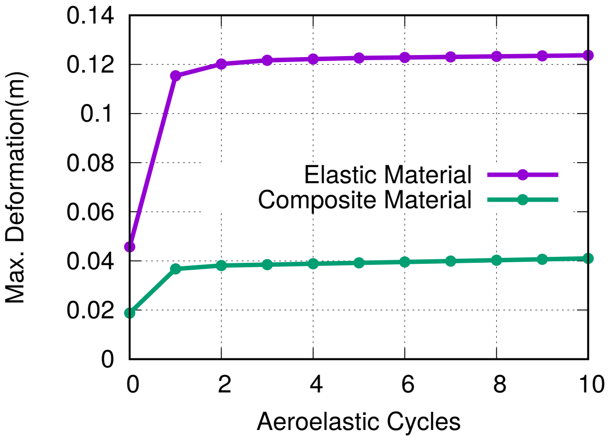

Figure 6.15: *Case 1. Comparison of the evolution of the aeroelastic for the two different materials.*

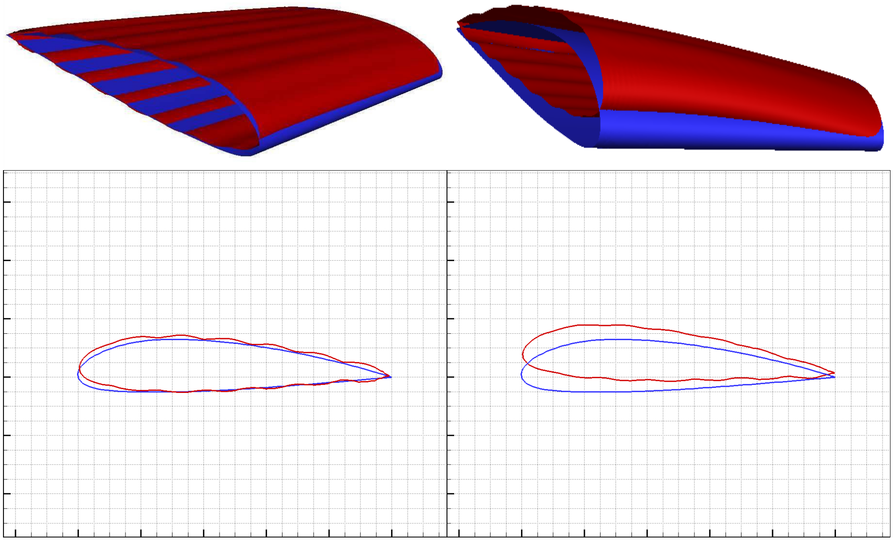

Figure 6.16: *Case 1. Comparison of the initial and deformed state for the two different materials , viscous flow model. Top-Left: The stiffer composite material, initial state (blue) and deformed at the end of aeroelastic cycles (red). Top-Right: The flexible material (same colours). Bottom: Corresponding airfoils on the symmetry plane (same colours).*

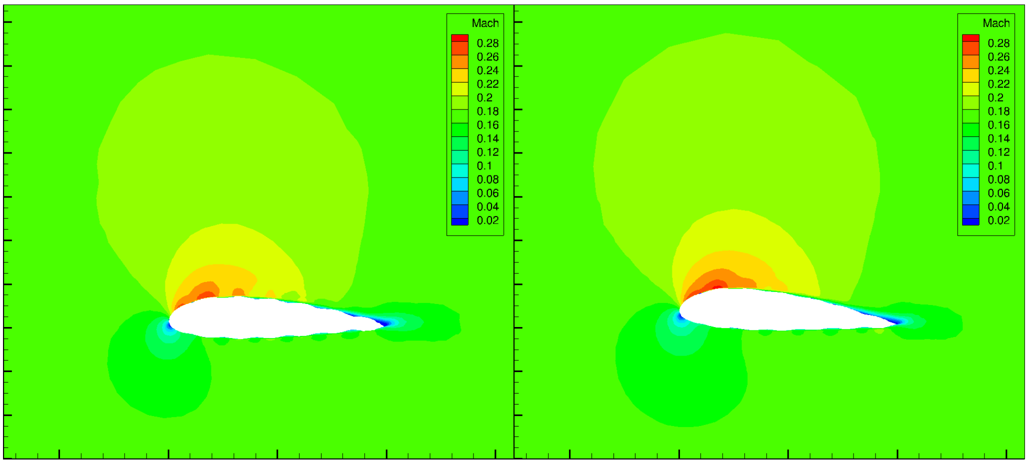

Figure 6.17: *Case 1. Comparison of the mach number iso-areas field on the symmetry plane for the two different materials, computations based on the RANS equations. Left: Stiffer composite material. Right: Flexible material.*

6.3 Case 2. Studies on a Caterpillar-shaped NACA4318 Wing

For conventional lifting surfaces the aerodynamic performance is normally of primary concern; however, in the design of inflatable wings, stiffness and manufacturability play a more significant role. By considering the above a different geometry is designed, using the NACA4318 airfoil profile, Fig. 6.18.

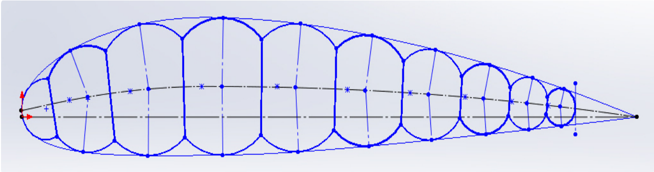

Figure 6.18: *Case 2. NACA4318 airfoil, approximated by circular profiles.*

In order to achieve an approximate airfoil shaped geometry the number of the internal compartments increased to 10 and the transverse ribs to 9. Also, for the purpose of manufacturability the last circle transverse rib (at the trailing edge) height was set to 1.5cm. resulting to the geometry shown in Fig. 6.19.

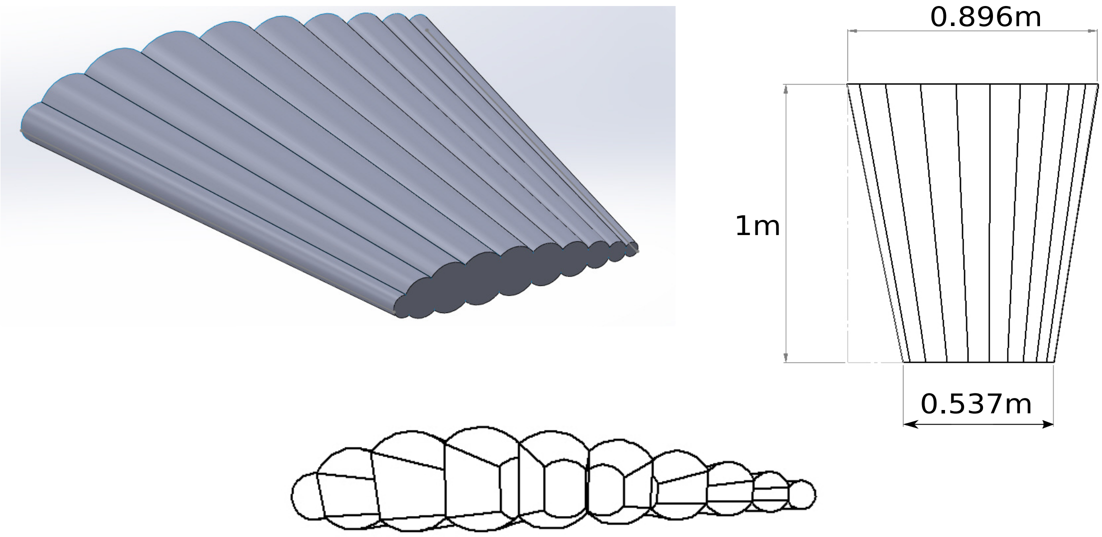

Figure 6.19: *Case 2. Caterpillar-shaped wing profile. Top-Left: the half of the 3D wing model. Top-Right: planform of the half wing. Bottom: the internal ribs.*

A hybrid grid of tetrahedra, pyramids, prisms and hexahedra is generated around half of the wing; the grid has $\sim 1.5 \times 10^6$ nodes and is shown in Fig. 6.20. The distance of the first nodes off the wall allows for resolution of the turbulent boundary layer down to the wall ($y+ < 1$).

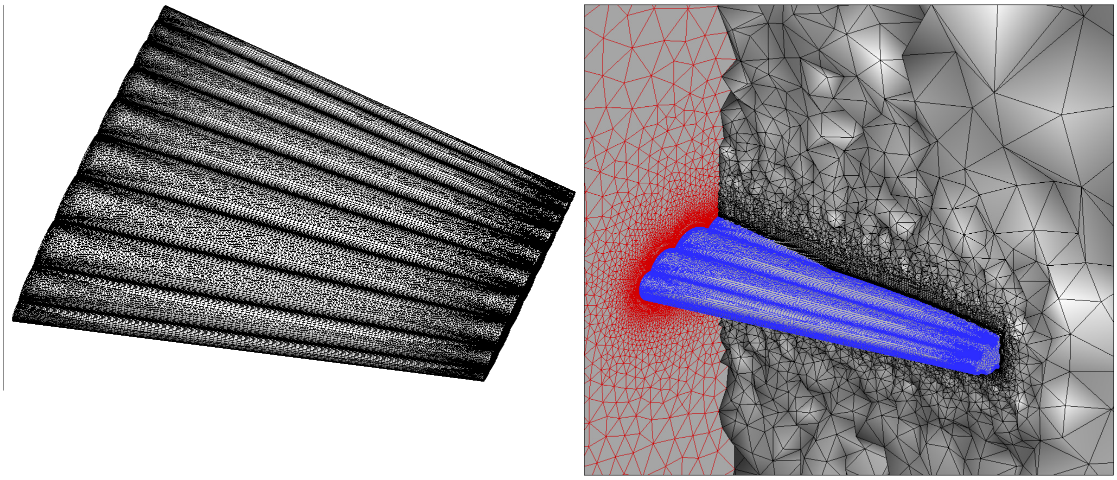

Figure 6.20: *Case 2. CFD grid for the solution of the RANS. Left: Hybrid surface grid on the inflated wing surface. Right: Hybrid volume grid around the wing.*

Material	Composite Material
Elements	Shell 181
Thickness	1 mm
Internal Pressure	120000 Pa

Table 6.7: *Case 2. Basic CSM solver inputs.*

Some data used for the structural model are presented in Table 6.7.
As shown in Fig. 6.21, the aeroelastic problem is practically well converged just after 5 aeroelastic cycles. The deviation of the maximum deformation in the last aeroelastic cycle is converged at the value of $7.5 \times 10^{-6}m$. and the lift coefficient at the value of 0.414.

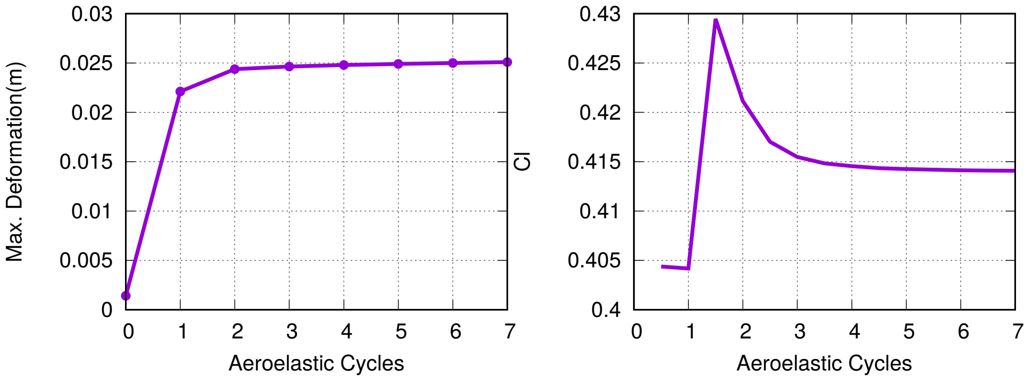

Figure 6.21: *Case 2. Evolution of the aeroelastic simulation, viscous flow model. Left: Cumulatively maximum deformation through the aeroelastic cycles. Right: Evolution of lift coefficient for 7 aeroelastic cycles.*

In Fig. 6.22, the convergence of all the equations during the last aeroelastic cycle is shown; it can be seen that the flow equations are considered to be converged. Each flow solution takes ∼ 40 min. on a single NVIDIA Tesla K40 GPU, the structural solution takes ∼ 3 min. on Intel I-5 CPU and the CFD grid deformation ∼ 5 min. on the same CPU. Thus, the cost for the solution of the whole aeroelastic problem using the numerical solution of the RANS equations for 7 aeroelastic cycles costs ∼ 6 hours.

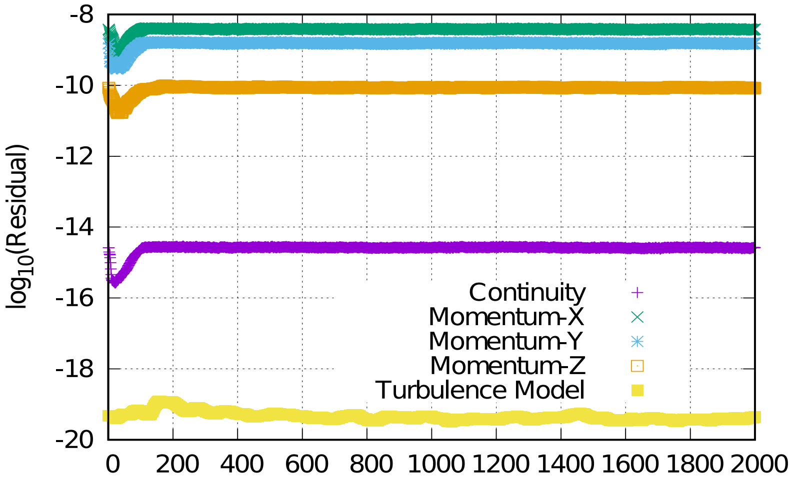

Figure 6.22: *Case 2. Top: CFD equations convergence for the last aeroelastic cycle with the RANS equations.*

As in case 1, after running the caterpillar-shaped wing with a pitch angle of 10° the same aeroelastic solution was performed for 3 different pitch angles 2° 5° and 8 ° in order to create the same polar curve as before, which is presented in comparison to the same curve computed for the NACA4318 wing, 6.23.

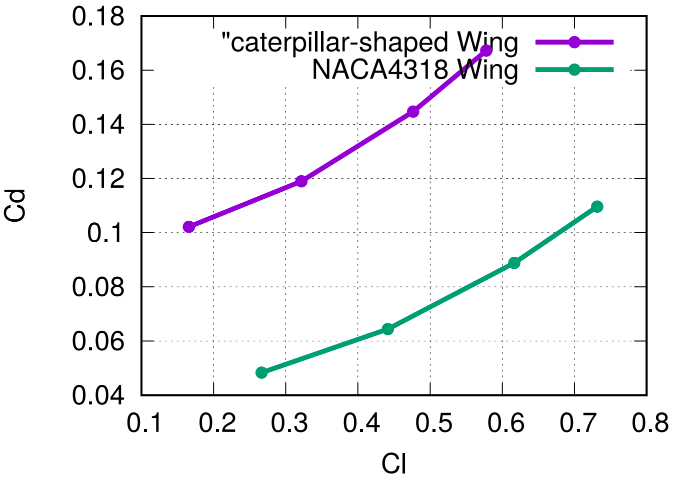

Figure 6.23: *Case 2. The computed polar (c_L vs. c_D). NACA 4318 wing has a smaller drag and a higher lift coefficient compared to the caterpillar-shaped one.*

From Fig. 6.24, it is obvious that with the same internal pressure and wall thickness the caterpillar-shaped wing has almost zero inflation, in the 'zeroth' cycle, since its circular profile withstands better with internal pressure loads. Also, the aerodynamic load produced from the caterpillar-shaped wing is smaller due to the disturbed flow around it, Fig. 6.25. This reduction in aerodynamic load results in a smaller computed maximum deformation in comparison with the NACA4318 shaped wing, Fig. 6.24.

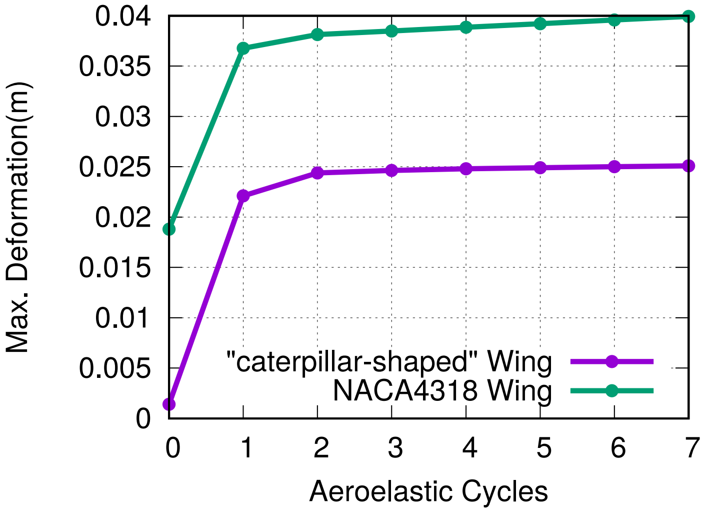

Figure 6.24: *Case 2. Evolution of the aeroelastic simulation, viscous model flow. Comparison of the cumulative maximum deformation between the caterpillar-shaped wing and NACA4318 one.*

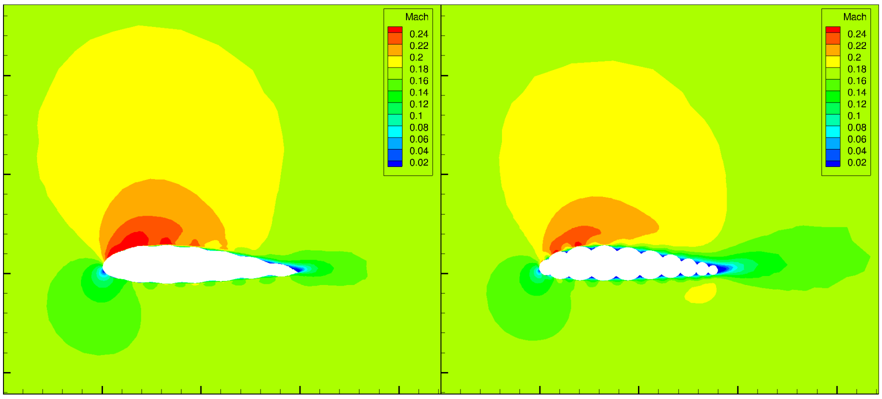

Figure 6.25: *Case 2. Comparison of the Mach number iso-areas on the symmetry plane, viscous flow model. The caterpillar-shaped wing has a much more disturbed flow resulting in less aerodynamic loads.*

6.3.1 Case 2 Revisited using a Flexible Material

A second run with a more flexible material is also performed. The CFD grid and the CFD solver inputs are the same. For the CSM setup, the material properties described in Table 6.4 are used and the internal pressure is 120000Pa. The aeroelastic simulation results in higher maximum deformation compared to the case with the composite material, Fig. 6.26. The resulting deformation along with the pressure distributions on the initial and the deformed wing are presented in Figs. 6.27 and 6.28, respectively.

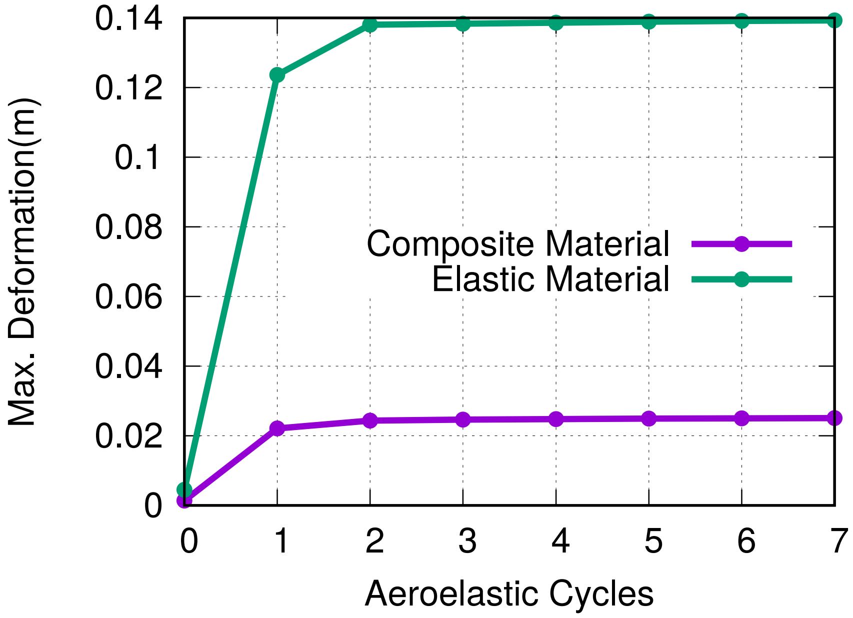

Figure 6.26: *Case 2. Comparison of the cumulative maximum deformation between the two materials on the caterpillar-shaped wing.*

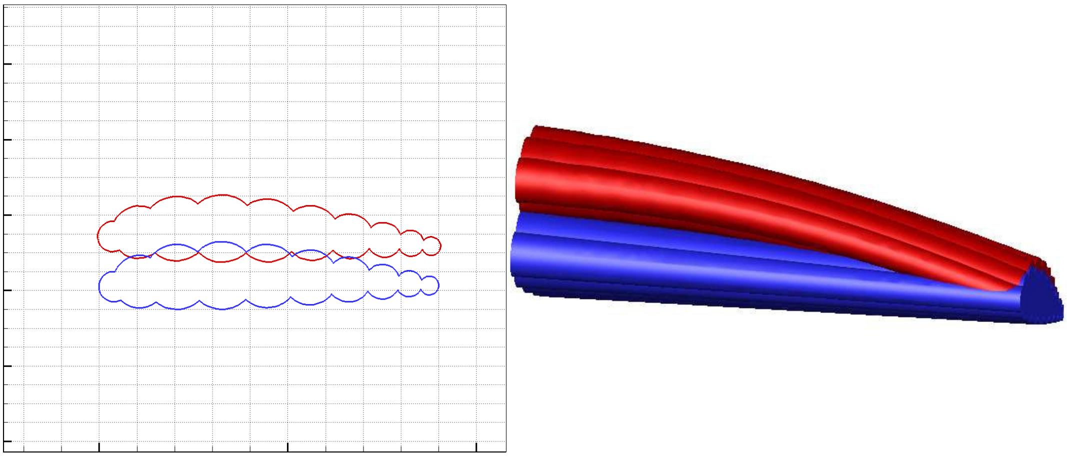

Figure 6.27: *Case 2. Deformation of the caterpillar-shaped wing. Left: View on the symmetry plane of the wing's outline initial (blue) vs. deformed (red). Right: Perspective view of the caterpillar-shaped wing from the initial state (blue) to the deformed one (red) at the end of the aeroelastic cycles.*

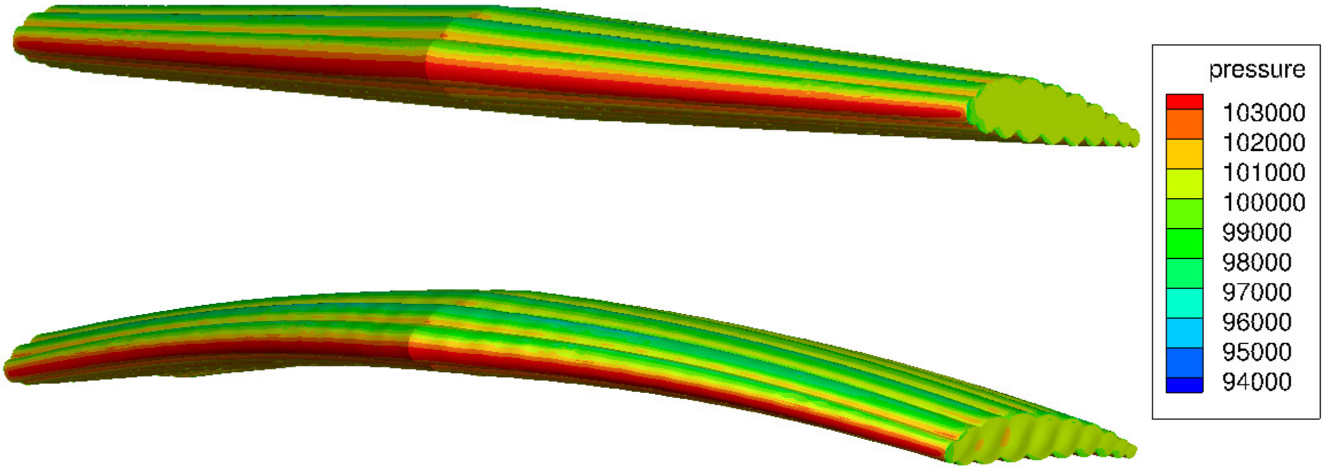

Figure 6.28: *Case 2. Top: Pressure distribution on caterpillar-shaped wing initial state. Bottom: Pressure distribution on deformed state after 10 aeroelastic cycle. (Both pressure fields calculated with viscous flow model).*

6.4 Case 3: Studies of the Inflatable NACA4318 Wing Including Tethers

In this case, the geometry of the wing is the same as in case 1. However, the basic difference is that the tethers are now included in the CSM analysis. The geometry used by the CSM model is shown in Fig. 6.29.

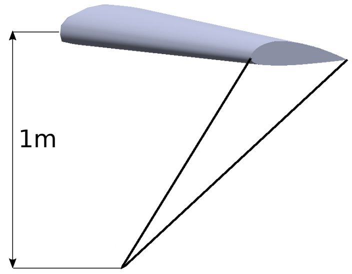

Figure 6.29: *Case 3. Half of the 3D wing model including two tethers.*

For the wing CSM model, the same material properties and elements are used as in case 1. Since, the tethers are included in the structural analysis, material, properties, elements and boundary conditions should be defined for them, Tables 6.8 and 6.9.

Material	Steel, see table 6.9
Elements	Beam 188 (used as bar element)
Cross Section	Circular

Table 6.8: *Case 3. FEM solver basic values for tethers.*

Density	$7850 kg/m^3$
Young' Modulus	$2 \times 10^{11} kg/ms^2$
Poisson's Ratio	0.3

Table 6.9: *Case 3. Steel Material Properties*

After defining the basic properties for the tethers, the boundary conditions of the CSM model change compared to case 1. Of course, the two supports used for representing the tether effect has been deleted. In case 3, the tethers' base (i.e. the bottom point where the four - for the whole wing - tethers converge) is considered to be fixed, constraining all degrees of freedom, Fig. 6.30. The only change done in case 3 affects the CSM model, since the tethers are not considered during the CFD analysis. No computation was made regarding the lift produced by the device and, in particular, in comparison with the weight of the tethers made of steel.
As shown in Fig. 6.31, the aeroelastic problem is practically well converged after 8

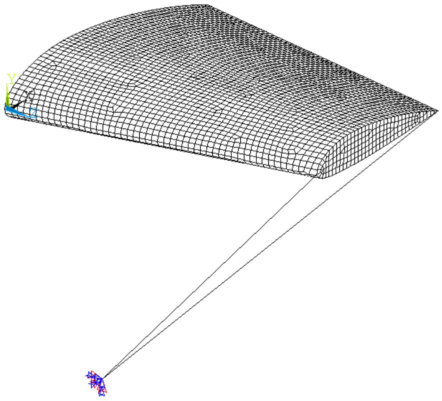

Figure 6.30: *Case 3. The CSM model containing the tethers.*

aeroelastic cycles. The variation of the maximum deformation computed in the last aeroelastic cycle is equal to $8.23 \times 10^{-5}m$.

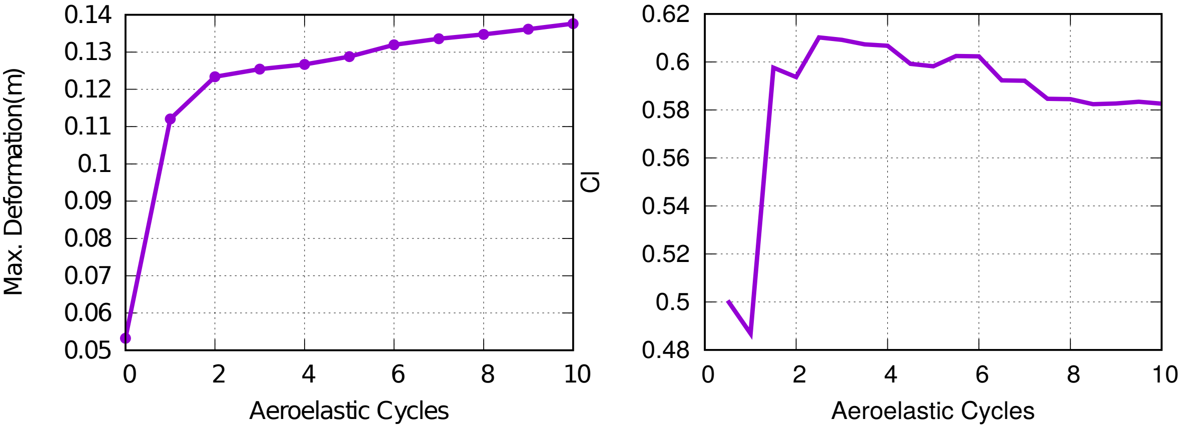

Figure 6.31: *Case 3. Evolution of the aeroelastic simulation of NACA4318 with tethers, using viscous flow model. Left: Cumulative maximum deformation in each aeroelastic cycle. Right: Evolution of the lift coefficient through the aeroelastic cycles.*

Comparing the maximum deformation changes with the standard airfoil shaped wing, it is obvious that in case 3, including the tethers, the presented deformations are higher. In both cases, the internal inflation pressure and the uniform CFD pressure are the same, however the tether let the geometry 'shrink' in the z-axis during the inflation compared to the case where supports are directly applied to the wing (without tethers), the difference in the 'zeroth' aeroelastic cycle between the cases is shown in Fig. 6.32. Also, the deformation is much higher, since the position of the tethers gives much more freedom to the structure to move, Fig 6.33.

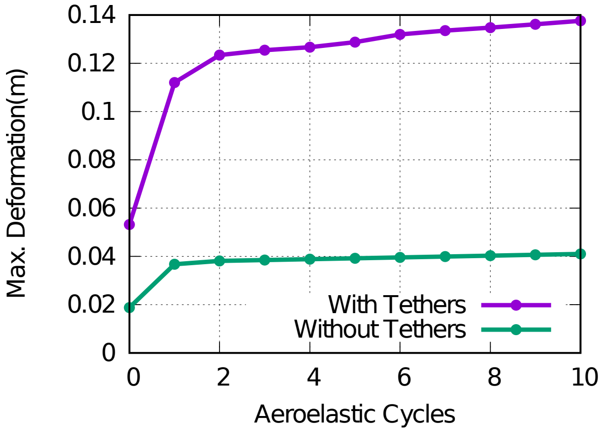

Figure 6.32: *Case 3. Comparison of the cumulative maximum deformation between the wing with tethers and the wing with the direct supports, using the RANS equations.*

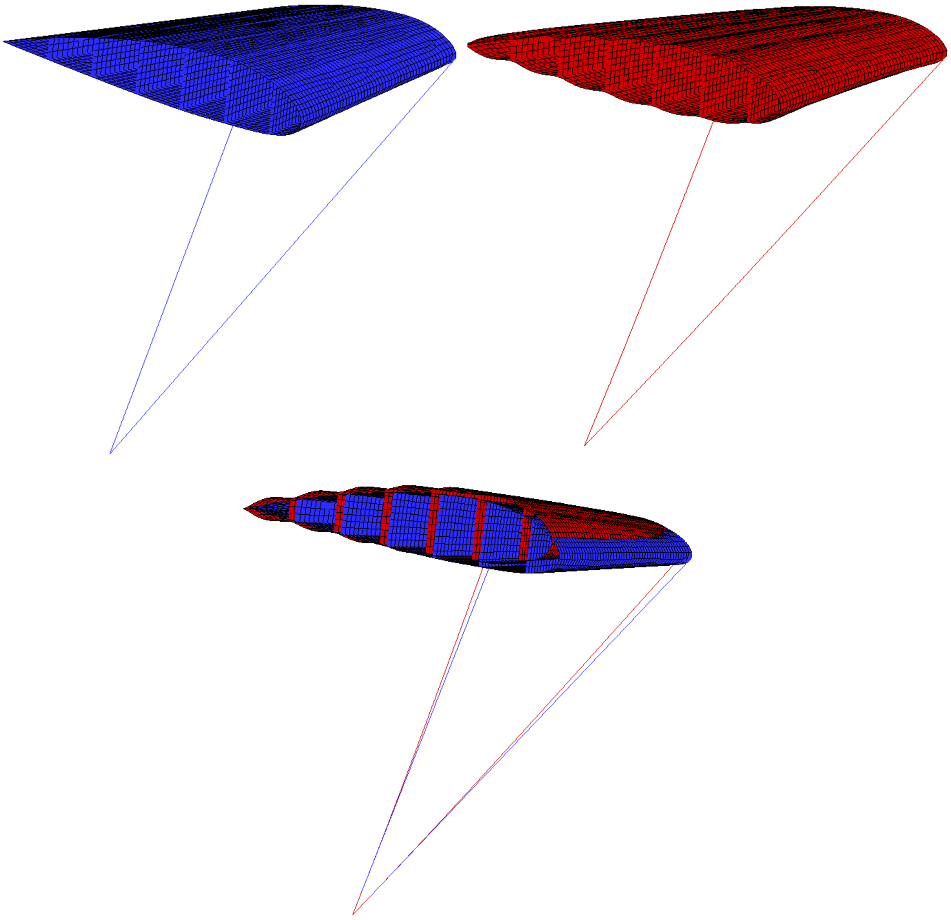

Figure 6.33: *Case 3. NACA4318 with tethers. Top-Left: The initial CSM model before aeroelastic cycles. Top-Right: The deformed CSM model at the end of the 10th aeroelastic cycle. Bottom: The difference between the initial (blue) and the deformed (red) state.*

6.5 Case 4: Studies on the Inflatable NACA0012 Wing

6.5.1 Aeroelastic Problem Using Euler Equations

As in case 1, a standard NACA0012 profile, with 7 internal compartments is used for the geometry creation. However, in cases 4 and 5 the airfoil is not tapered in order to create the wing and instead is extruded along the z-axis, Fig. 6.34. The CFD grid is created in the same way as case 1. A hybrid grid consisting of $\sim 2.1 \times 10^5$ nodes of tetrahedra, pyramids, prisms and hexahedra is generated around the half of the wing nodes. Data used for the structural model are presented in Table 6.5. Using the variation in the lift coefficient and the maximum deformation as convergence criteria, the aeroelastic problem has converged after 4 aeroelastic cycles, Fig 6.35. In the last aeroelastic cycle the variation of the maximum deformation is equal to $6.72 \times 10^{-5} m$. In comparison with case 1 NACA4318 using the wing, the new wing with the NACA0012 airfoil has converged to a smaller value of the lift coefficient resulting in smaller aerodynamic load and deformation magnitude, Fig. 6.36, with the pitch angle equal in both case to 10° and the same farfield conditions.

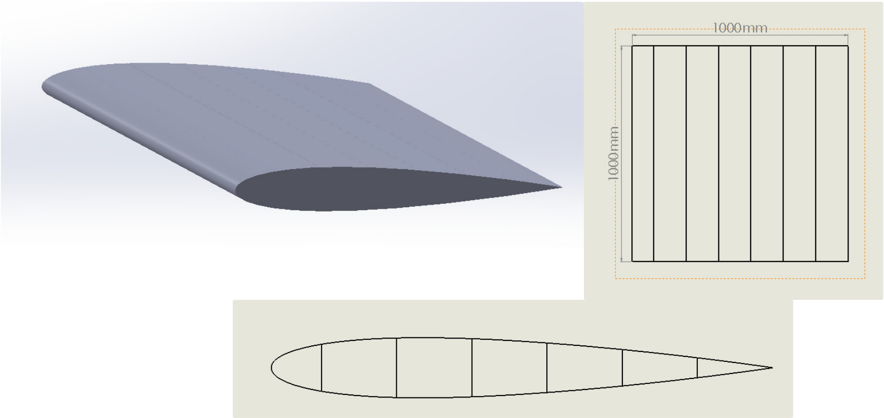

Figure 6.34: *Case 4. NACA0012 airfoil shaped wing. Top-Left: Half of the 3D wing model. Top-Right: Planform of the half wing. Bottom: The internal ribs.*

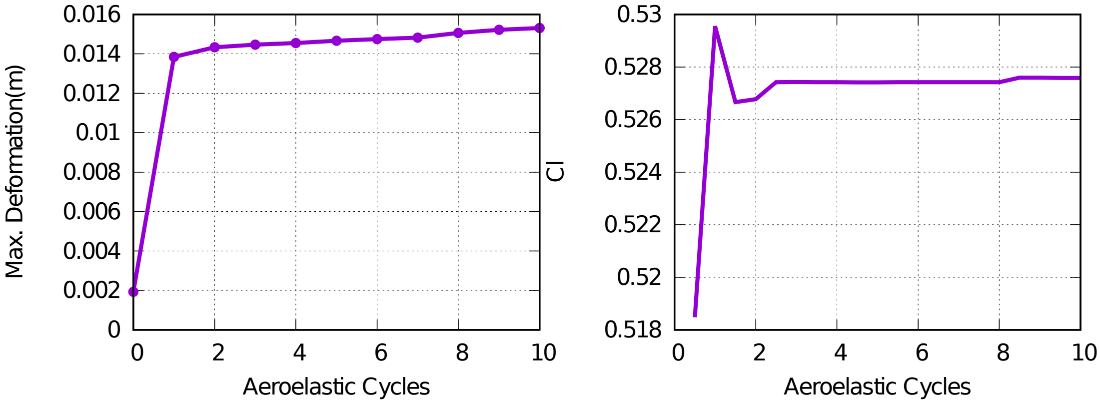

Figure 6.35: *Case 4. Evolution of the aeroelastic simulation, inviscid flow model. Left: Cumulatively maximum deformation through the aeroelastic cycles. Right: Lift coefficient evolution through the aeroelastic cycles.*

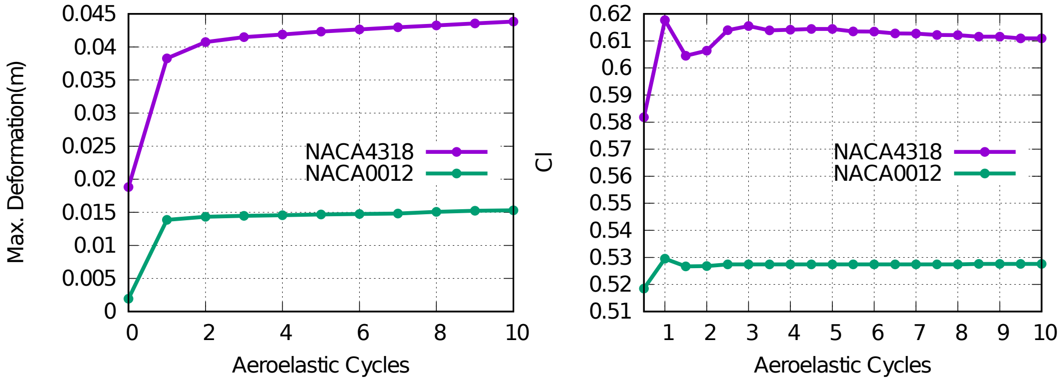

Figure 6.36: *Case 4. Comparison between NACA4318 and NACA0012 wings, inviscid flow model. Left: Cumulatively maximum deformation through the aeroelastic cycles, with all other data the same. Right: Lift coefficient evolution through the aeroelastic cycles.*

6.5.2 Aeroelastic Problem Using the RANS Equations

As before, next step is to solve the same problem using Navier-Stokes equations. The CSM model is kept the same. The CFD grid is changed, since the RANS equations need a finer grid, especially close to the wall, in order to obtain proper boundary resolution. The new unstructured grid contains $\sim 9.2 \times 10^5$ nodes, Fig. 6.37.

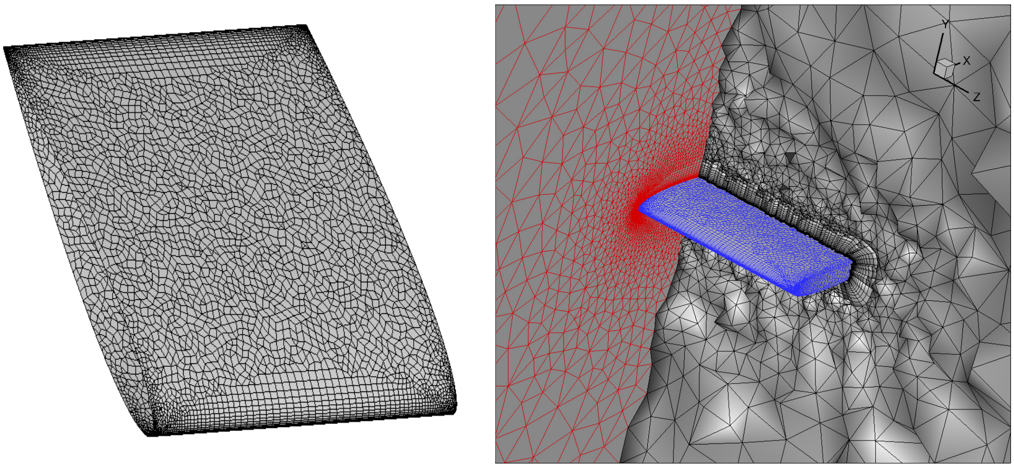

Figure 6.37: *Case 4. CFD grid for the RANS equations. Left: Hybrid surface grid on the wing surface. Right: Hybrid volume grid around the wing. The wing surface is shown in blue and the symmetry boundary in red.*

Using the RANS equations the aeroelastic problem is well converged after three cycles, Fig. 6.38. The variation of the maximum deformation between the last aeroelastic cycle and the previous one is equal to $5.66 \times 10^{-5}m$. A comparison of the convergence of the aeroelastic loop between NACA4318 wing and NACA0012 wing shows that NACA4318 produces higher lift coefficient and consequently aerodynamic load, which reluts in higher deformations, Fig. 6.39.

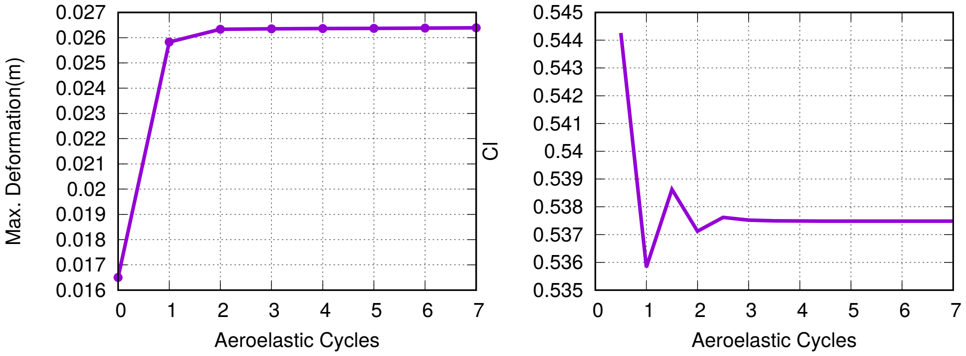

Figure 6.38: *Case 4. Evolution of the aeroelastic simulation, NACA0012 airfoil. Left: Cumulative maximum deformation through aeroelastic cycles. Right: Lift coefficient evolution through aeroelastic cycles.*

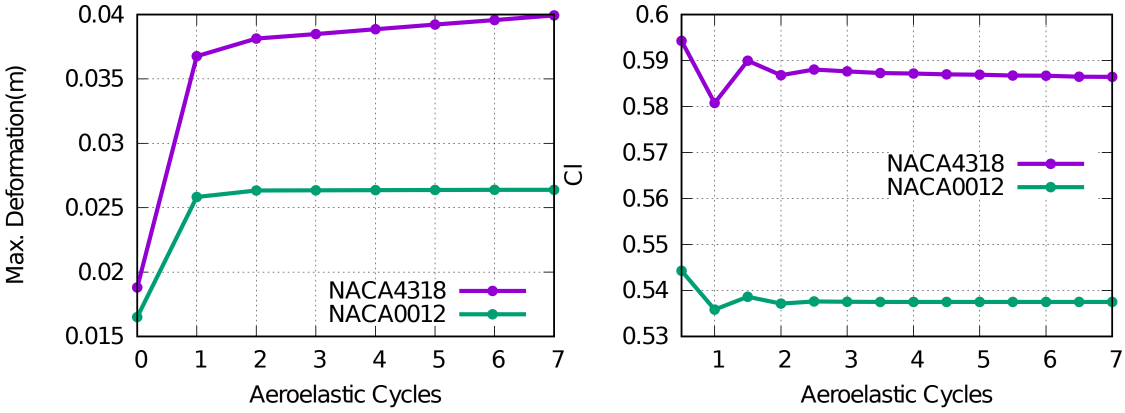

Figure 6.39: *Case 4. NACA0012 vs. NACA4318 wings' evolution of the aeroelastic simulation. Left: Cumulative maximum deformation. Right: Comparison of the lift coefficient evolution.*

6.5.3 Case Revisited using a Flexible Material

The only change that has to be made is in the CSM model as before the values defined in Tables 6.4 and 6.6 are used. The aeroelastic problem is well converged after 3 aeroelastic cycles, since the variation of the maximum deformation is equal to $4.78 \times 10^{-5} m$. Fig 6.40. In Fig. 6.41 the change in the pressure distribution on the surface wing caused by the change of the wing shape can be seen.

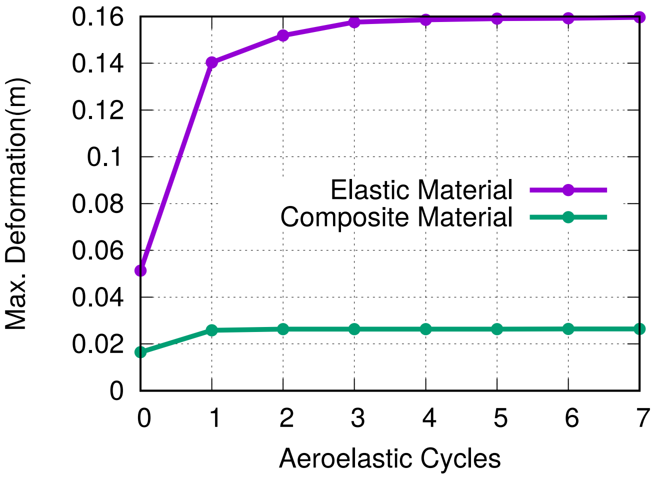

Figure 6.40: *Case 4. NACA0012 airfoil cumulative maximum deformation, computed for two materials using viscous flow model.*

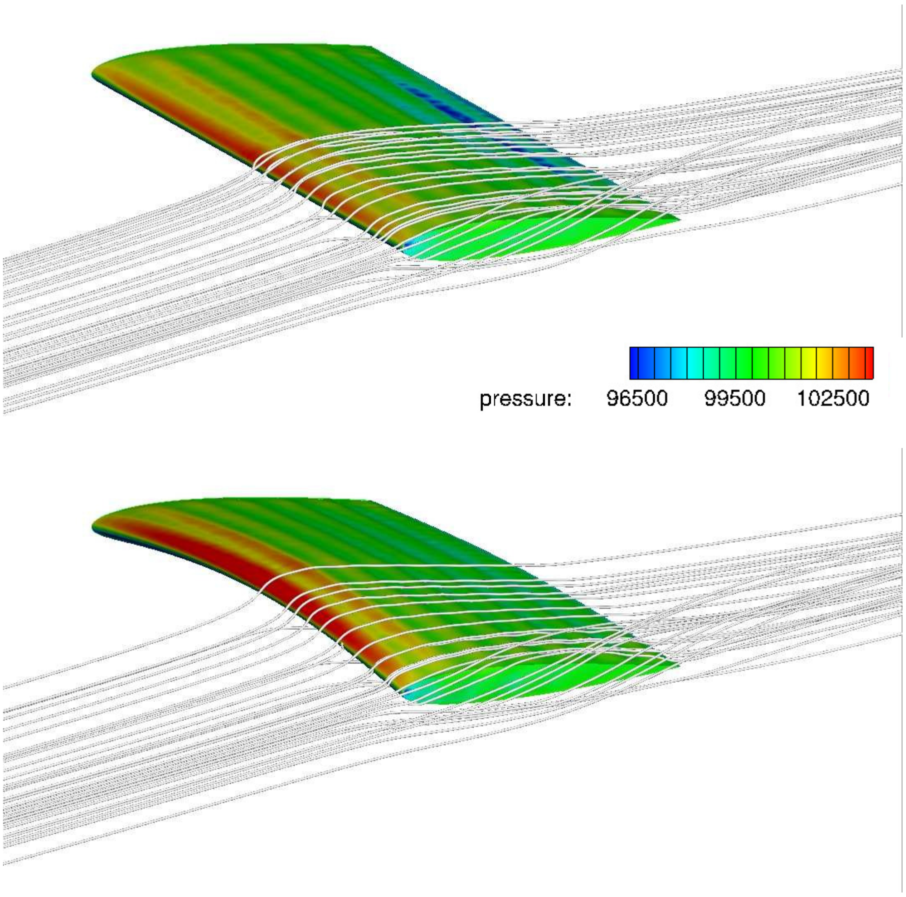

Figure 6.41: *Case 4. NACA0012 airfoil wing pressure field. Top: Pressure distribution and streamlines on the wing surface after the zeroth cycle. Bottom: Pressure distribution and streamlines at the end of the last aeroelastic cycle.*

6.6 Case 5. Studies of the Inflatable NACA0012 Wing Including Tethers

After analysing the NACA0012 wing with direct supports on the tip the next step is to include the tethers in the CSM model, as in case 3 Section 6.4, and the CSM data are defined in Table 6.8. For the CFD solver the RANS equations' grid is used, as in case 4 Section 6.5.1, and its basic inputs are defined at Table 6.2. The aeroelastic simulation, practically, converges after 5 cycles, Fig. 6.42. The change in the maximum deformation in the last aeroelastic cycle is equal to $2.82 \times 10^{-5} m$. The deformed wing including the new tethers position is compared with the initial (undeformed) shape, Fig. 6.43 The max. deformation with and without tethers is compared in Fig. 6.44. The presence of tethers allows for greater deformations compared to direct supports. A comparison of the max. deformation between the NACA0012 and NACA4318 wings both with tethers, Fig. 6.45, indicates that the NACA4318 wing results to higher aerodynamic loads and, thus, higher deformations.

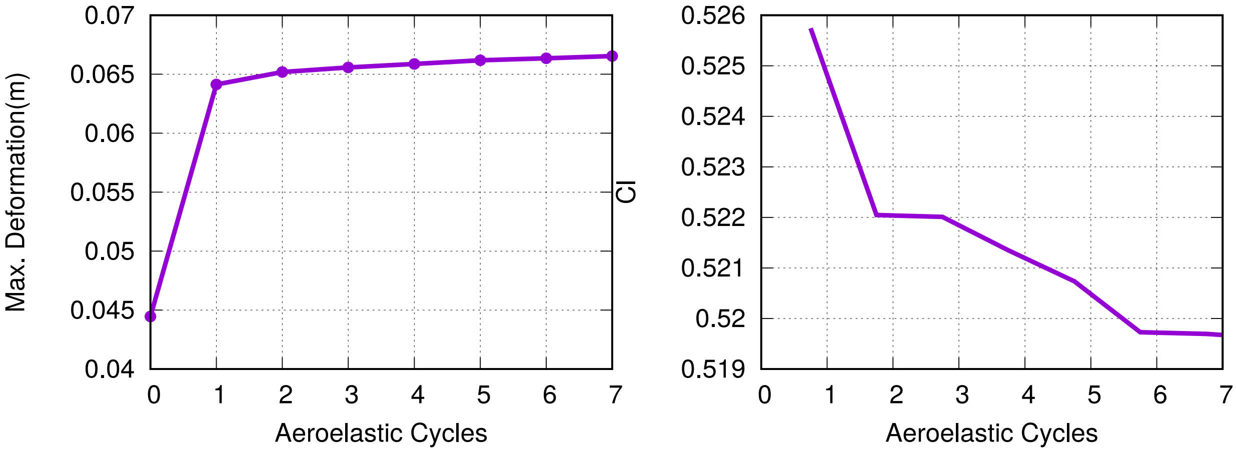

Figure 6.42: *Case 5. NACA0012 wing with tethers aeroelastic convergence, using viscous flow model. Left: Cumulative maximum deformation through aeroelastic cycles. Right: Evolution of the lift coefficient through the aeroelastic cycles.*

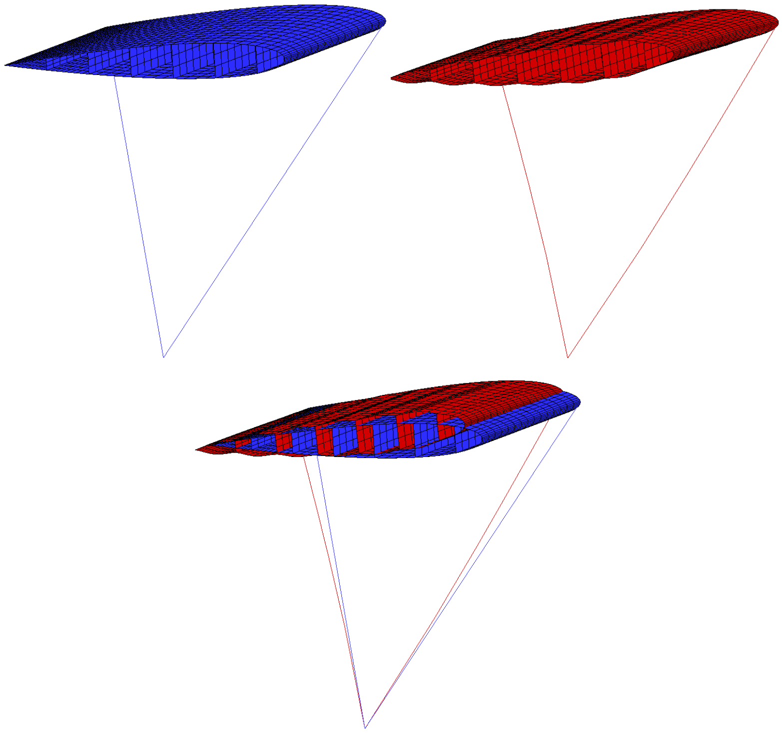

Figure 6.43: *Case 5. NACA0012 wing with tethers. Top-Left: Initial CSM model before the aeroelastic solution. Top-Right: Deformed CSM model at the end of the seventh aeroelastic cycle. Bottom: The comparison between the initial (blue) state and the deformed (red) state.*

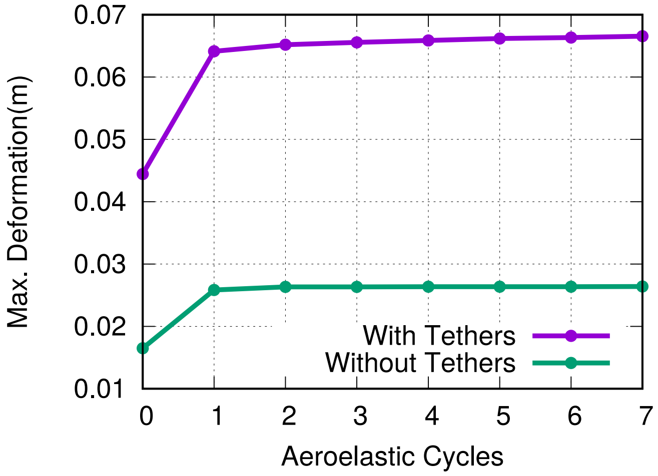

Figure 6.44: *Case 5. For NACA0012 wing the sum of the maximum deformation with and without tethers. As expected the case with tethers allow the wing to deform compared to the wing with the direct supports.*

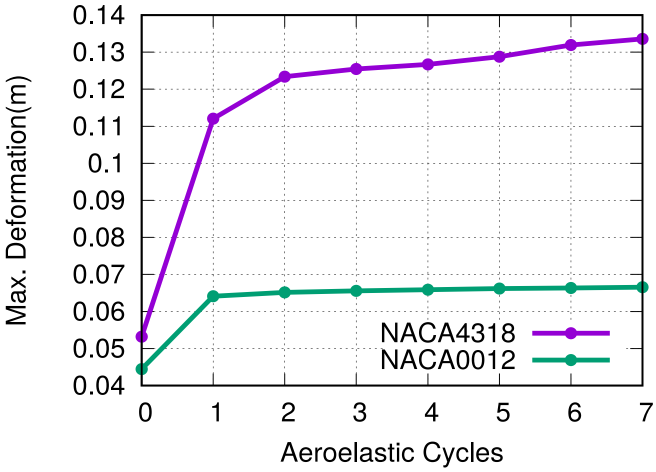

Figure 6.45: *Case 5. Comparison of the cummulative maximum deformation between the NACA0012 and NACA4318 wings, both with tethers.*

6.7 Summary and Discussion

The results obtained with the turbulent flow model in all cases using the NACA4318 wing are summarized in Table 6.10. In Table 6.10, the difference between the undeformed NACA4318, the smooth NACA4318 at the end of the aeroelastic cycles and the caterpillar-shaped NACA4318 at the end of the aeroelastic cycle, can be seen. The deformation for the standard NACA4318, made of composite material, is relatively small thus the computed drag forces are similar to the undeformed one's. However the slightly bumpy surface caused from the inflation affects the computed lift force. The same effect is much more pronounced in the case of the caterpillar-shaped wing, in which the computed drag force is higher and the lift force has decreased significantly compared to the undeformed standard NACA4318 wing. The presence of tethers seems not to affect the computed forces, despite the fact that such an assembly allows for higher deformations compared to the case with the supports. Finally, the comparison between the composite and elastic material shows that the high deformations increase the drag forces, since the whole wing is raised from position and tilted back, however the change in position also increases the computed lift, in comparison to the composite material case.

All results produced with viscous flow model				
Case	**Material Used**	**Drag (N)**	**Lift (N)**	**Maximum Deformation(m)**
Case 1 (NACA4318)	Undeformed	186.14	1405.33	-
Case 1 (NACA4318-Supports)	Composite/Stiff	189.48	1257.23	0.045
Case 1 (NACA4318-Supports)	Elastic/Flexible	209.18	1436.09	0.125
Case 2 (Caterpillar-shaped Wing-Supports)	Composite/Stiff	258.00	889.26	0.025
Case 2 (Caterpillar-shaped Wing-Supports)	Elastic/Flexible	289.92	1159.13	0.142
Case 3 (NACA4318-Tethers)	Composite/Stiff	192.36	1226.02	0.134

Table 6.10: *Comparison of drag, lift forces and the maximum deformation in NACA4318 cases.*

Chapter 7

Overview and Conclusions

7.0.1 Overview

The work presented in this diploma thesis concerned the aeroelastic analysis of inflatable wings and, to this end, solvers for the CFD and CSM models were used and their interfaces were built. To be more specific, in this diploma thesis the following tasks were undertaken:

- To study the aeroelastic behaviour of inflatable wings.
- In order to perform the aeroelastic analysis, except of the in-house GPU-enabled CFD solver, a CSM s/w was needed to perform the structural analysis. The commercial s/w MAPDL (counterpart of the ANSYS) was used, since it offered the capability to be executed in batch mode from a script.
- After defining the two basic solvers, in order to be able to perform a fully automated aeroelastic loop, FSI tools were needed. Those tools were either programmed or the integrated tools offered by ANSYS were used. Throughout this diploma thesis, our policy was to prefereably use, the in-house tools since they provided better control over the problem solution.
- After programming the FSI tools and creating the aeroelastic loop, analyses of inflatable wings and investigations regarding the shape, the material and the supports of them were performed. Finally, some first results about the aeroelastic behaviour of inflatable wings were extracted.

Some benefits from the developed tools are listed below:

- A new tool, capable of performing aeroelastic analysis on inlfatable wings. is made available. This tool combines in-house (for the CFD part) and commercial (for the CSM part) tools. The replacement of any of them with another similar tool is almost straightforward, especially once we have programmed our interfacing tools.

- The programmed aeroelastic loop is fully automated and the file formats used are universal and versatile.
- As this thesis was drawn up, it was the first time that the in-house GPU enabled code PUMA was coupled with an external CSM solver in an aeroelastic loop. As a result, this thesis was a test for the capabilities of the PUMA, to support aeroelastic analysis loops.
- The shape function based interpolation tool performs very well in rebuilding the new CFD surface mesh according to the computed deformations, without impairing the CFD surface grid, which happened with other tools.
- Once all the above are ready and fully operational, next step is to proceed to the shape optimization of inflatable wings, using either evolutionary algorithms or adjoint methods.

Appendix A

Wing Geometry Parameterization

In this appendix, the process of parameterization of the wing geometry is presented. Specifically, the creation of the 3D NACA4318 geometry, used in case 1 6.2 is described. The first step is to obtain several points describing the shape of the selected airfoil. In our case using an online tool, [28], the coordinates of a NACA4318 airfoil are obtained. The origin of the coordinate system is located at the leading edge of the airfoil and points in the XY plane are created, Fig. A.1.

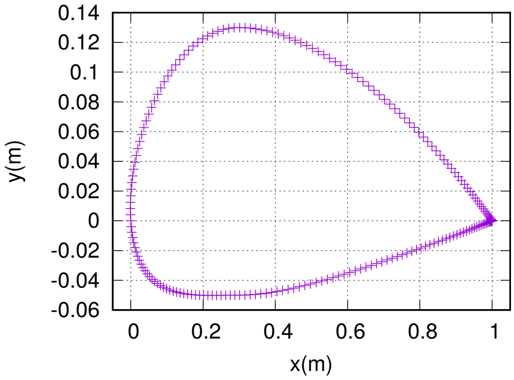

Figure A.1: *Case 1. NACA4318 initial points used for the creation of the geometry. Axis not in scale.*

After exporting the points in a (x, y) format, they are inserted in a commercial CAD s/w and a curve is fitted around those points. Having the outline of the airfoil, next step is to tapper it along z axis in order to create a wing, Fig. A.2. After, creating the outside skin of the wing, the internal compartments of our geometry are created and the whole geometry is exported as an IGES file, which is a neutral file form suitable for the CFD grid generation s/w and for the CSM solver s/w.

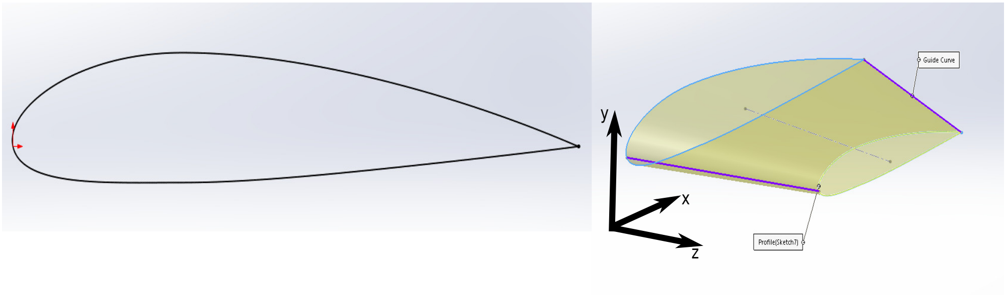

Figure A.2: *Left: Curve fitted around points. Right: Airfoil tapered along z-axis.*

Appendix B

The LTT Format

In this appendix, the format used by the PUMA CFD code is presented. The computational grid is described in a set of three files, all of which consist the so-called Lab of Thermal Turbomachines (LTT) format. These files are:

- The .nod file, containing the x, y, z coordinates of all the nodes.
- The .hyb file, containing the element connectivity of the grid.
- The .patch file, containing the information on the boundary patches of the mesh.

The .nod file

The first file is the .nod file containing the x, y and z coordinates of the grid nodes. In the first line of the file, the total number of nodes is written, while in the next three lines the x, y and z coordinates of each node are written, respectively, Fig. B.1.

$$\begin{array}{llll} nbNodes & & & \\ nodeX^1 & nodeX^2 & nodeX^3 & \ldots \\ nodeY^1 & nodeY^2 & nodeY^3 & \ldots \\ nodeZ^1 & nodeZ^2 & nodeZ^3 & \ldots \end{array}$$

Figure B.1: *Representation of the .nod file structure where* $nodeX_i$*,* $nodeY_i$ *and* $nodeZ_i$ *are the x, y and z coordinates, respectively, of the* $i-th$ *node.*

The .hyb file

The second file is the .hyb file, containing element connectivities. In the first line of the file the total numbers of tetrahedra (nbTet), pyramids (nbPyr), prisms (nbPri)

and hexahedra (nbHex) is written. In the following lines, the nodal IDs of each element are written, Fig. B.2, where
$iHex^{1}{}_{1}iHex^{2}{}_{1}iHex^{3}{}_{1}iHex^{4}{}_{1}iHex^{5}{}_{1}iHex^{6}{}_{1}iHex^{7}{}_{1}iHex^{8}{}_{1}$,
for example, are the nodal IDs of the nodes of the first hexahedron. The nodal IDs of each element type are written in a separate line.

$$\begin{array}{lllllllll}
nbTet & nbPyr & nbPri & nbHex \\
iTet_1^1 & iTet_1^2 & iTet_1^3 & iTet_1^4 \ldots \\
iPyr_1^1 & iPyr_1^2 & iPyr_1^3 & iPyr_1^4 & iPyr_1^5 \ldots \\
iPri_1^1 & iPri_1^2 & iPri_1^3 & iPri_1^4 & iPri_1^5 & iPri_1^6 \ldots \\
iHex_1^1 & iHex_1^2 & iHex_1^3 & iHex_1^4 & iHex_1^5 & iHex_1^6 & iHex_1^7 & iHex_1^8 \ldots
\end{array}$$

Figure B.2: *Representation of the .hyb file structure.*

The .patch file

The third and last file completing the three-file structure of the LTT format is the .patch file. This file contains all the necessary information concerning the grid boundaries (i.e. the patches). In the first line, the total number of patches is written. In the following lines, sections with pieces of information per boundary patch are written. Each section contains the name of the patch, the patch information and, finally, the list of nodal IDs that belong to it. Everything, except the patch name, is enclosed in curly brackets, Fig. B.3.

```
nbPatches
PatchName_1
{
    BCType boundaryConditionType | geometricTyp
    ConnectionID 1
                 .
                 .
                 .
    Nodes nbNodes
    list_of_patch_node_ids

}
PatchName_2
{
    BCType boundaryConditionType | geometricTyp
    ConnectionID 1
                 .
                 .
                 .
    Nodes nbNodes
    list_of_patch_node_ids

}
......
```

Figure B.3: *Representation of the .patch file structure.*

Appendix C

ANSYS Batch File Commands

In this Appendix, the basic batch commands used for the CSM model are presented. The MAPDL uses a scripting language in order to perform a batch analysis without using GUI. A sample of the script used in our case is presented with some comments explaining the commands used. First, the IGES format of the geometry is imported in the preprocessor of the s/w.

```
/AUX15
IOPTN,IGES,SMOOTH
IOPTN,MERGE,YES
IOPTN,SOLID,YES
IOPTN,SMALL,YES
IOPTN,GTOLER, DEFA
IGESIN,'NACA4318','IGES',' '
FINISH
```

Next, the elements to be used in the analysis, the material properties and the thickness of the shell element is defined.

```
/PREP7
!DEFINING ELEMENT
ET,1,SHELL181
!DEFINING MATERIAL PROPERTIES
MPTEMP,,,,,,,,
MPTEMP,1,0
MPDATA,EX,1,,9.3769E9
MPDATA,EY,1,,8.4116E9
MPDATA,EZ,1,,8.4116E9
MPDATA,PRXY,1,,0.36
MPDATA,PRYZ,1,,0.36
MPDATA,PRXZ,1,,0.36
MPDATA,GXY,1,,1.972E8
MPDATA,GYZ,1,,1.489E8
```

```
MPDATA,GXZ,1 , ,1.489E8
!DEFINING THICKNESS OF SHELL
SECT,1 ,SHELL, ,
SECDATA, 0.001 ,1 ,0.0 ,3
SECOFFSET,MID
SECCONTROL, , , , , , ,
```

Next step, is to create the CSM mesh.

```
TYPE,     1
MAT,           1
REAL,
ESYS,           0
SECNUM,     1
MSHAPE,0 ,2D
MSHKEY,0
FLST,2 ,21 ,5 ,ORDE,2
FITEM,2 ,22
FITEM,2 ,−42
AESIZE,P51X,0.02 ,
FLST,5 ,21 ,5 ,ORDE,2
FITEM,5 ,22
FITEM,5 ,−42
CM,_Y ,AREA
ASEL, , , ,P51X
CM,_Y1 ,AREA
CHKMSH, 'AREA'
CMSEL,S , _Y
ACLEAR, _Y1
AMESH, _Y1
CMDELE, _Y
CMDELE, _Y1
CMDELE, _Y2
/UI ,MESH,OFF
```

In this step the supports and the applied loads are defined.

```
/PREP7
ALLSEL
CMSEL,S ,SYMMETRY
DSYM,SYMM,Z ,
D,SYMMETRY, ,0 , , , , , ,UZ,ROTX,ROTY,
ALLSEL
D,FRONT, ,0 , , , ,UX,UY, , , ,
D,BACK, ,0 , , , , ,UY, , , ,
CMSEL,S ,PRESSURE
```

```
SF,PRESSURE,PRES,120000
ALLSEL
/INPUT,'PRESSURE_INT.dat'! PRESSURE FROM CFD INTERPOLATED TO CSM GRID
```

The stresses from the previous cycle are imported and applied.

```
/SOLU
NLGEOM,ON
INISTATE,SET,CSYS,-2
INISTATE,SET,DTYP,EPEL
INISTATE,READ,'./file.ist'
FINISH
```

The solution of the CSM model is performed.

```
/SOLU
INISTATE,WRITE,1, , , ,-2,EPEL
SOLVE
FINISH
SAVE, file,db,
```

Stresses and deformed geometry are written in a file in order for them to be used in the next step.

```
/PREP7
ALLSEL
UPGEOM,1,LAST,LAST,'file','rst',' '
FINISH
CDWRITE,DB
```

Appendix D

Stresses and Deformed Geometry through Aeroelastic Cycles

In chapter 5, during the presentation of the algorithm used for the CSM model, it is stated that the stresses and the deformed geometry are kept, in order to be used for the next aeroelastic cycle as initial state. In this Appendix, it is explained how by using the stresses and the deformed geometry of the previous cycle contributes to a more energy preserving algorithm. Let us assume that the CSM model is a simple spring on which a force F is applied, with F standing for the aerodynamic loads in our case. In its initial state the spring is undeformed and has no energy stored inside, Fig D.1. After the solution of the 'CSM' model for an 'aeroelastic' cycle, the spring is deformed and also an amount of energy is stored inside it. This energy is equal to the work produced by the acting force F and can be expressed as stresses. In the next cycle, the applied force changes in F'. It is obvious that, if the initial geometry, without any stress, is used for the new cycle, the work produced by F in the previous cycle will be lost. As a result, in order to preserve the work, the deformed geometry with the computed stresses from the previous cycle should be used as initial in the next one. After explaining with a simple example the need to store the deformed geometry and stresses a validation in our case is performed.

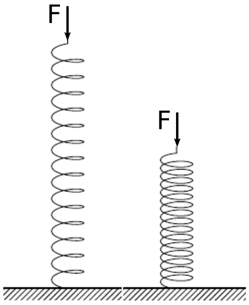

Figure D.1: *Left: Initial undeformed spring with the applied force. Right: Deformed spring at the end of an 'aeroelastic' cycle, with energy stored within.*

The wing, used in case 1 6.2 is deformed representing the zeroth cycle. Then, the deformed geometry and the computed stresses are used as initial state with the same supports as before. However, neither the internal inflation pressure nor the external aerodynamic pressure are applied and our wing should return to the initial undeformed state, D.2.

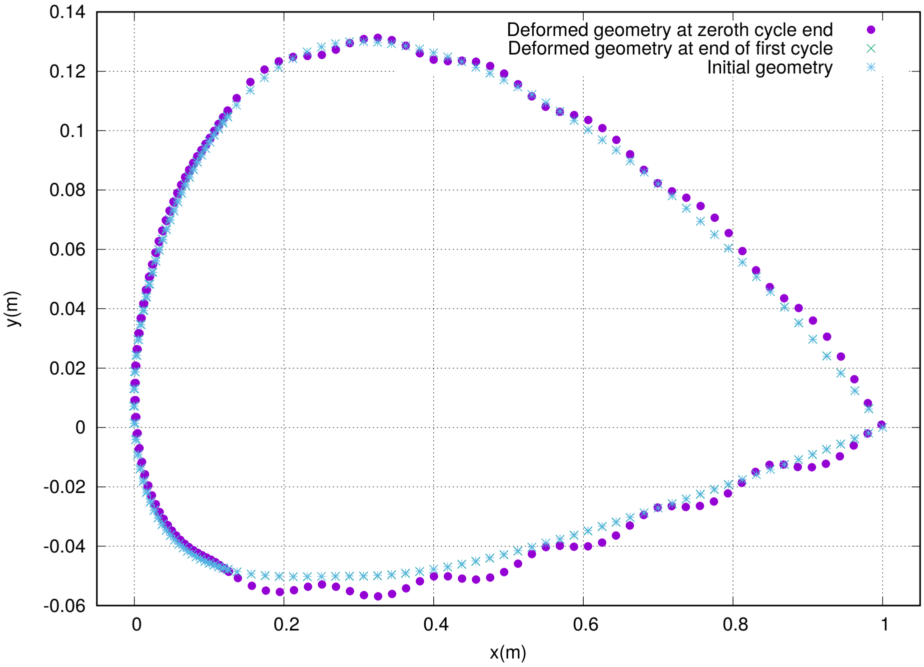

Figure D.2: *Case 1. View of the symmetry plane. Comparison of the initial airfoil (blue) shaped wing and the ones arising from the aeroelastic cycles. The shape of the wing is deformed after the zeroth cycle (purple) due to the inflation pressure and becomes more bumpy. However, after solving the again the CSM model without any external load, by using only the deformed geometry and the computed stresses from the zeroth cycle, as described above, the wing after the solution of the CSM model returns to its initial shape. Axis not in scale.*

Appendix E

Case 3. Revisited using a Composite Material for Tethers

In Case 3, the tethers' material is steel. This choice was made only for evaluating the wing's behaviour when the tethers are included in the CSM analysis and not to make any decisions about the tethers' material. After, evaluating wing's behaviour when tethers are included, a revision of the case 3 is performed. Specifically, the geometry, the CFD model and the basic CSM model are not changed. However, the tethers material and cross section are changed as described in Table E.1.

Tethers' Composite Material Properties	
Density	$1075 kg/m^3$
Young' Modulus	$2.4 \times 10^9 kg/ms^2$
Poisson's Ratio	0.3
Diameter of Circular Cross Section	$0.02m.$

Table E.1: *Case 3. New material for tethers.*

The new composite material is not as stiff as the steel, used in the previous analysis, however it is almost seven times lighter and in applications of producing renewable energy using inflatable wings weight plays a significant role.

The aeroelastic problem is converged sufficiently after 6 aeroelastic cycles, Fig. E.1. The deviation of the maximum deformation is converged to the value of $6.75 \times 10^{-4} m$. In comparison to the steel tethers model the composite material tether is more flexible and lets the assembly to deform at a higher degree, Figs. E.2, E.3.

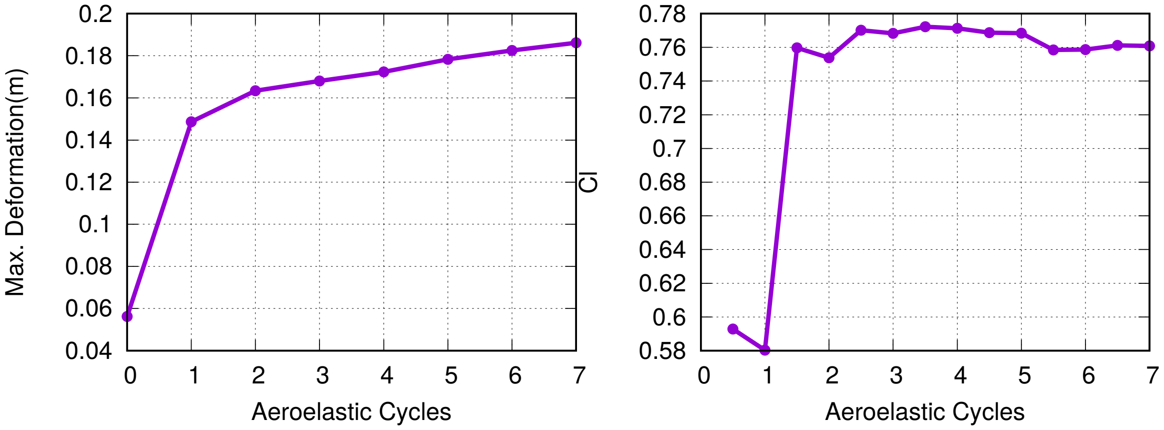

Figure E.1: *Case 3 Revision. Evolution of the aeroelastic simulation, viscous flow model. Left: Cumulatively maximum deformation through the aeroelastic cycles. Right: Lift coefficient evolution through the aeroelastic cycles.*

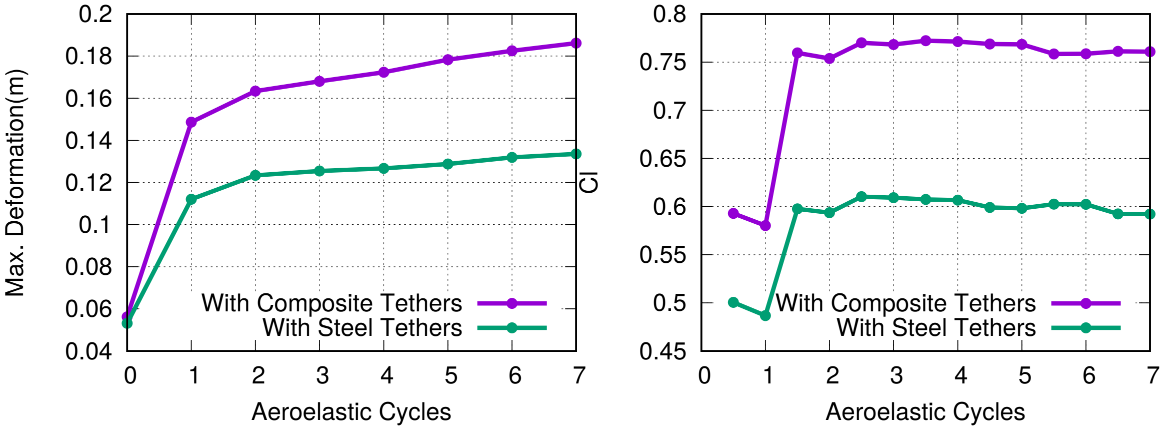

Figure E.2: *Case 3 Revision. Comparison of the evolution of the aeroelastic simulation, for the two different tethers' materials. The difference in the cumulatively maximum deformation and in the lift coefficient for the two cases.*

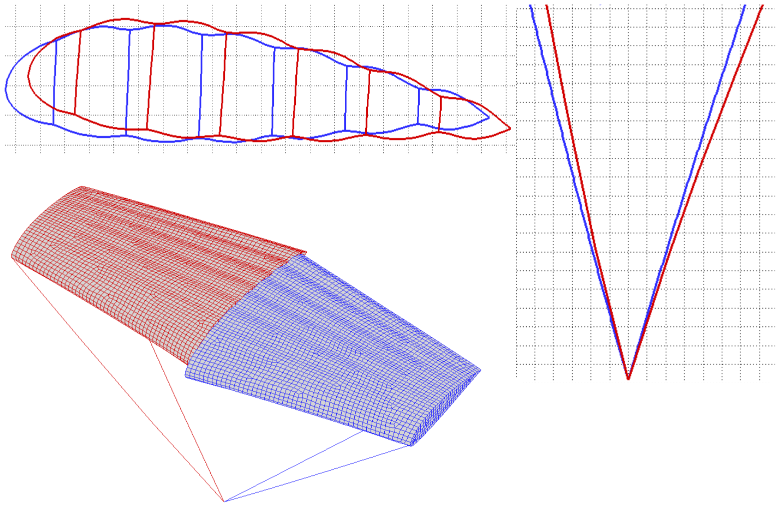

Figure E.3: *Case 3 Revision. Comparison of the deformed state at the last aeroelastic cycle for the two different tethers' material models. Top-Left: Corresponding airfoils at the symmetry plane, the model with steel tethers (blue) and the model with tethers made from composite (red). Bottom-Left: Perspective view of the models (same colours). Right: Tethers' difference in deformation (same colours).*

Bibliography

[1] A.Simpson: *Design and Evaluation of Inflatable Wings for UAV's.* PhD thesis, University of Kentucky, 2008.

[2] R. Chipman, A. Zislin and C. Waters: *Control of Aeroelastic Divergence.* AIAA Journal of Aircraft, 20:1007–1013, 1983.

[3] A. Natarajan: *Aeroelasticity of Morphing Wings using Neural Networks.* PhD thesis, Virginia Polytechnic Institute and State University, Blacksburg, Virginia, 2002.

[4] M. Paul: *Wing Deflection Analysis of 3d Printed Wind Tunnel Models.* Master Thesis. California Polytechnic State University, 2017.

[5] *Inflatable building.* `https://en.wikipedia.org/wiki/Inflatable_building`.

[6] *Inflatable boat.* `https://en.wikipedia.org/wiki/Inflatable_boat`.

[7] *Tire.* `https://en.wikipedia.org/wiki/Tire`.

[8] *Tokyo dome.* `https://en.wikipedia.org/wiki/Tokyo_Dome`.

[9] *Balloon.* `https://en.wikipedia.org/wiki/Balloon_(aeronautics)`.

[10] *Vega 1.* `https://en.wikipedia.org/wiki/Vega_1`.

[11] R. Norris and W. Pulliam: *Historical Perspective on Inflatable Wing Structures.* AIAA Paper 2009-2145, 50th AIAA/ASME/ASCE/AHS/ASC Structures, Structural Dynamics, and Materials Conference, Palm Springs, California, United States, May 4-7 2009.

[12] J.Rowe: *Finite Element Modeling of an Inflatable Wing.* Master Thesis. University of Kentucky, 2007.

[13] B. Cocke Jr.: *Wind-tunnel investigation of the aerodynamic and structural deflection characteristics of the Goodyear inflatoplane.* Technical Report NASA AA00006133_00001, 1958.

[14] J. Murray, J. Pahle, S. Thornton, S. Vogus, T. Frackowiak, J. Mello and B. Norton: *Ground and Flight Evaluation of a Small-Scale Inflatable-Winged Aircraft.* Technical Report NASA 20020039162, 2002.

[15] A. Cherubini, A. Papini, R. Vertechy and M. Fontana: *Airborne Wind Energy Systems: A review of the technologies.* Renewable and Sustainable Energy Reviews, 51:1461–1476, 2015.

[16] K. Tsiakas: *Development of shape parameterization techniques, a flow solver and its adjoint, for optimization on GPUs. Turbomachinery and external aerodynamics applications.* PhD thesis, Laboratory of Thermal Turbomachines NTUA, Athens, 2019.

[17] Asouti, V.G., Trompoukis, X.S., Kampolis, I.C., and Giannakoglou, K.C.: *Unsteady CFD computations using vertex-centered finite volumes for unstructured grids on Graphics Processing Units.* International Journal for Numerical Methods in Fluids, 67(2):232–246, 2011.

[18] Trompoukis, X.S., Asouti, V.G., Kampolis, I.C., and Giannakoglou, K.C.: *CUDA implementation of Vertex-Centered, Finite Volume CFD methods on Unstructured Grids with Flow Control Applications*, chapter 17. Morgan Kaufmann, 2011.

[19] P. Spallart and S. Allmaras: *A One-Equation Turbulence Model for Aerodynamic Flows.* AIAA Paper 92-0439 30th Aerospace Sciences Meeting and Exhibit Reno, Nevada, United States.

[20] ANSYS, Inc: *ANSYS 12–Theory Reference Manual*, 2009.

[21] *Strength of materials.* `https://mechanicalc.com/reference/strength-of-materials`.

[22] Χ. Προβατίδης: *Πεπερασμένα Στοιχεία στην Ανάλυση Κατασκευών.* Εκδόσεις Τζιόλα, 2016.

[23] F. Berna, H. Dohmen, J. Pei, S. Schuster and B. Won: *A Comparison of One-Way and Two-Ways Coupling Methods for Numerical Analysis of Fluid-Structure Interactions.* Journal of Applied Mathematics, vol. 2011, 2011.

[24] A. Farhat, M. Lesoinne and P. LeTallec: *Load and Motion Transfer Algorithms for Fluid/ Structure Interaction Problems with Non-Matching Discrete Interfaces: Momentum and Energy Conservation, Optimal Discretization and Application to Aeroelasticity.* Computer Methods in Applied Mechanics and Engineering, 157:95–114, 1998.

[25] G. Guruswamy: *A review of numerical fluids/structures interface methods for computations using high-fidelity equations.* Computers and Structures , 80:31–41, 2002.

[26] *Nasa common research model.* `https://commonresearchmodel.larc.nasa.gov/geometry/`.

[27] F. Gagliardi: *Shape parameterization and constrained aerodynamic optimization. Applications including turbomachines.* PhD thesis, Parallel CFD & Optimization Unit NTUA, Athens, In progress.

[28] *Airfoil tools.* `http://airfoiltools.com`.

Εθνικό Μετσόβιο Πολυτεχνείο
Σχολή Μηχανολόγων Μηχανικών
Τομέας Ρευστών
Μονάδα Παράλληλης Υπολογιστικής Ρευστοδυναμικής & Βελτιστοποίησης

Διατύπωση & Προγραμματισμός Μεθόδου Αλληλεπίδρασης Ρευστού-Στερεού & Εφαρμογές σε Φουσκωτές Πτέρυγες.

Διπλωματική Εργασία

Παπαγεωργίου Ε. Γεώργιος

Επιβλέπων: Κυριάκος Χ. Γιαννάκογλου, Καθηγητής ΕΜΠ

Αθήνα, 2019

ΕΚΤΕΝΗΣ ΠΕΡΙΛΗΨΗ ΣΤΑ ΕΛΛΗΝΙΚΑ

Αντικείμενο Εργασίας

Η διπλωματική αυτή εργασία έχει ως στόχο τη μελέτη της αεροελαστικής συμπεριφοράς ´φουσκωτών´ πτερύγων με τη χρήση του λογισμικού PUMA (**P**arallel solver, for **U**nstructured grids, for **M**ulti-blade row computations, including **A**djoint) [3],[7], της Μονάδας Παράλληλης Υπολογιστικής Ρευστοδυναμικής & Βελτιστοποίησης του ΕΜΠ (ΜΠΥΡΒ/ΕΜΠ) για την επίλυση των εξισώσεων ροής, του εμπορικού κώδικα MAPDL (**M**echanical **A**NSYS **P**arametric **D**esign **L**anguage), [2], ο οποίος αποτελεί τμήμα του εμπορικού λογισμικού ANSYS για την επίλυση των εξισώσεων του δομικής ανάλυσης καθώς και τη σύζευξη των δύο επιλυτών.

Εισαγωγή

Η βασική αρχή της αεροελαστικότητας είναι ότι η ροή ενός υγρού γύρω από ένα στερεό δημιουργεί αεροδυναμικές δυνάμεις οι οποίες προκαλούν την παραμόρφωση του. Αυτή η παραμόρφωση έχει ως αποτέλεσμα την ανακατανομή των αεροδυναμικών φορτίων, γεγονός που επηρεάζει την αεροδυναμική απόδοση του σώματος κ.ο.κ. Συνεπώς, για την επίτευξη της κατάστασης ισορροπίας απαιτείται η ταυτόχρονη επίλυση τόσο των εξισώσεων ροής όσο και των εξισώσεων που διέπουν τη μηχανική του στερεού σώματος.

Στη διπλωματική αυτή εργασία, η αεροελαστική ανάλυση επικεντρώθηκε σε ´φουσκωτές´ πτέρυγες (Inflatable wings). Ως φουσκωτό σώμα ορίζεται κάθε σώμα το οποίο αποκτά το σχήμα του και τη μηχανική του ευστάθεια λόγω του πεπιεσμένου ρευστού, συνήθως αέρα, στο εσωτερικό του. Τα οφέλη τέτοιων κατασκευών είναι το μειωμένο βάρος τους καθώς επίσης και η ευκολία αποθήκευσης τους όταν βρίσκονται σε ξεφούσκωτη μορφή. Η μελέτη σε τέτοιες κατασκευές, ιδιαίτερα τα τελευταία χρόνια, έχει εντατικοποιηθεί καθώς μπορούν να χρησιμοποιηθούν είτε σε διαστημικές αποστολές, λόγω του μικρού βάρους και όγκου, είτε για την παραγωγή ενέργειας μέσω ανανεώσιμων πηγών, όπως ο άνεμος, [1], Στο δεύτερο στοχεύει αυτή η εργασία.

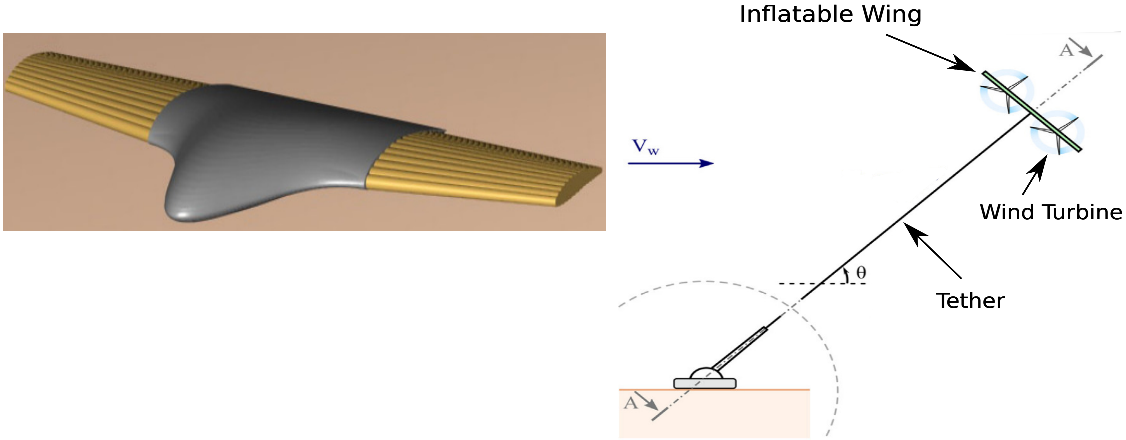

Σχήμα 1: *Χρήσεις φουσκωτών πτερύγων. Αριστερά: Όχημα εξερεύνησης από πρόγραμμα της NASA, [5]. Δεξιά: Αιωρούμενη ανεμογεννήτρια, η οποία τοποθετείται πάνω σε μία φουσκωτή πτέρυγα και συγκρατείται από κατάλληλα σχοινιά πρόσδεσης τα οποία μεταφέρουν παράλληλα την παραγόμενη ενέργεια, [1] .*

Κώδικας Υπολογιστικής Ρευστοδυναμικής (PUMA)

Η ΜΠΥΡΒ/ΕΜΠ έχει αναπτύξει έναν κώδικα ο οποίος επιλύει αριθμητικά τις εξισώσεις RANS (**R**eynolds **A**veraged **N**avier-**S**tokes, μαζί με ένα μοντέλο τύρβης στον τριδιάστατο χώρο, σε μη-δομημένα πλέγματα με τη χρήση της μεθόδου των πεπερασμένων όγκων. Εδώ, σε όλες τις περιπτώσεις, για την επίλυση της ροής χρησιμοποιείται το μοντέλο τύρβης των Spalart-Allmaras, [6]. Η εκτέλεση του κώδικα σε επεξεργαστές καρτών γραφικών (NVIDIA GPUs) παρέχει αξιοσημείωτη επιτάχυνση σε σύγκριση με αντίστοιχο λογισμικό το οποίο εκτελείται σε κεντρικές μονάδες επεξεργασίας (CPUs) μειώνοντας με αυτόν τον τρόπο δραστικά τον χρόνο κάθε επίλυσης. Το λογισμικό χρησιμοποιήθηκε για την πρόλεξη της ροής γύρω από την πτέρυγα για να υπολογιστούν τα αεροδυναμικά φορτία που ασκούνται σε αυτή.

Κώδικας Δομικής Ανάλυσης (MAPDL)

Για την επίλυση των εξισώσεων του στερεού σώματος χρησιμοποιήθηκε το λογισμικό MAPDL, (τμήμα του ευρύτερου λογισμικού της ANSYS) το οποίο στηρίζεται στη μέθοδο των πεπερασμένων στοιχείων για την επίλυση των εξισώσεων. Το λογισμικό προσφέρει στον χρήστη τη δυνατότητα να γράψει την αλληλουχία των εντολών σε μορφή γλώσσας προγραμματισμού και μπορεί να εκτελεί την επίλυση των εξισώσεων της μηχανικής χωρίς τη χρήση γραφικού περιβάλλοντος ή άλλης εξωτερικής παρέμβασης. Η δυνατότητα αυτοματοποίησης του αποδείχτηκε εξαιρετικά χρήσιμη καθώς το αεροελαστικό πρόβλημα για να συγκλίνει απαιτεί αρκετούς κύκλους επαναλήψεων. Το συγκεκριμένο λογισμικό χρησιμοποιήθηκε για τον υπολογισμό των παραμορφώσεων της αεροτομής που δημιουργούνται λόγω των ασκούμενων αεροδυναμικών φορτιών.

Σύζευξη των δύο Επιλυτών

Εκτός από τους δύο βασικούς επιλύτες, η μελέτη ενός αεροελαστικού προβλήματος απαιτεί υπολογιστικά εργαλεία ώστε να μεταφερθεί η πληροφορία από το ένα πλέγμα στο άλλο. Συγκεκριμένα, στα περισσότερα αεροελαστικά προβλήματα, όπως και σ΄ αυτό που μελετήθηκε στην εργασία αυτή, τα δύο πλέγματα που διακριτοποιούν το χωρίο του ρευστού και αυτό της κατασκευής δεν έχουν τον ίδιο αριθμό κόμβων και στοιχείων στη διεπιφάνεια τους. Συνήθως, το πλέγμα στο οποίο επιλύονται οι εξισώσεις ροής είναι πιο πυκνό, για την ακριβή πρόλεξη των συνεκτικών στρωμάτων, ενώ το πλέγμα στο οποίο επιλύονται οι εξισώσεις του στερεού δεν απαιτεί εξίσου την ίδια ανάλυση. Ως αποτέλεσμα, απαιτείται η ύπαρξη λογισμικού παρεμβολής των αεροδυναμικών φορτίων από το πυκνό αεροδυναμικό πλέγμα στο αραιό πλέγμα του στερεού καθώς για και την παρεμβολή των υπολογιζόμενων παραμορφώσεων από το αραιό στο πυκνό πλέγμα στην επιφάνεια διεπαφής. Το λογισμικό που προγραμματίστηκε για το σκοπό αυτό βασίζεται στις συναρτήσεις μορφής των τριγωνικών και τετραπλευρικών στοιχείων για την παρεμβολή. Πέραν της παραμόρφωσης των αντίστοιχων κόμβων του πυκνού αεροδυναμικού πλέγματος στην επιφάνεια διεπαφής, απαιτείται, επιπλέον, η παραμόρφωση και του ογκικού αεροδυναμικού πλέγματος. Για την παραμόρφωση του τελευταίου χρησιμοποιείται λογισμικό βασιζόμενο στη θεωρία των συναρτήσεων ακτινικής βάσης (**R**adial **B**asis **F**unction), το οποίο έχει αναπτυχθεί στη ΜΠΥΡΒ/ΕΜΠ στο πλαίσιο διδακτορικής διατριβής, [4]

Ροή Επίλυσης Αεροελαστικού Προβλήματος

Μετά την επιλογή των επιμέρους εργαλείων και τη μεταξύ τους αμφίδρομη σύζευξη, η επίλυση του αεροελαστικού προβλήματος μπορεί να πραγματοποιηθεί με τον αλγόριθμο του σχήματος 2. Ως αφετηρία θεωρείται το απαραμόρφωτο σχήμα της πτέρυγας, ενώ στον λεγόμενο ΄μηδενικό΄ αεροελαστικό κύκλο υλοποιείται η διαδικασία φουσκώματος.

Εφαρμογές

Με την ολοκλήρωση του προγραμματισμού διαφόρων εργαλείων καθώς και τη σύζευξη των επιλυτών, μελετήθηκαν οι περιπτώσεις πτερύγων του πίνακα 1. Οι συνθήκες ροής που χρησιμοποιήθηκαν για όλες τις περιπτώσεις παρουσιάζονται στον πίνακα 2. Δύο είναι τα κύρια υλικά που χρησιμοποιήθηκαν σε όλες τις περιπτώσεις και τα χαρακτηριστικά τους παρουσιάζονται στους πίνακες 3 και 4. Το πρώτο σύνθετο υλικό μοντελοποιείται ως ορθοτροπικό υλικό ενώ το δεύτερο ως ισοτροπικό. Το δεύτερο

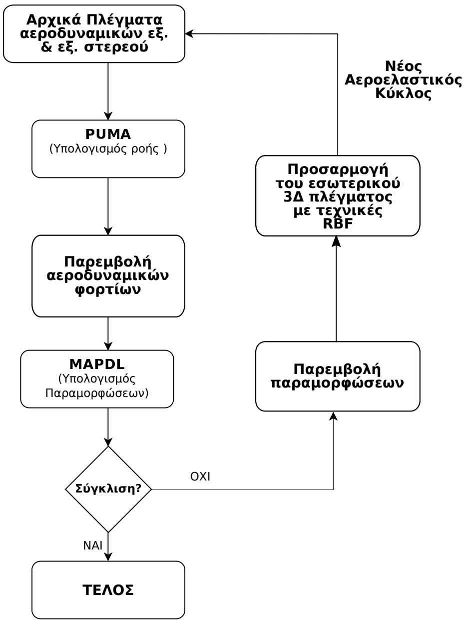

Σχήμα 2: *Διάγραμμα ροής επίλυσης αεροελαστικού προβλήματος.*

Εξισώσεις Ροής	*Χρησιμοποιούμενο Υλικό*
Περίπτωση 1: NACA4318 πτέρυγα χωρίς σχοινιά πρόσδεσης	
Euler	Σύνθετο/Δύσκαμπτο
RANS	Σύνθετο/Δύσκαμπτο
RANS	Ελαστικό
Περίπτωση 2: NACA4318, 'μορφής κάμπιας', χωρίς σχοινιά πρόσδεσης	
RANS	Σύνθετο/Δύσκαμπτο
RANS	Ελαστικό
Περίπτωση 3: NACA4318 πτέρυγα με σχοινιά πρόσδεσης	
RANS	Σύνθετο/Δύσκαμπτο
Περίπτωση 4: NACA0012 πτέρυγα χωρίς σχοινιά πρόσδεσης	
Euler	Σύνθετο/Δύσκαμπτο
RANS	Σύνθετο/Δύσκαμπτο
RANS	Ελαστικό
Περίπτωση 5: NACA0012 πτέρυγα με σχοινιά πρόσδεσης	
RANS	Σύνθετο/Δύσκαμπτο

Πίνακας 1: *Σύνοψη των περιπτώσεων που μελετήθηκαν.*

υλικό σε σύγκριση με το σύνθετο υλικό, είναι αρκετά πιο ελαστικό.
Ενδεικτικά παρουσιάζονται μερικά από τα αποτελέσματα των περιπτώσεων που με-

Κατάσταση στα Όρια	**Τιμή**
Πυκνότητα Αέρα	1.2 kg/m^3
Στατική Πίεση	101325 Pa
Μέτρο Ταχύτητας	60 m/s
Κατεύθυνση Ροής	Άξονας x
Γωνία Pitch	10 °
Γωνία Yaw	0 °
Θερμοκρασία	294 K
Δυναμική Συνεκτικότητα Αέρα	$1.716 \times 10^{-5} kg/ms$
Μοντέλο Τύρβης	Spalart-Allmaras

Πίνακας 2: *Συνθήκες ροής για όλες τις περιπτώσεις.*

Ιδιότητες Ορθοτροπικού Σύνθετου Υλικού	
Πυκνότητα	$1000.7 kg/m^3$
Μέτρο Ελαστικότητας XY	$9.3769 \times 10^9 kg/ms^2$
Μέτρο Ελαστικότητας YZ	$8.411 \times 10^9 kg/ms^2$
Μέτρο Ελαστικότητας XZ	$8.411 \times 10^9 kg/ms^2$
Λόγος Poisson	0.36
Μέτρο Διάτμησης XY	$1.972 \times 10^8 Pa$
Μέτρο Διάτμησης YZ	$1.489 \times 10^8 Pa$
Μέτρο Διάτμησης XZ	$1.489 \times 10^8 Pa$

Πίνακας 3: *Ιδιότητες σύνθετου υλικού.*

Ιδιότητες Ισοτροπικού Ελαστικού Υλικού	
Πυκνότητα	$1400.6 kg/m^3$
Μέτρο Ελαστικότητας	$2 \times 10^8 kg/ms^2$
Λόγος Poisson	0.33

Πίνακας 4: *Ιδιότητες ελαστικού υλικού*

λετήθηκαν. Όλα τα αποτελέσματα βρίσκονται στο κυρίως κείμενο της διπλωματικής εργασίας, στην Αγγλική γλώσσα.

Περίπτωση 1: Στα σχήματα 3, 4 παρουσιάζεται η πρώτη περίπτωση. Η γεωμετρία της πτέρυγας ακολουθεί το περίγραμμα της αεροτομής NACA4318, και η ροή επιλύεται σε μη-δομημένο πλέγμα. Στο σχήμα, 4, είναι εμφανής η παραμόρφωση του σχήματος της πτέρυγας λόγω των αεροδυναμικών φορτίων καθώς και η αλλαγή στις ισογραμμές της πίεσης.

Περίπτωση 2: Στη δεύτερη περίπτωση, η γεωμετρία της πτέρυγας δημιουργείται από κυλινδρόμορφους θαλάμους που ακολουθούν το περίγραμμα της αεροτομής NACA4318, 5. Στο σχήμα, 6, το οποίο αντιστοιχεί στο ελαστικό υλικό για την πτέρυγα, παρουσιάζεται η μεγάλη μετακίνηση της πτέρυγας προς τα πάνω και πίσω λόγω των αεροδυναμικών φορτίων.

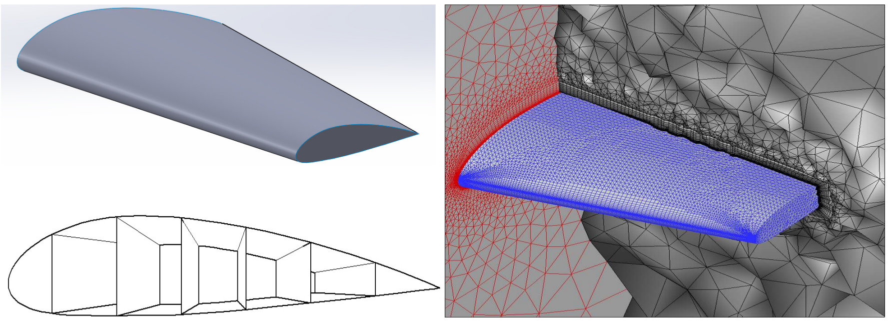

Σχήμα 3: *Περίπτωση 1. Αριστερά-Πάνω: Προοπτική όψη της πτέρυγας. Αριστερά-Κάτω: Εσωτερικές διαμορφώσεις της φουσκωτής πτέρυγας. Δεξιά: Αεροδυναμικό πλέγμα.*

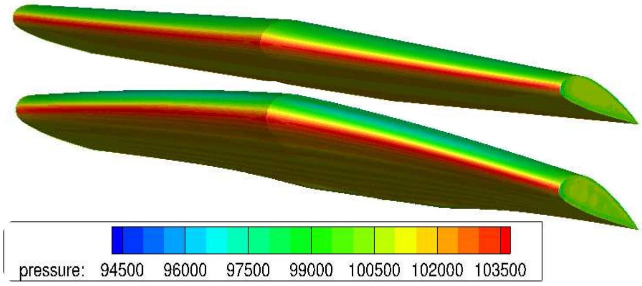

Σχήμα 4: *Περίπτωση 1. Ισογραμμές πίεσης στην απαραμόρφωτη (πάνω) και στην παραμορφωμένη πτέρυγα (κάτω), στο τέλος του δέκατου αεροελαστικού κύκλου.*

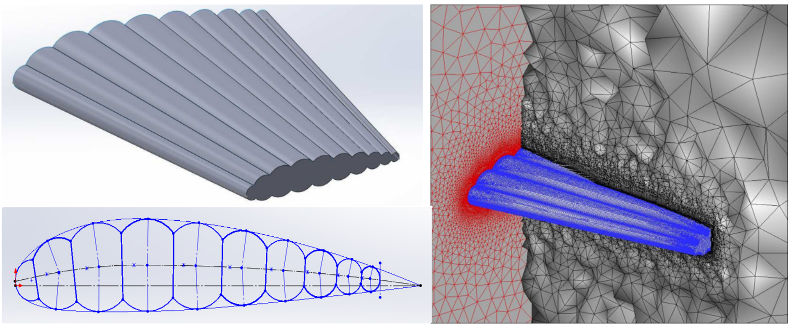

Σχήμα 5: *Περίπτωση 2. Αριστερά-Πάνω: Προοπτική όψη της αεροτομής. Αριστερά-Κάτω: Προσέγγιση του σχήματος της αεροτομής NACA4318 με μια σύνθεση κυλινδρόμορφων διαδοχικών θαλάμων, 'μορφή κάμπιας'. Δεξιά: Αεροδυναμικό πλέγμα.*

Περίπτωση 3: Η περίπτωση 3 περιλαμβάνει στην επίλυση των εξισώσεων δομικής ανάλυσης την ύπαρξη στηρίξεων (σχοινιά πρόσδεσης) προκειμένου να μελετηθεί η συμπεριφορά της πτέρυγας με το πραγματικό είδος στηρίξεων. Η ύπαρξη σχοινιών επιτρέπει στην πτέρυγα μεγαλύτερη μετακίνηση σε σύγκριση με την περίπτωση 1 στην οποία οι στηρίξεις τοποθετούνται απευθείας πάνω στα άκρα της πτέρυγας.

Περίπτωση 4: Η περίπτωση 4 αποτελεί αναθεώρηση της περίπτωσης 1, με μόνη αλλαγή στο σχήμα της πτέρυγας καθώς αυτή ακολουθεί το περίγραμμα της αεροτομής

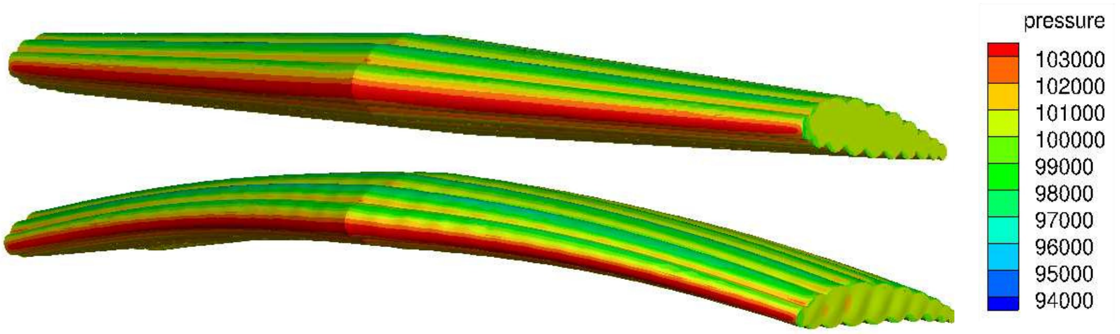

Σχήμα 6: *Περίπτωση 2. Ισογραμμές πίεσης στην απαραμόρφωτη (πάνω) και στην παραμορφωμένη πτέρυγα (κάτω), στο τέλος του έβδομου αεροελαστικού κύκλου.*

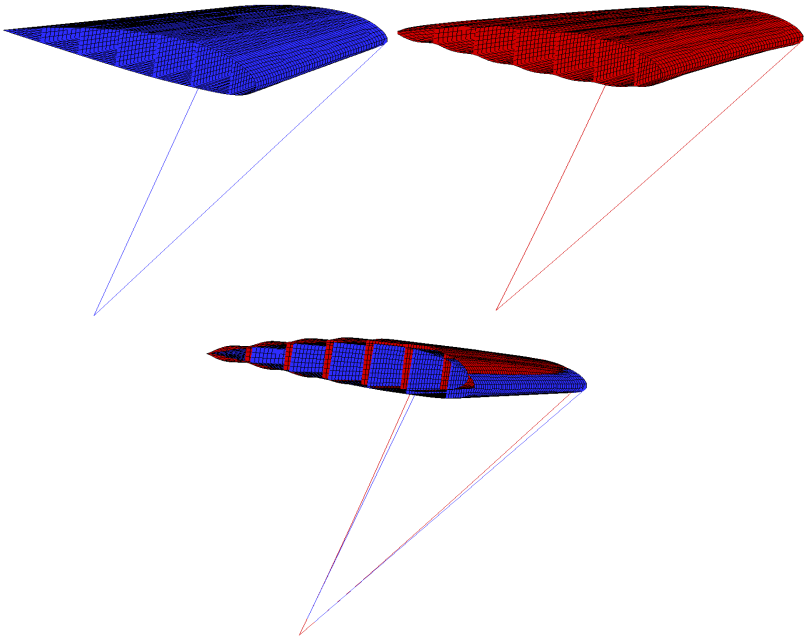

Σχήμα 7: *Περίπτωση 3. Πάνω-Αριστερά: Η αρχική γεωμετρία της πτέρυγας με τα σχοινιά πρόσδεσης. Πάνω-Δεξιά: Η παραμορφωμένη γεωμετρία στο τέλος του δέκατου αεροελαστικού κύκλου. Κάτω: Διαφορά ανάμεσα στην αρχική (μπλε) και στην παραμορφωμένη κατάσταση (κόκκινο).*

NACA0012, 8.

Περίπτωση 5: Τέλος, η περίπτωση 5 αποτελεί μια αναθεώρηση της περίπτωσης 3, με τη γεωμετρία της να ακολουθεί το περίγραμμα της αεροτομής NACA0012. Στο σχήμα 10 παρουσιάζεται η μετακίνηση της αεροτομής όταν συμπεριλαμβάνονται και τα σχοινιά πρόσδεσης.

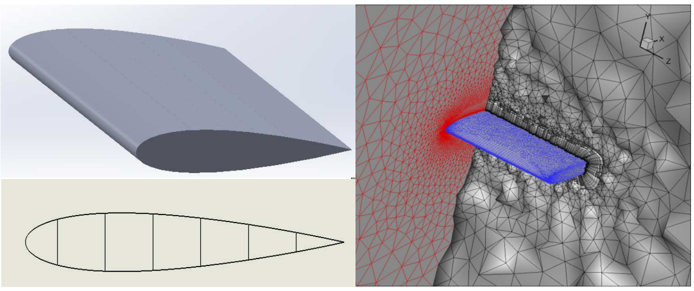

Σχήμα 8: *Περίπτωση 4. Αριστερά-Πάνω: Προοπτική όψη της πτέρυγας. Αριστερά-Κάτω: Εσωτερικές διαμορφώσεις της πτέρυγας. Δεξιά: Αεροδυναμικό πλέγμα.*

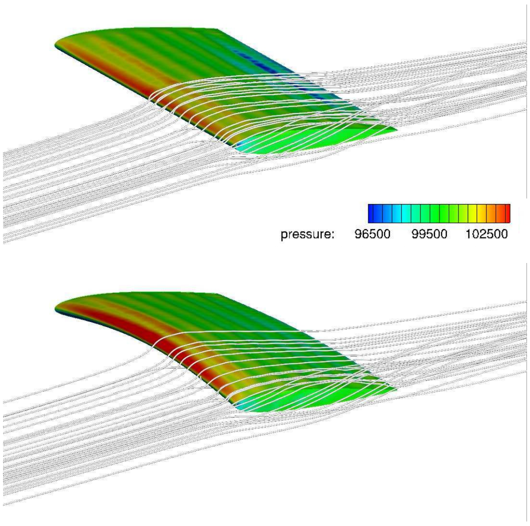

Σχήμα 9: *Περίπτωση 4. Ισογραμμές πίεσης στην απαραμόρφωτη (πάνω) και στην παραμορφωμένη πτέρυγα (κάτω), στο τέλος του έβδομου αεροελαστικού κύκλου.*

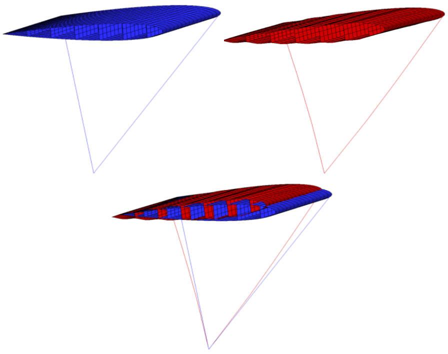

Σχήμα 10: *Περίπτωση 5. Πάνω-Αριστερά: Η αρχική γεωμετρία της πτέρυγας με τα σχοινιά πρόσδεσης. Πάνω-Δεξιά: Η παραμορφωμένη γεωμετρία στο τέλος του δέκατου αεροελαστικού κύκλου. Κάτω: Διαφορά ανάμεσα στην αρχική (μπλε) και στην παραμορφωμένη (κόκκινο) κατάσταση.*

Αποτελέσματα πρόλεξης με μοντέλο συνεκτικής ροής				
Περίπτωση	**Υλικό**	**Οπισθέλκουσα (N)**	**Άνωση (N)**	**Μέγιστη Παραμόρφωση(m)**
Περίπτωση 1 (NACA4318)	Απαραμόρφωτο	186.14	1405.33	-
Περίπτωση 1 (NACA4318)	Σύνθετο /Δύσκαμπτο	189.48	1257.23	0.045
Περίπτωση 1 (NACA4318)	Ελαστικό	209.18	1436.09	0.125
Περίπτωση 2 (Αεροτομή ‘μορφής κάμπιας’)	Σύνθετο /Δύσκαμπτο	258.00	889.26	0.025
Περίπτωση 2 (Αεροτομή ‘μορφής κάμπιας’)	Ελαστικό	289.92	1159.13	0.142
Περίπτωση 3 (NACA4318 -Σχοινιά για στήριξη)	Σύνθετο /Δύσκαμπτο	192.36	1226.02	0.134

Πίνακας 5: *Σύγκριση ανάμεσα σε οπισθέλκουσα, άνωση και μέγιστη παραμόρφωση για τις περιπτώσεις που χρησιμοποιείται η πτέρυγα με το σχήμα της NACA4318 αεροτομής.*

Σύνοψη-Σχόλια

Σε αυτήν τη διπλωματική εργασία μελετήθηκε η αεροελαστική συμπεριφορά φουσκωτών πτερύγων. Στον πίνακα 5 φαίνονται τα αποτελέσματα των περιπτώσεων όπου χρησιμοποιήθηκε το προφίλ της αεροτομής NACA4318. Η παραμόρφωση της πτέρυγας από σύνθετο υλικό στο τέλος των αεροελαστικών κύκλων, είναι σχετικά μικρή με αποτέλεσμα να μην επηρεάζει ιδιαίτερα την οπισθέλκουσα. Ωστόσο, η ελαφρώς ανώμαλη επιφάνεια που δημιουργείται, κυρίως λόγω της εσωτερικής πίεσης, επηρεάζει αρνητικά την παραγόμενη άνωση. Παρόμοια αποτελέσματα, σε μεγαλύτερο βαθμό ωστόσο, παρατηρούνται στην περίπτωση της πτέρυγας με ‘σχήμα κάμπιας’, η οπισθέλκουσα της οποίας είναι αρκετά μεγαλύτερη ενώ η παραγόμενη άνωση είναι αισθητά μειωμένη. Η παρουσία των σχοινιών πρόσδεσης δεν επηρεάζει ιδιαίτερα την αεροδυναμική απόδοση της πτέρυγας παρόλο που επιτρέπει μεγαλύτερες μετακινήσεις συγκριτικά με την απευθείας στήριξη της πτέρυγας. Τέλος, συγκρίνοντας τα δύο υλικά, παρατηρείται ότι οι μεγάλες παραμορφώσεις αυξάνουν ταυτόχρονα την οπισθέλκουσα και την άνωση της πτέρυγας. Στα επόμενα βήματα το εωδιαφέρον εστιάζει στη βελτιστοποίηση των φουσκωτών πτερύγων, χρησιμοποιώντας είτε εξελικτικούς αλγόριθμους είτε συζυγείς μεθόδους. Σχετική έρευνα είναι σε εξέλιξη στη ΜΠΥΡ/ΕΜΠ.

Επιλεγμένη Βιβλιογραφία

[1] A. Cherubini, A. Papini, R. Vertechy and M. Fontana. Airborne Wind Energy Systems: A review of the technologies. *Renewable and Sustainable Energy Reviews*, 51:1461–1476, 2015.

[2] ANSYS, Inc. *ANSYS 12–Theory Reference Manual*, 2009.

[3] V. Asouti, X. Trompoukis, I. Kampolis, and K. Giannakoglou. Unsteady CFD computations using vertex–centered finite volumes for unstructured grids on Graphics Processing Units. *International Journal for Numerical Methods in Fluids*, 67(2):232–246, May 2011.

[4] F. Gagliardi. *Shape parameterization and constrained aerodynamic optimization. Applications including turbomachines.* PhD thesis, Parallel CFD & Optimization Unit NTUA, Athens, In progress.

[5] M. Lindell, S. Hughes, M. Dixon and C. Willey. Structural Analysis and Testing of the Inflatable Re-entry Vehicle Experiment (IRVE). May 1-4 2006.

[6] P. Spalart and S. Allmaras. A one-equation turbulence model for aerodynamic flows. AIAA Paper 1992-439, 30th Aerospace Sciences Meeting and Exhibit, Reno, Nevada, USA, January 6–9 1992.

[7] X. Trompoukis, V. Asouti, I. Kampolis, and K. Giannakoglou. CUDA implementation of vertex–centered, finite volume CFD methods on unstructured grids with flow control applications. In *GPU Computing Gems*, chapter 17, pages 207–224. Addison-Wesley Professional, 2011.